HIGH TEMPERATURE SCANDIUM CONTAINING ALUMINUM ALLOYS SUBJECTED TO EQUAL CHANNEL ANGULAR PRESSING

A Dissertation

by

JAHANZAIB MALIK

Submitted to the Office of Graduate and Professional Studies of
Texas A&M University
in partial fulfillment of the requirements for the degree of

DOCTOR OF PHILOSOPHY

Chair of Committee,	Bilal Mansoor
Co-Chair of Committee,	Ibrahim Karaman
Committee Members,	Homero Castaneda
	Karl Ted Hartwig
Head of Department,	Ibrahim Karaman

May 2019

Major Subject: Materials Science and Engineering

ABSTRACT

Precipitation hardenable aluminum alloys are well-known for their high strength-to-weight ratio, good thermal stability, electrical conductivity, and low cost. Al-Sc alloys micro-alloyed with rare earth and transition metal elements can be strengthened for ambient and high temperature applications. This is primarily due to the precipitation of coherent, hard, finely distributed, and coarsening resistant, nanosized $Al_3(X)$ trialuminide precipitates. In addition to precipitation strengthening, equal channel angular pressing (ECAP) can be applied to further enhance mechanical properties of this system by microstructure modification.

In this work, the effect of ECAP on microstructure modification, precipitate evolution, and mechanical response of a high temperature aluminum alloy with micro-additions of Er, Sc, Zr, V, Si was investigated. Combined strengthening with yield strength up to ~180 MPa was achieved after aging to peak hardness followed by grain refinement through ambient temperature ECAP using route 4Bc. Subsequently, a different processing approach of ECAP after homogenization was also carried out. Tensile results showed only a slight improvement of about 2-5% in yield strengths of peak-aged followed by ECAP (PA-ECAP) alloy as compared to homogenized followed by ECAP (H-ECAP) alloy. Mechanical tests combined with calorimetry studies and scanning/transmission electron microscopy confirmed the occurrence of dynamic precipitation during ambient temperature ECAP of Al-Er-Sc-Zr-V-Si in homogenized condition. Hence, it was

established that ECAP can significantly influence the kinetics and distribution of precipitates in these alloys.

Furthermore, pre- and post- ECAPed alloys were subjected to annealing heat treatments. The variations in microhardness after annealing heat treatments at different temperatures highlighted the important role nanoprecipitates play in maintaining microstructure stability of Al-Er-Sc-Zr-V-Si before and after ECAP. Microstructure evolution during static annealing (without the application of load) and dynamic annealing (with applied load) was also studied using interrupted high temperature tensile tests followed by electron backscatter diffraction (EBSD) analysis. Results showed that there is a difference in deformation mechanism for H-ECAP and PA-ECAP. Among the two processing routes, although the magnitude of static and dynamic grain growth in H-ECAP condition was found to be higher than PA-ECAP condition, it showed superior elevated temperature strength and ductility.

Lastly, electrochemical characteristics of Al-Er-Sc-Zr-Si with micro-additions of Group 5 transition elements (V, Nb, or Ta) added individually and then exposed to saline media. There is slight increase in activity of Al-Er-Sc-Zr-Si after addition of any of Group 5 elements (V, Nb, or Ta) which justifies their addition to improve ambient and elevated temperature mechanical properties. The order of mechanical strength is Al-Er-Sc-Zr-Si-V > Al-Er-Sc-Zr-Si-Nb > Al-Er-Sc-Zr-Si-Ta > Al-Er-Sc-Zr-Si.

DEDICATION

To my loving parents, wife and sisters for their prayers, wishes and unconditional and continuous support at every step of my life.

ACKNOWLEDGEMENTS

I would like to take this opportunity to express immense thanks and gratitude to my advisors, Dr. Bilal Mansoor and Dr. Ibrahim Karaman for their endless guidance, support, and encouragement during the entire duration of my Ph.D.

Dr. Bilal Mansoor has always empowered me to do excellent research and encouraged me to think out-of-the-box and come up with unique ideas to explore various dimension of my research. He been a very active and supportive advisor. He has provided guidance at both professional and personal levels. He held regular meetings, which helped me to work continuously and more productively on my research. Regular input from Dr. Bilal has tailored my research towards higher impact.

I'm especially thankful to Dr. Ibrahim Karaman for giving me the opportunity to work on this project. Despite always being busy, he regularly held project meetings to review progress and set future direction. I have managed to learn so much from his advice on how to conduct research and present in a most effective way.

I would also like to thank Dr. Karl T. Hartwig and Dr. Homero Casteneda for serving as my committee members and following up on my research progress. I would like to thank my colleagues Dr. Muhammad Usman and Wahaz Nasim for their input and important technical assistance in this project.

Most importantly, I would like to express my deepest gratitude to my family for supporting and motivating me at every step. My father's advices and my mother's love and prayers has always kept me on the right path and helped me achieve my goals.

CONTRIBUTORS AND FUNDING SOURCES

Contributors

This work was supervised by a dissertation committee consisting of Assistant Professor Dr. Bilal Mansoor (advisor) of the Department of Mechanical Engineering, Professor Dr. Ibrahim Karaman (co-advisor), Professor Dr. Karl T. Hartwig and Associate Professor Dr. Homero Castaneda of the Department of Materials Science and Engineering.

Funding Sources

This work was made possible by a National Priorities Research Program (NPRP) grant from the Qatar National Research Fund (a member of The Qatar Foundation), under grant number NPRP 7-756-2-284. The statements made herein are solely the responsibility of the authors.

NOMENCLATURE

APT	Atom Probe Tomography
BM	Base metal (Al-Er-Sc-Zr-Si)
DCP-AES	Direct-Current Plasma Atomic-Emission Spectroscopy
DGG	Stress-induced/Dynamic grain growth
DIC	Differential Isothermal Calorimetry
DSC	Differential Scanning Calorimetry
DSA	Dynamic strain aging
EBSD	Electron Backscatter Diffraction
EC	Electrical Conductivity
ECAP	Equal Channel Angular Pressing
ED	Extrusion Direction
EDM	Electro Discharge Machining
EDS	Energy Dispersive Spectroscopy
EDAX	Energy-dispersive X-ray spectroscopy
EIS	Electrochemical impedance spectroscopy
FD	Flow direction
FCC	Face Centered Cubic
GP zones	Guinier Preston zones
GPB zones	Guinier–Preston–Bagaryatsky zones
H	Homogenized

H-ECAP	Homogenized followed by ECAP
HER	Hydrogen Evolution Reaction
HRTEM	High Resolution Transmission Electron Microscopy
IGC	Intergranular corrosion
ND	Normal Direction
OCP	Open circuit potential
OM	Optical Microscopy
OIM	Orientation (Imaging) Microscopy
PA	Peak Aged
PA-ECAP	Peak aged followed by ECAP
PD	Potentiodynamic polarization
RE elements	Rare Earth elements
SGG	Conventional/Static grain growth
SRS	Strain rate sensitivity
SPD	Severe Plastic Deformation
STEM	Scanning Transmission Electron Microscopy
T	Temperature
TEM	Transmission Electron Microscopy
UFG	Ultra-Fine Grains
UTS	Ultimate Tensile Strength
σ_o	Peierls stress
σ_{ss}	Solid solution strengthening

σ_{ppt}	Precipitation strengthening
σ_{gs}	grain size strengthening
σ_{ρ}	dislocation strengthening
ϵ	True strain
$\dot{\epsilon}$	True strain rate
Q	Activation energy
R	grain radius
R_n	Initial grain radius
n	Grain growth exponent
K	Arrhenius type relation
C_{ct}	Double layer capacitance
CPE	Constant phase element
E_{corr}	Corrosion potential
Z_{diff}	Warburg element
Y_o	Admittance
R_p	Polarization resistance
R_{ct}	Charge transfer resistance
R_{oxide}	Oxide layer resistance

TABLE OF CONTENTS

LIST OF FIGURES

Page

LIST OF TABLES

Page

CHAPTER I

INTRODUCTION AND LITERATURE REVIEW

1.1 Aluminum and its alloys

There is an ever-increasing demand for lightweight, high performance, corrosion resistant metallic alloys. In particular, alloys that offer high specific stiffness and high specific strength at ambient temperature and superior creep resistance at elevated temperature are highly sought after by various industries [1][2]. Therefore, an important practical goal is to design optimal processing routes to further improve mechanical properties and enhance performance of lightweight alloys at a suitable cost.

Aluminum alloys readily satisfy the design criteria of lightweight, and high specific strength at room temperature. Strengthening of aluminum alloys at room temperature and elevated temperature is a comprehensive subject in materials science with a strong practical importance. The ultimate aim generally is to have materials with high strength-to-weight ratio, in order to achieve better efficiencies in high end applications. However, aluminum alloys still have limited use when it comes to elevated temperature applications. This is because Al alloys generally don't meet the strength, durability and stability requirements of high temperature applications. Precipitation hardening is one of the most effective strengthening processes which relies on alloying additions and heat-treatments to improve the mechanical response of metallic alloys [3]. Precipitation relies on solutes that have higher solubility at elevated temperatures and decreasing solubility at low temperatures [4]. The kinetics and coherency of precipitates is what dictates the

elevated temperature strengths. In most conventional precipitation hardenable Al alloys, semi-coherent, incoherent metastable precipitates present at high temperature (~300 °C) result in the reduction of creep resistance [5].

1.2 Generations of scandium containing aluminum alloys

Scandium containing aluminum alloys are heat-treatable, precipitation-hardenable alloys [6]. They contain coherent, finely distributed, hard, $L1_2$ ordered, nanosized Al_3Sc tri-aluminide precipitates that contribute to ambient temperature strength by either precipitate shearing or Orowan looping mechanism [6], [7]. In addition, these Al_3Sc precipitates provide potent coarsening resistance and enable the use of Al-Sc alloys at significantly higher temperatures of up to 350°C, as compared to conventional age-hardenable 2xxx and 6xxx series Al alloys [6]–[8]. Mechanical properties of Al-Sc alloys can be improved by ternary additions with transition or rare earth metals that substitute for the rather expensive Sc to produce more coarsening resistant, coherent, $Al_3(Sc_{1-y}X_y)$ precipitates [9]–[11]. The faster diffusing components segregate to the core of the tri-aluminide precipitates. In fact, partial substitution of the rather expensive Sc by elements such as Zr, Er, and Yb leads to the formation of coarsening resistant core-shell morphology precipitates [15–17].

Summary of various generations of Scandium containing Aluminum alloys:

1. Al-Sc binary system (Sc addition below 0.23%)
    a. Forms $L1_2$-ordered Al_3Sc precipitates
    b. Coarsening resistant to ~300°C
    c. Moderate diffusivity of Sc in α-Al

2. Al-Sc-Zr ternary system – Group VIA (Ti, Zr, Hf) slower diffusers than Sc
    a. Forms Al_3(Sc,Zr) precipitates – Sc core, Zr shell
    b. Substitutes Sc – reduces cost
    c. Coarsening resistance to 400°C
3. Al-Sc-Er ternary system – Rare Earth (Er, Yb) faster diffuser than Sc
    a. Forms Al_3(Sc,RE) precipitates – RE core, Sc shell
    b. Substitutes Sc – reduces cost
    c. Increases lattice parameter mismatch
4. Al-Er-Sc-Zr quaternary system – Er faster diffuser than Sc and Zr
    a. Forms core/double-shell precipitates
    b. Coarsening resistant to 400°C due to Zr additions
    c. Increased lattice mismatch due to Er additions
5. Proposed High Temperature Al Alloy:

    Al-Er-Sc-Zr-X quinternary system – X is Group VA (V, Nb, or Ta)
    a. (V, Nb, or Ta) slower diffusers than Er, Sc, and Zr
    b. Expected to form high number density Al_3(Er,Sc,Zr,X) precipitates
    c. Core/triple shell “nano-onion” structure
    d. Expected to exhibit extreme coarsening resistance and superior creep properties.

Table 1 display an extensive review of various generations of scandium containing alloys published in the literature. Selection criteria was based on wt. % of Sc and other rare-earths and transition elements that substituted Sc. The review was aimed to justify that Sc

substitution in Al-Sc alloys with Zr, Er, and V can still produce alloys with reasonable strength. Substitution of relatively costly Sc is necessary to make these alloys commercially viable. Figure 1 illustrates all the microhardness values for each generation in ascending order. It can be seen that reducing Sc content down to 0.014 at. % substituting with Er and Zr can also give microhardness around 60 HV (G5). In our recent work with Erdeniz et al., we reported on the development of a vanadium micro-alloyed Al-Er-Sc-Zr-Si alloy [16]. This system, after a double-aging heat treatment, exhibited a peak microhardness of 600 MPa at ambient temperature. This strength level was linked to a fine dispersion of nanosized, core-shell morphology, vanadium containing Al_3(Sc, Er, Zr, V) precipitates. In addition, the alloy showed significant creep resistance up to 400°C, which was linked to potent grain coarsening resistance, provided by these unique, core-shell morphology, tri-aluminide precipitates.

Table 1 Review of various generations of Al-Sc alloys published in recent years. Microhardness values variation with additions of Sc, rare-earths and transition elements. (at. % unless otherwise specified).

Alloy Composition	Hardness (HV)	Heat-treatment	Reference
Al-1100	24	As-cast	---
Al-0.6wt%Sc	46	Homogen-ized	K. Venkateswarlu (2004) [17]
Al-1.0wt%Sc	52		
Al-2.0wt.%Sc	64		
Al-0.05wt.%Sc	35	300 / 24 h	A. k. Lohar (2009) [18]
Al-0.1wt.%Sc	59		
Al-0.5wt.%Sc	69		

Table 1 continued

Alloy Composition	Hardness (HV)	Heat-treatment	Reference
Al-0.2wt.%Sc	45	400 / 3 h	Davydov (1996) [19]
Al-0.2wt.%Sc-0.15wt.%Zr	65	400 / 24 h	
Al-0.4wt.%Sc	76	450 / 0.15 h	
Al-0.4wt.%Sc-0.15wt.%Zr	74		
Al-0.1Zr	40.8	450 / 3 h	Knipling (2010) [20]
Al-0.1Sc-0.1Zr	75.5	400 / 3 h	
Al-0.1Sc	66.3	300 / 3 h	
Al-0.06Sc	44	325 / 3 h	Knipling (2011) [21]
Al-0.06Zr	30.5	500 / 3 h	
Al-0.06Sc-0.06Zr	64.2	425 / 3 h	
Al-0.06Sc	34.9	300 / 24 h	Karnesky (2006) [10]
Al-0.08Sc	64.2	300 / 16 h	
Al-0.64Sc-0.022Er	66.3	300 / 16 h	
Al-0.05wt.%Sc-0.15wt.%Zr	35.0	300 / 24 h	A. K. Lohar (2009) [18]
Al-0.1wt.%Sc-0.15wt%Zr	62.0		
Al-0.5%Sc-0.15wt%Zr	71.0		
Al–0.05Sc–0.01Er–0.06Zr	46.6	400 / 140 h	Vo. (2014) [22]
Al–0.055Sc–0.005Er–0.02Zr–0.05Si	53.0	400 / 60 h	
Al-0.005Er-0.02Sc-0.07Zr-0.08V-0.06Si	58.0	350 / 16h + 400 / 20 h	Erdeniz (2017) [16]
Al–0.005Er–0.02Sc–0.07Zr-0.06Si	55.0	350 / 16h + 400 / 12 h	

Table 1 continued

Alloy Composition	Hardness (HV)	Heat-treatment	Reference
Al-0.08Zr	25.3	350 / 400 h	S.P Wen (2011) [23]
Al-0.04Er-0.02Zr	37.0	350 / 2 h	
Al-0.04Er-0.04Zr	39.6	350 / 300 h	
Al-0.04Er-0.08Zr	57.3	350 / 200 h	
Al-0.04Er	40.8	350 / 0.2 h	
Al-0.18Sc	73.9	375 / 0.5 h	Fuller (2003) [9]
Al-0.14Sc-0.012Zr	68.3	375 / 0.8 h	
Al-0.055Sc-0.005Er-0.02Zr-0.05Si	54.2	425 / 1 h	Luca (2016) [15]
Al-0.014Sc-0.008Er-0.08Zr-0.1Si	57.9	400 / 3 h	
Al-0.06Sc-0.05Er-0.01Zr-0.04Si	61.8	300 / 4 h + 425 / 8 h	Booth-Morrison (2012) [14]
Al-0.06Sc-0.06Zr	56.1	300 / 24 h + 400 / 24 h	Booth-Morrison (2011) [24]
Al-0.05Sc-0.06Zr-0.01Er	50.5		
Al-0.04Sc-0.06Zr-0.02Er	49.5		
Al-0.12Sc	71.3	325 / 2 h	Karnesky (2006) [10]
Al-0.9Sc-0.03Er	65.6	325 / 2 h	

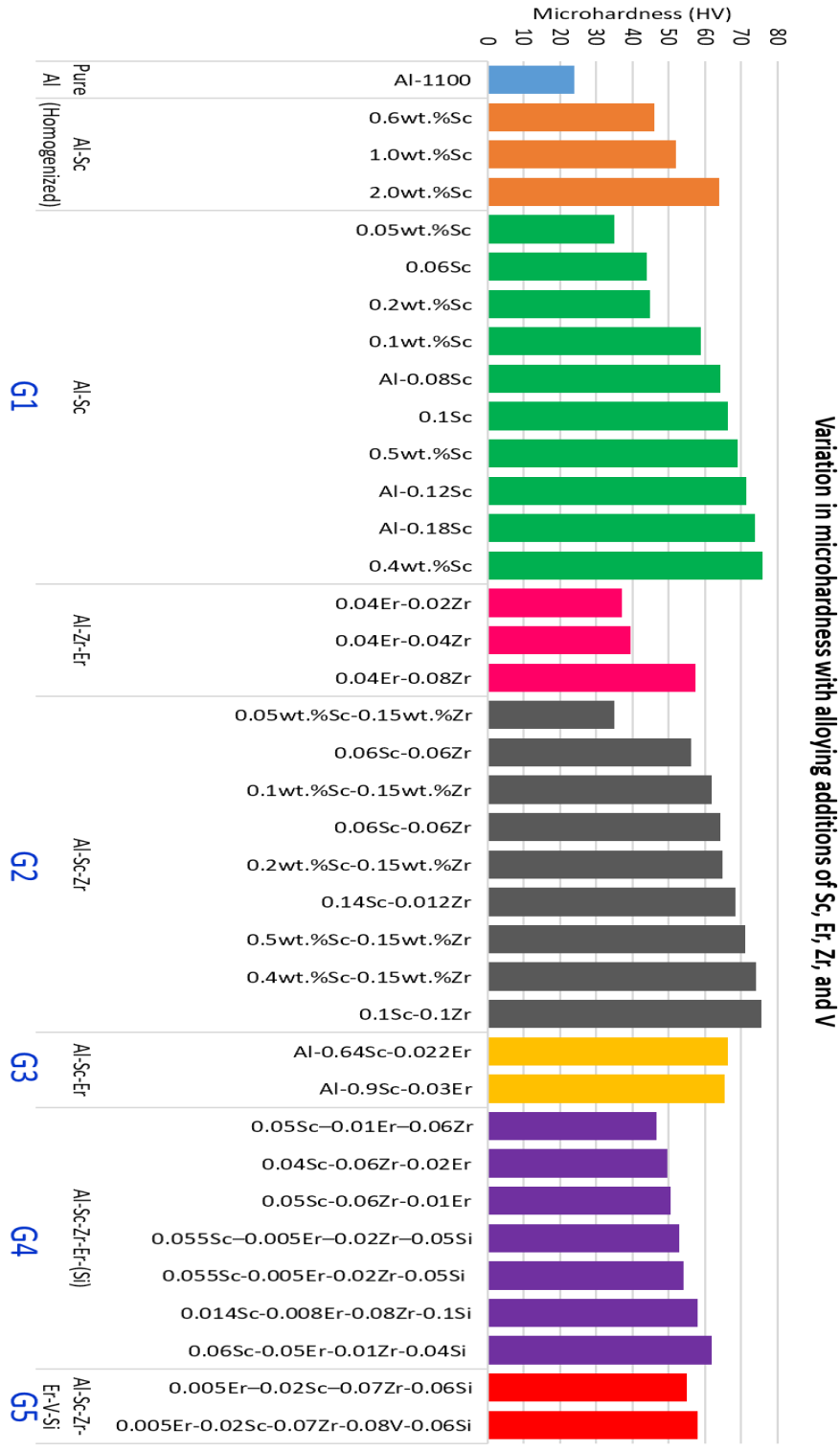

Figure 1 Bar chart of various Al-Sc generation (G1 to G5) from the table shown earlier.

1.3 Equal channel angular pressing

In addition to precipitation strengthening, severe plastic deformation (SPD) can be employed to further enhance strength through grain refinement in accordance with the Hall-Petch relationship [25]–[29]. Equal channel angular pressing (ECAP) is a well-known severe plastic deformation technique that routinely produce ultra-fine grained (UFG) materials from bulk [30]–[32]. ECAP offers the ability to refine microstructure and manipulate texture in a range of different alloys [33]–[35]. ECAP is a popular SPD technique largely due to its strengthening effectiveness and processing efficiency [30], [36]–[38]. UFG structures produced by ECAP, exhibit improved strengths and fatigue life at ambient temperature, and can even show superplastic behavior at elevated temperatures [39]–[41]. The intense plastic strain imparted during ECAP ensures that the processed materials are fully dense and virtually free from macro-segregation typically observed in cast materials. ECAP of precipitation hardenable lightweight alloys is more attractive because it further enhances the potential of such alloys for high performance industrial applications. A growing body of literature has shown, precipitation kinetics, size, morphology and distribution of precipitates and second phase particles in the matrix of processed material, critically depend on the ECAP temperature and route. The influence of thermodynamic state of the material prior to ECAP i.e. super-saturated, peak-aged or overaged condition; in such scheme of things has also received some attention. In this context, pre-ECAP aging and post-ECAP aging are the two main processing sequences that are used to optimize the strengthening of precipitation hardenable alloys. In the post-ECAP aging category, many authors have investigated the effect of ECAP on precipitation

kinetics and the link between high density of lattice defects and diffusion controlled processes [42]–[44]. In the pre-ECAP aging, major areas of concern are the influences of deformation during ECAP on the precipitates distribution [45], fracturing [46], coarsening/dissolution [47], and subsequent microstructure stability at elevated temperatures. To the best of our knowledge, the impact of severe plastic deformation on core/shell morphology precipitates has not been investigated before in any system.

The literature on severe plastic deformation of heat-treatable aluminum alloys indicates post ECAP aging at a temperature much lower than the usual aging temperature, can yield superior strength by taking combined benefit of both grain-size effect and precipitates [48]. Sordi et al. studied the precipitation kinetics in an Al-Ag alloy [46]. They reported that diffusion kinetics accelerated rapidly after ECAP due to the presence of defect structure, comprising mainly of grain boundaries, sub-grains, and dislocations. Kim et al. compared pre-ECAP and post-ECAP aging of 6061 Al alloy [49]. They found post-ECAP aging to be more effective compared to aging of unpressed material. However, they used a low aging temperature to suppress the softening during heat treatment. Contrary to the favorable aspects of post-ECAP aging, Fare et al. reported small but continual decrease in hardness after aging of ECAPed Al-Mg-Si alloy at 180°C [44].

1.4 Research motivation and objectives

1.4.1 Motivation

a) The literature indicates significantly long aging times at high temperatures for Al-Er-Sc-Zr-X-Si. Erdeniz et al. [16] reported double aging at 350°C / 16 h followed by 400°C / 12 h to achieve peak microhardness in Al-Er-Sc-Zr-V-Si.

The goal here is to devise a processing route that would suppress or bypass longer aging times at high temperatures.

b) Improve limited ductility at temperatures around 400 °C. Analyze superplastic ability of Al-Sc alloys.

c) Understand role of precipitates and deformation mechanisms during thermomechanical characterization.

1.4.2 Significance to Al-Sc alloys

- Combined strengthening (precipitation hardening and grain refinement) of Al-Er-Sc-Zr-V-Si will result in the improvement of mechanical properties at room temperature, as expected. However, the impact of combined strengthening on high temperature tensile properties shall be investigated at temperature up to 400 °C
- Post- and Pre- ECAP aging and its effect on precipitation kinetics and maintaining thermal stability of Al-Er-Sc-Zr-V-Si will be studied to identify the most efficient processing route that would give optimum properties at room temperature as well as elevated temperature.
- It is not yet known that how ECAP influence the morphology of core/shell precipitates. It will be interesting to observe whether the core/shell structure of trialuminide precipitates is conserved after ECAP?
- High temperature tensile comparison of Nb and Ta containing Al alloys will be evaluated to show which alloying addition contributes to high creep resistance.

1.4.3 Objectives

The goal of this thesis is to improve the mechanical strength and thermal stability through heat treatments, microstructure modification and precipitation of scandium containing aluminum alloys, subjected to equal channel angular pressing. The desired goal will be accomplished using the following objectives:

1. Mechanical characterization of commercially pure aluminum (Al-1100) subjected to various ECAP routes
    - ECAP routes 1A, 2C, 4C, 4Bc and subsequent grain refinement
    - Effect of temperature on tensile strength and ductility
    - Effect of strain on tensile strength and ductility
    - Evaluate optimum ECAP route for processing of Al-Sc alloy.
2. Grain refinement, thermal stability and role of precipitates after ECAP of an aged Al-Er-Sc-Zr-V-Si alloy
    - Comparative study of thermal stability of homogenized (H), peak-aged (PA), and peak-aged + ECAP (PA-ECAP).
    - Distribution and orientation of grains and precipitates.
    - Microhardness homogeneity after ECAP.
    - Role of precipitates in maintaining thermal stability and inhibiting grain coarsening.
3. Precipitate evolution during and after ECAP of homogenized (supersaturated) Al-Er-Sc-Zr-V-Si alloy
    - Homogenized alloy will be subjected to ECAP route 4Bc

- Dynamic precipitation and post-ECAP aging studied using: DSC, DIC, Isochronal and Isothermal heat treatment.
- Mechanical (Tensile, VHN) and microstructural characterization (SEM, TEM)

4. Effect of ECAP on high temperature tensile behavior of Al-Er-Sc-Zr-V-Si alloy
    - Strain rate sensitivity using decremental strain-rate testing.
    - Evaluation of strain hardening coefficients
    - Influence of ECAP on deformation mechanisms
    - Microstructure evolution and grain growth during static annealing (without any applied load) and dynamic annealing (with applied load).
5. Electrochemical characterization of Al-Er-Sc-Zr-V-Si, Al-Er-Sc-Zr-Nb-Si, Al-Er-Sc-Zr-Ta-Si and base condition Al-Er-Sc-Zr-Si alloys
    - Open circuit potential of the three alloys in their peak-aged conditions.
    - Potentiodynamic polarization and electrochemical impedance spectroscopy for extended period in 1% NaCl solution.
    - Corrosion mechanism and surface degradation after exposure.

CHAPTER II

MECHANICAL PROPERTIES OF COMMERCIALLY PURE ALUMINUM ALLOY SUBJECTED TO VARIOUS ECAP ROUTES

2.1 Introduction

High strength light metals are always in demand and an important requirement for aerospace and automotive industries. Aluminum and its alloys are popularly known as lightweight structural materials with high specific strength, excellent corrosion resistance, good thermal and electrical properties, recyclability and ease in casting. Production and commercial aluminum and its alloys are divided into two categories: cast and wrought products. Wrought alloys are basically cast ingot subjected to plastic deformation processes, such as rolling, extruding, and drawing etc. The designation of these alloys represents composition and temper. 1xxx series of aluminum is > 99.0 % in purity. This alloy is a good representation of a commercially pure Al. One such alloy with a minimum purity of 99.0 % is Al-1100-O which has low mechanical properties but excellent workability. Al-1100 can be strengthened by strain hardening or work hardening processes [50].

Grain size reduction in submicron or even nanometer range can greatly enhance mechanical properties according to Hall-Petch relationship [51]. Traditional methods to reduce grain size by straining and plastic deformation includes cold rolling, extrusion, and drawing. However, in past several decades novel methods have emerged to induce severe plastic deformation (SPD) on a metal/alloy to produce ultra-fine grain structures with

superior mechanical properties. Equal channel angular pressing (ECAP) is one such novel technique that can produce ultra-fine grain structures while conserving the shape of the billet [52]. The principle and mechanical of grain refinement using ECAP has been discussed in detail in Chapter 1, Section 1.3. Final structure of the billet depends on the processing route and number of passes. There are four basic ECAP routes: Route A (no rotation), Route B_A (alternating 90° rotation), Route B_C (counterclockwise 90° rotation), and Route C (counterclockwise 180° rotation). There are different slip systems that are activated during each of these processing routes [53]. Other important parameters during ECAP are the number of passes (from 1 to 12 generally), pressing speed (in mm/min) and pressing temperature. Selection of route and number of passes to achieve optimal strength/ductility combination depends on the alloy system. For instance, ECAP of magnesium alloys is difficult due to the limited number of slip planes in its hexagonal close packed structure and is often subjected to high temperature ECAP for limited number of passes to avoid cracks. Aluminum alloys, due to their FCC crystal structure are relatively easier to ECAP at room temperature. However, selection of ECAP route and number will constitute towards grain size and distribution, grain boundary orientations and resulting strength/ductility combination at ambient and elevated temperatures. Literature shows that a minimum of 2 passes is generally enough to induce considerable grain refinement. However, four or more passes can impart enough strains to produce a UFG structure with high-angle grain boundaries using route B_c [54]. The challenge is to modify the microstructure to achieve a good combination of strength and ductility and optimize the grain size for room temperature as well as high temperature application.

Commercially pure Al-1100 was selected as baseline unalloyed aluminum to evaluate the best combination of ECAP route and number of passes to maintain strength and ductility at ambient and elevated temperature. In this context Saravanan et al. [55] studied number of ECAP passes required to achieve peak-hardness in 99.5 % pure Al using route B_c. They found gradual decrease in grain size with the number of passes, utilizing up to 8 passes. Hardness increased from 20 BHN for as-received condition to ~44 BHN after 4 passes, however, the difference in hardness between 4-8 passes was not significant, which shows that substantial increment in hardness is during the first 4 passes. Iwahashi et al. [56] conducted ECAP on high purity aluminum with initial grain size of ~1.0 mm. They compared number of passes (up to 10) without rotation (route A) and with 180° rotation (route C). Both routes ultimately give a similar equiaxed structure after 10 passes, however route C showed an enhanced microstructural evolution with high angle grain boundaries. Moreover, rotation between passes result in elimination of elongated sub-grains. It was also reported that 4 passes are enough to obtain optimal microstructure modification using route C. Similar trend in number of passes has been shown by Horita et al. [37] during mechanical characterization of ECAPed Al-1100, 0.2 % proof stress peaked after 4 passes and remained indifferent after 6 passes. They also observed improvement in ductility which was attributed to the formation of fine-grain with high-angle grain boundaries.

In this chapter, commercially pure aluminum Al-1100-O is subjected to various ECAP routes and passes to select the best route/pass that will give an optimum microstructure for strength and ductility combination at room as well as elevated

temperature. The results from this chapter will be used to identify a possible route and number of passes for Al-Er-Sc-Zr-V-Si alloy. Selection of Al-1100 for this purpose is justified since the Al-Sc is microalloyed (<~0.1 wt. % alloying additions) and is very similar to pure aluminum when in homogenized condition.

2.2 Experimental Procedure

Commercial pure aluminum Al-1100 with O-temper was purchased in form of 10 in. x 6 in. x 6 in. slabs. Electric discharge machining was employed to cut the billets of size 1x1x6 in. for ECAP. One as-received billet was retained to measure mechanical properties and grain size as a reference.

The ECAP was carried out at room temperature with a pressing speed of 1 mm/min and using a 90° die channel. Three different routes were selected and appropriate number of passes:

1. A (no rotation, 1 pass),
2. Route 2C (counterclockwise 180° rotation after each pass, 2 passes),
3. Route 4C (counterclockwise 180° rotation after each pass, 4 passes) and
4. Route $4B_C$ (counterclockwise 90° rotation after each pass, 4 passes).

Maximum number of 4 passes were decided based on the review of several studies discussed in the introduction section. After ECAP, samples from each billet was sectioned for microstructure characterization and miniature tensile specimens for mechanical testing. In all cases as-received billet (pre-ECAP, designated as 0P) was also analyzed as a reference.

Room temperature tensile tests were carried out on 0P, 1A, 2C, 4C, and 4Bc samples of Al-1100. ECAPed samples were tested in both flow direction (FD) and extrusion direction (ED) to identify which plane/direction gives better combination of strength and ductility for each route with given number of passes. All Tensile tests were conducted at a faster and slower strain rates of $1x10^{-2}$ s^{-1} and $1x10^{-4}$ s^{-1}, respectively, using an electromechanical MTS Insight 30 kN machine. In addition to room temperature tests, high temperature tensile tests at 200 °C were also carried using both strain rates. The temperature of the specimens was maintained within ± 2 °C, measured with a thermocouple placed on the surface of the specimen. Schematic of the miniature tensile specimen used in this study is given in Figure 2. Two specimens were tested at this condition to ensure repeatability.

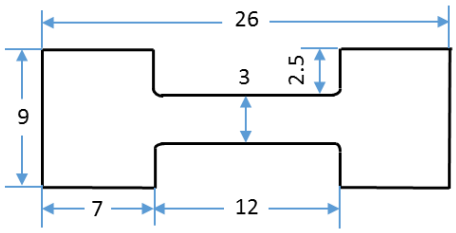

Figure 2 Miniature tensile specimens with 1.5 mm thickness and 11 mm gauge length.

2.3 Results and discussions

Stress-strain engineering curves from tensile tests experiments for as-received 0P (Figure 3) and ECAP pass 1A (Figure 4), ECAP pass 2C (Figure 5), ECAP pass 4C (Figure 6), ECAP pass 4Bc (Figure 7).

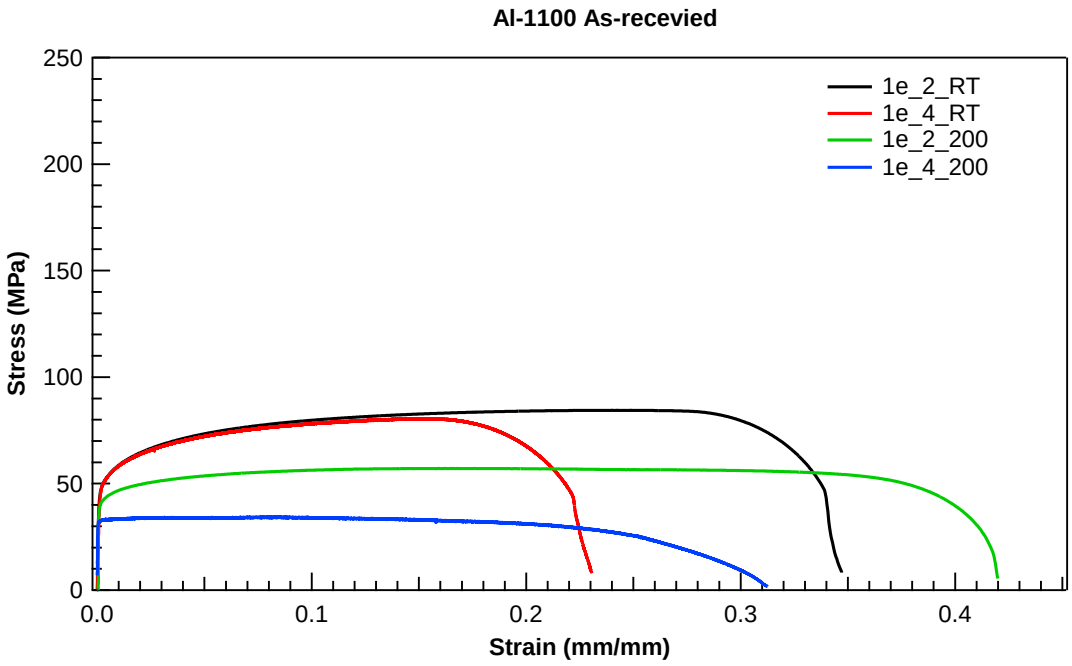

Figure 3 Engineering stress vs. engineering strain plots for Al-1100-O in as-received condition using strain rates of 10^{-2} s^{-1} (black and green) and 10^{-4} s^{-1} (red and blue). Testing at room temperature and 200 °C using both strain rates.

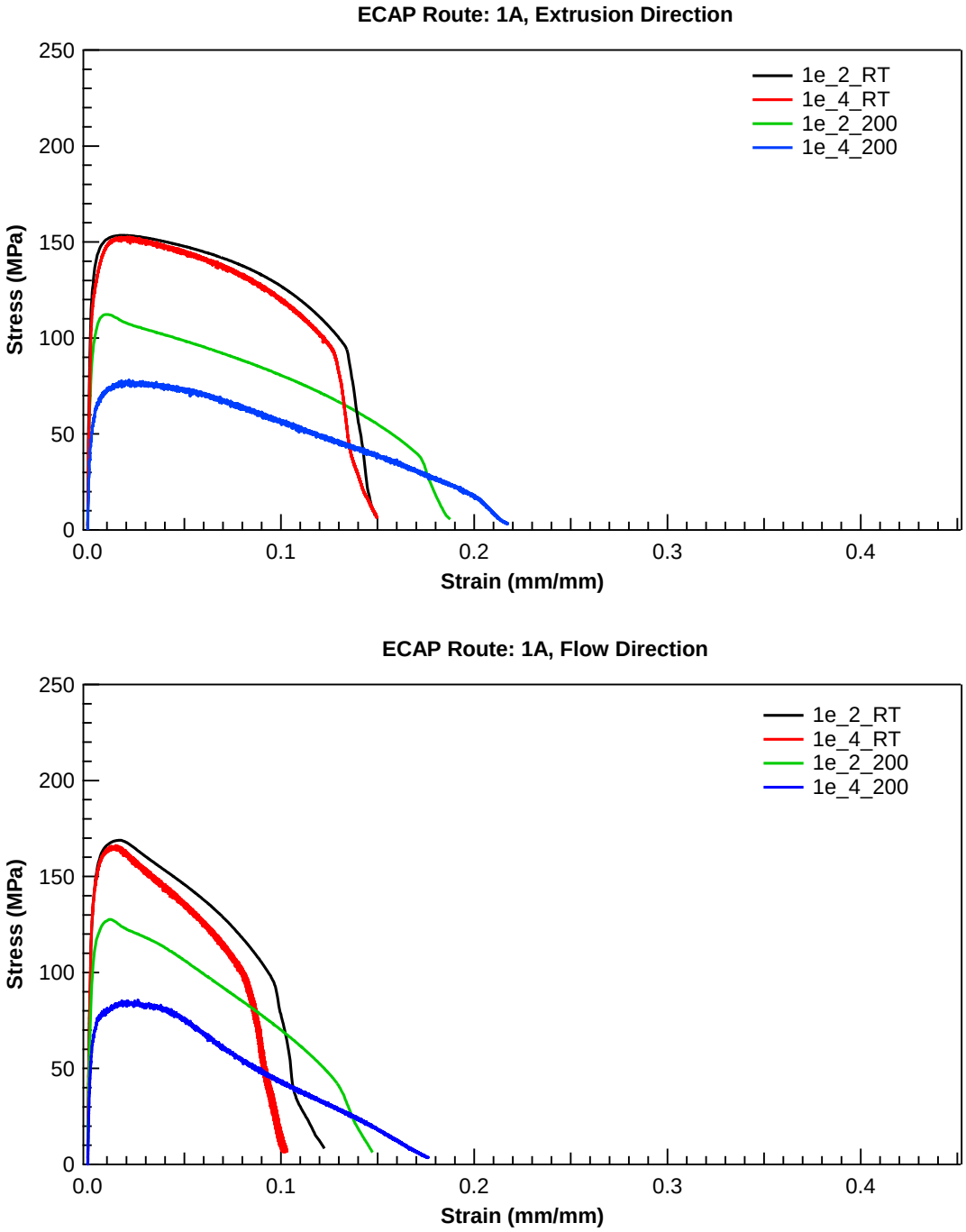

Figure 4 Engineering stress vs. engineering strain plots for Al-1100 ECAPed using route 1A in a) ED and b) FD conditions using strain rates of 10^{-2} s^{-1} (black and green) and 10^{-4} s^{-1} (red and blue). Testing was carried out at room temperature and 200 °C using both strain rates.

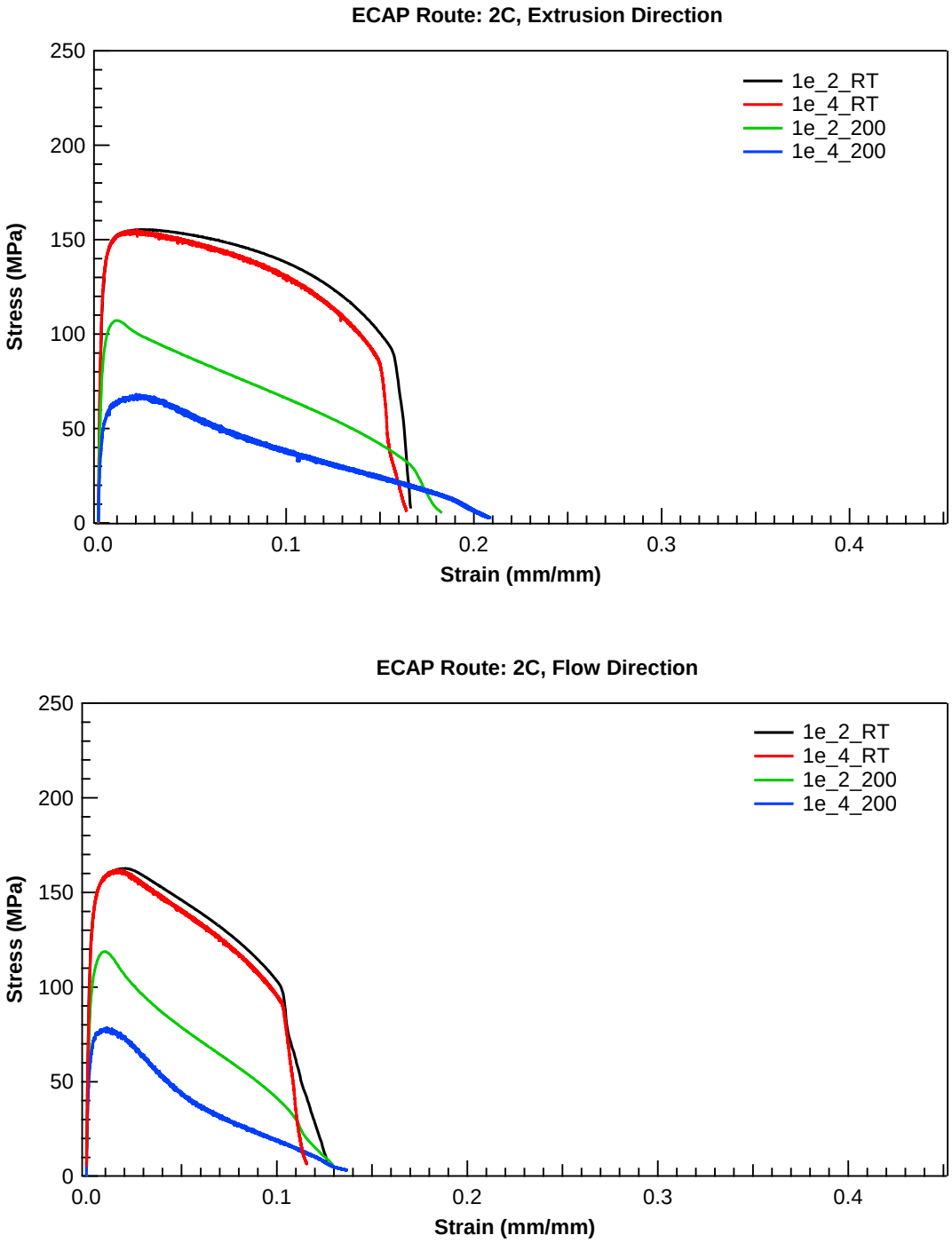

Figure 5 Engineering stress vs. engineering strain plots for Al-1100 ECAPed using route 2C in a) ED and b) FD conditions using strain rates of 10^{-2} s^{-1} (black and green) and 10^{-4} s^{-1} (red and blue). Testing was carried out at room temperature and 200 °C using both strain rates.

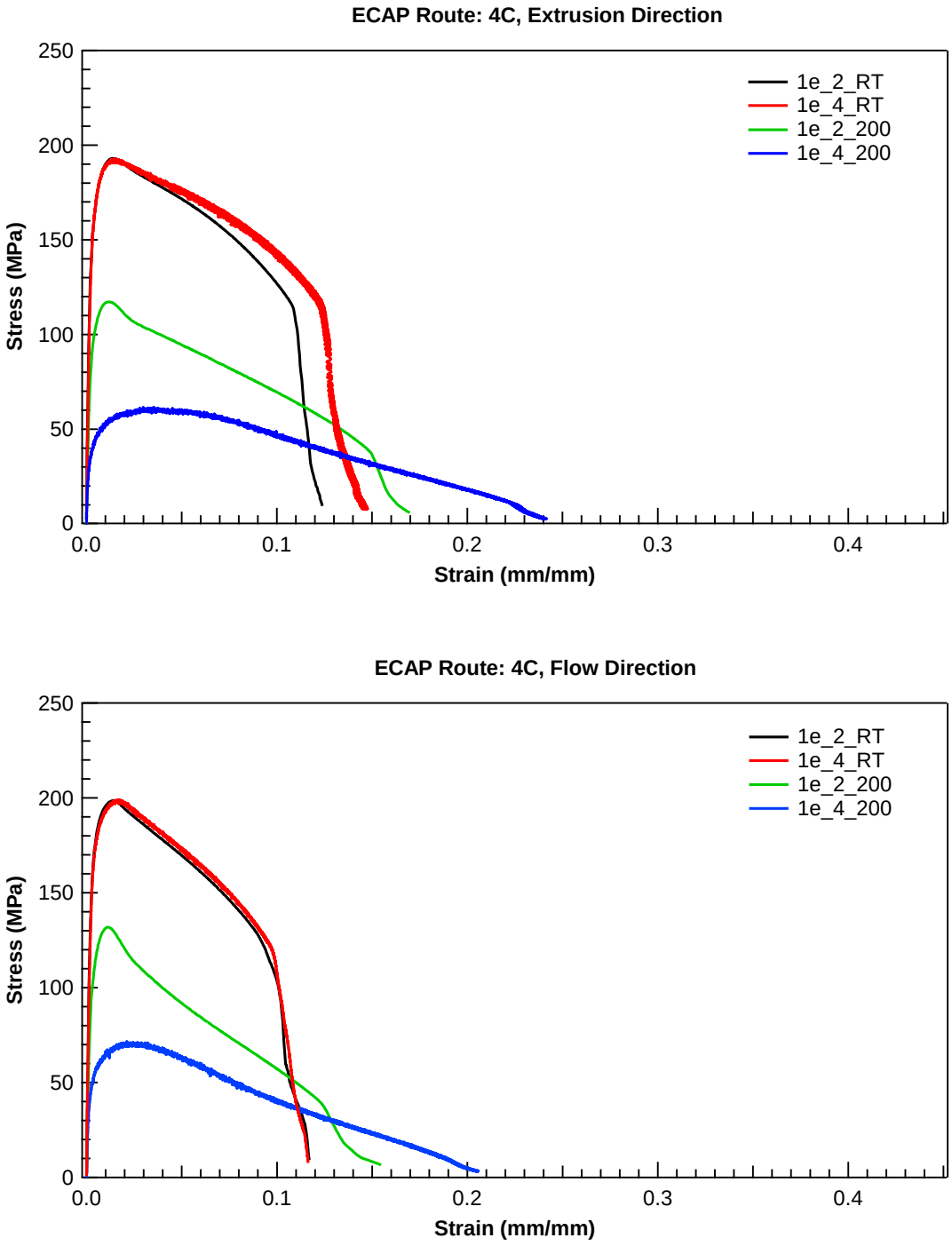

Figure 6 Engineering stress vs. engineering strain plots for Al-1100 ECAPed using route 4C in a) ED and b) FD conditions using strain rates of 10^{-2} s^{-1} (black and green) and 10^{-4} s^{-1} (red and blue). Testing was carried out at room temperature and 200 °C using both strain rates.

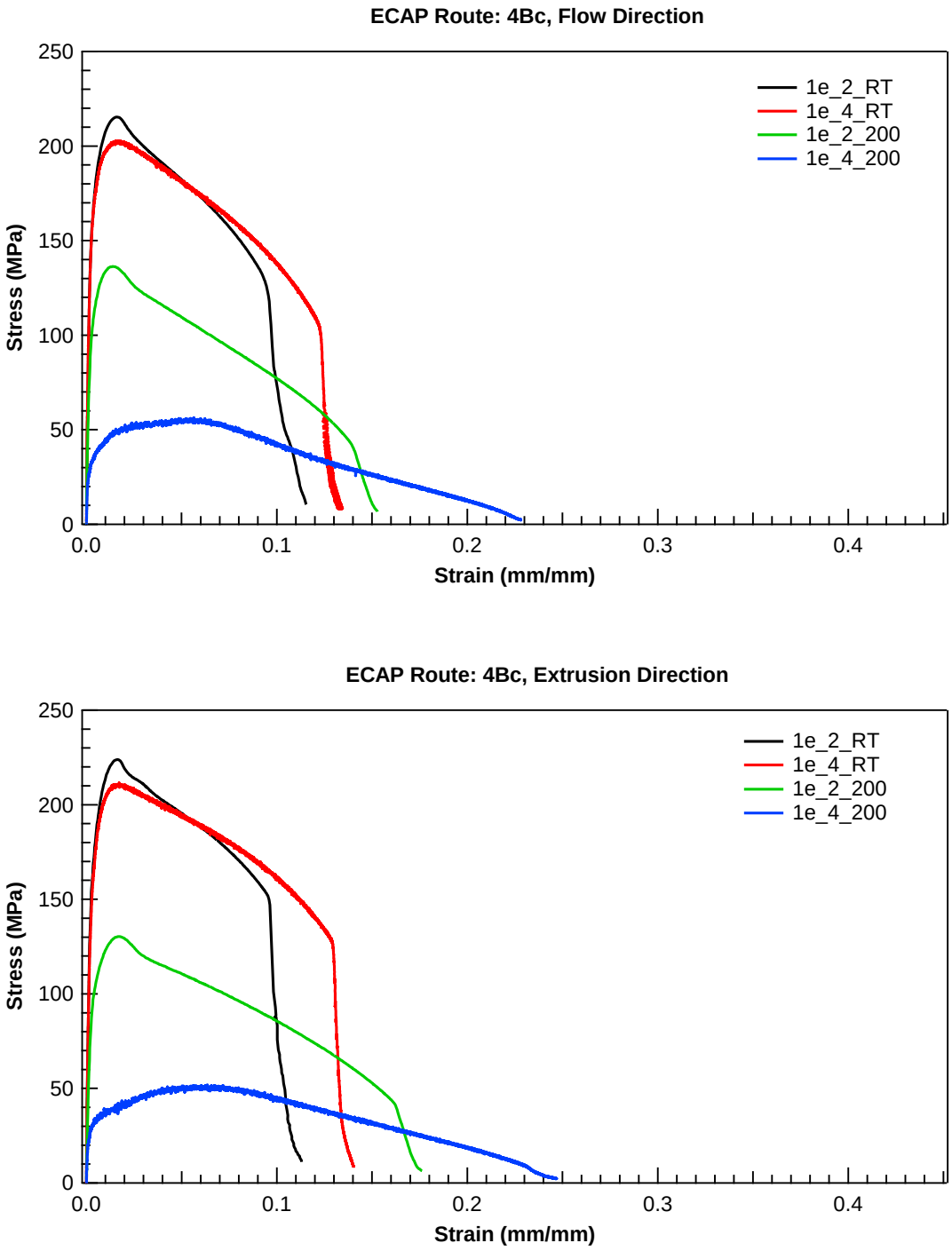

Figure 7 Engineering stress vs. engineering strain plots for Al-1100 ECAPed using route 4Bc in a) ED and b) FD conditions using strain rates of 10^{-2} s^{-1} (black and green) and 10^{-4} s^{-1} (red and blue). Testing was carried out at room temperature and 200 °C using both strain rates.

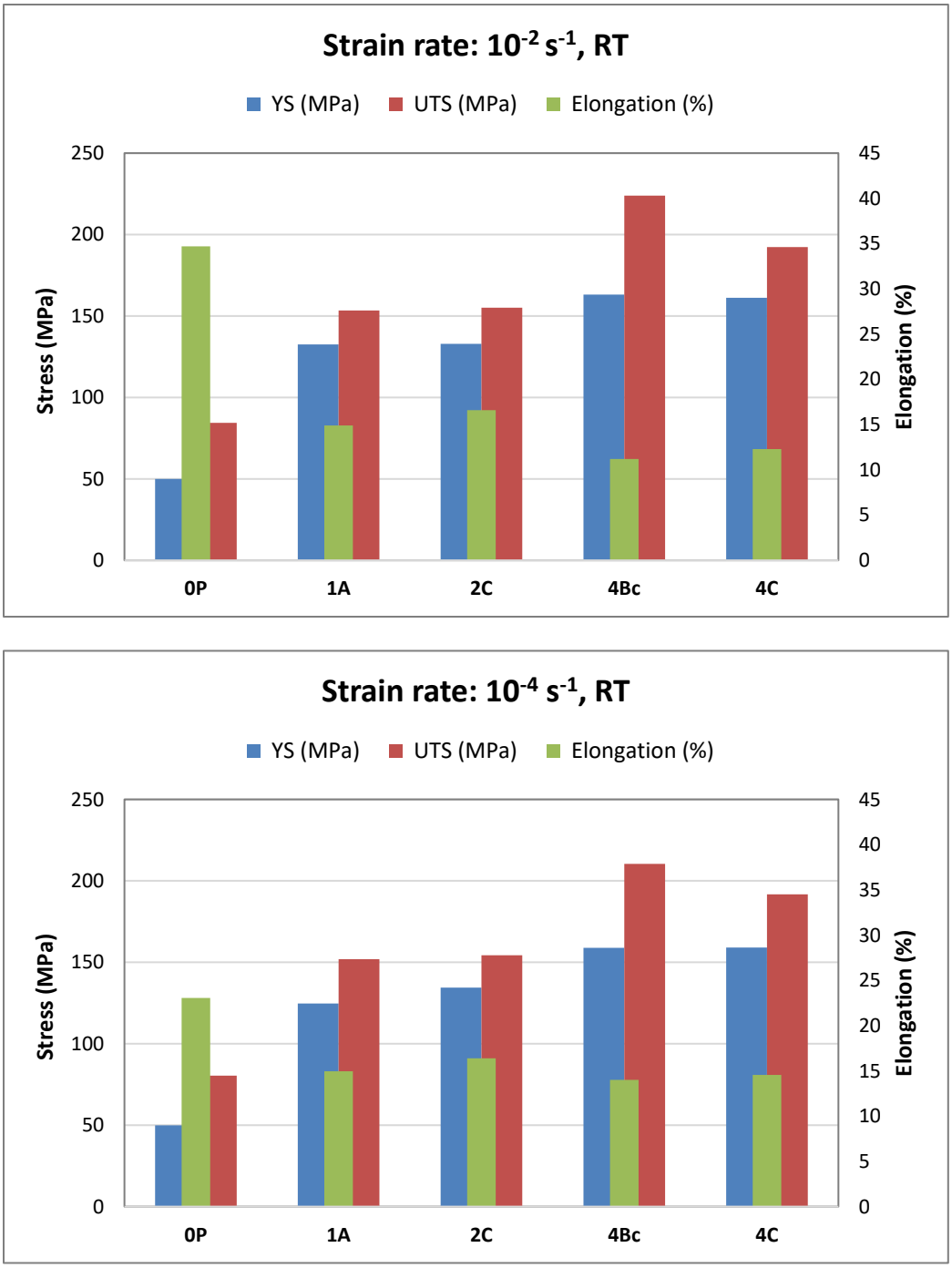

Figure 8 Bar charts with summary of the data (yield strength, ultimate tensile strength and % elongation) from room temperature tensile tests at strain rates of 10^{-2} s^{-1} and 10^{-4} s^{-1}. Only data values from ED tests are shown here.

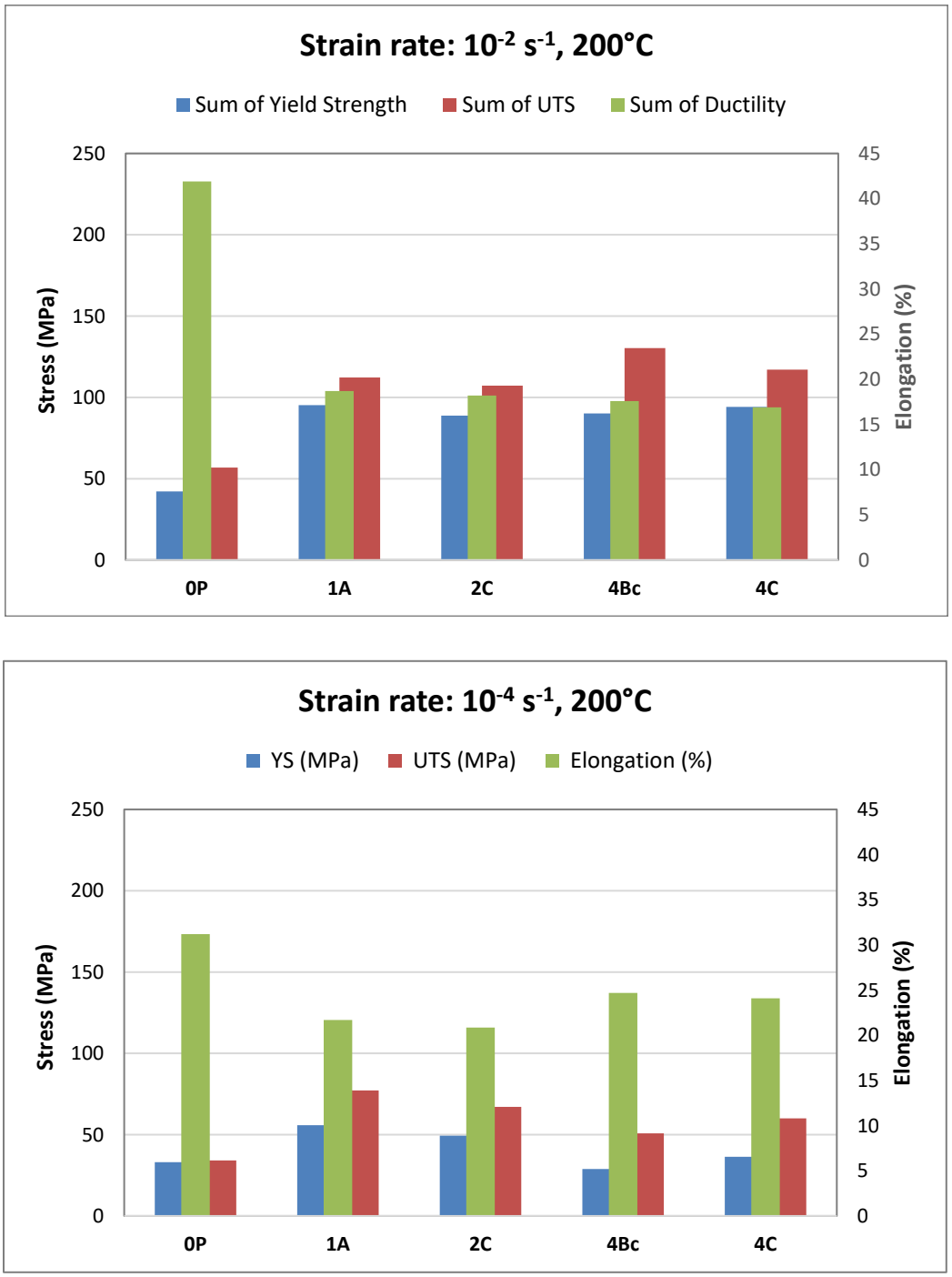

Figure 9 Bar charts with summary of the data (yield strength, ultimate tensile strength and % elongation) from high temperature 200°C tensile tests at strain rates of 10^{-2} s^{-1} and 10^{-4} s^{-1}. Only data values from ED tests are shown here.

The results show an overall expected outcome of high strength with increasing number of passes of ECAP. Bar charts in Figure 8 and Figure 9 summarize data for better comparison of strengths and ductilities with 0P (as-received) condition. The analysis covers the effect of strain rate, temperature, ECAP passes, and ECAP routes, There is negligible strain rate sensitivity at room temperature at all routes/passes as can be seen from similar bar heights of strength in 10^{-2} s^{-1} RT and 10^{-4} s^{-1} RT shown in Figure 8. Significant strain rate sensitivity was observed when the tests were conducted at 200 °C. Bar charts also show that route 4Bc gives better strength and ductility combination compared to other passes. This is in agreement with the literature which established that that four passes by route Bc, impart adequate true strain to promote evolution of dislocation cell structure and sub-grain boundaries into high-angle grain boundaries in different materials [54], [57]. It has also been reported that strong textures can be created using route Bc. Cao et al. [58] studied the texture evolution of commercially pure Al with respect to number of passes using route Bc and found that the texture intensity increases as a function of accumulated strain (i.e. number of ECAP passes).

2.4 Conclusion

Commercially pure Al-1100 was subjected to various ECAP routes/passes. The as-received Al-1100 and ECAPed aluminum were subjected to a number of tensile tests at room temperature and 200 °C using two different strain rates at each temperature. It was evaluated and substantiated by literature that 4Bc ECAP route gives a better combination of strength and ductility at ambient and elevated temperatures and hence, will be used as a primary processing route Al-Er-Sc-Zr-V-Si alloy in subsequent chapters,

CHAPTER III

GRAIN REFINEMENT AND ROLE OF PRECIPITATES ON MICROSTRUCTURE STABILITY AFTER ECAP OF PEAK-AGED AL-ER-SC-ZR-V-SI[1]

3.1 Introduction

Strengthening of materials at room temperature and elevated temperature is a comprehensive subject in materials science with a strong practical importance. The ultimate aim generally is to have materials with high strength-to-weight ratio, in order to achieve better efficiencies in high end applications. Precipitation hardening is one of the most effective strengthening processes which relies on alloying additions and heat-treatments to improve the mechanical response of metallic alloys [3]. Precipitation relies on solutes that have higher solubility at elevated temperatures and decreasing solubility at low temperatures [4].

Scandium containing aluminum alloys are readily used for high temperature applications due to their improved strength, toughness, creep resistance and good electrical properties [6]. The strengthening in these alloys is due to nano-sized and coherent tri-aluminide phases such as Al_3Sc. The mechanism of strengthening at ambient temperature is controlled by dislocation-precipitate interaction. Dislocations bypass the precipitates by shearing or Orowan looping mechanisms [21]. Continuous research in the optimization of the composition has allowed to develop aluminum alloys which can

[1] Reprinted with permission from Malik J. et al. (2018) Equal Channel Angular Pressing of a Newly Developed Precipitation Hardenable Scandium Containing Aluminum Alloy. In: Martin O. (eds) Light Metals 2018. TMS 2018. The Minerals, Metals & Materials Series. Springer, Cham

sustain temperatures as high as 400 °C. This has been made possible by the alloying additions of several rare-earth and transition metal elements that form $L1_2$ ordered trialuminide precipitates [12]. Additions of Zr, Er, and V has been reported to have a profound effect on the coarsening resistance of the precipitates due to their core/shell morphology [13]–[15]. Erdeniz et al. [16] has recently developed an aluminum alloy with micro-additions of Er, Sc, Zr, V, and Si. The authors reported a maximum hardness of ~600 MPa at ambient temperature after optimizing the peak-aging parameters. This is attributed to the precipitation strengthening due to the formation of $L1_2$-ordered Al_3(Sc,Er,Zr,V) nano-precipitates.

In addition to precipitation strengthening, severe plastic deformation (SPD) can be employed to further enhance strength through grain refinement in accordance with the Hall-Petch relationship [25]–[29]. Equal channel angular pressing (ECAP) is a popular SPD technique largely due to its strengthening effectiveness and processing efficiency [30], [36]–[38]. Pre-ECAP aging and post-ECAP aging are the two main processing sequences that are used to optimize the strengthening of precipitation hardenable alloys. In the post-ECAP aging category, many authors have investigated the effect of ECAP on precipitation kinetics and the link between high density of lattice defects and diffusion controlled processes [42]–[44]. In the pre-ECAP aging, major areas of concern are the influences of deformation during ECAP on the precipitates distribution [45], fracturing [46], coarsening/dissolution [47], and subsequent microstructure stability at elevated temperatures.

In this study, a newly developed precipitation hardened Al-Er-Sc-Zr-V-Si alloy by Erdeniz et al. [16], in peak aged condition was subjected to equal channel angular pressing using route 4Bc. It is to be noted that only the effects of ECAP on aged alloy has been reported here. ECAP of the homogenized alloy is another extensive study and will be reported elsewhere. The effect of ECAP on the grain refinement and subsequent improvement in mechanical properties were studied using tensile tests and microhardness contour maps. In addition, thermal stability of ECAPed microstructure was evaluated by taking microhardness measurements after conducting annealing heat treatments at various temperatures. Lastly, scanning electron microscopy (SEM) was used to evaluate the influence of ECAP on precipitate distribution, coarsening/dissolution, and fracturing, if any.

3.2 Experimental Procedure

3.2.1 Alloy production and aging heat treatments

The alloy used in this study is cast aluminum with micro-alloying additions of Sc, Er, Zr, V, and Si. Nominal composition of Al–Sc–Er–Zr–V–Si is given in Table 2. The detailed casting procedure for this alloy has been reported in the previous study [16]. Three as-cast billets were solution-treated at 640 °C for 4 h. One of the billets was kept in the homogenized (H) state for reference. The other two billets were aged using a two-step aging treatment of 350 °C / 16 h followed by 400 °C / 12 h. The effectiveness of this double aging treatment has been previously reported by Erdeniz et al. [16]. All heat-treated billets were quenched in water to terminate the treatment.

Table 2 Composition in at. %, of alloying additions in aluminum.

Sc	Er	Zr	V	Si	Al
0.013	0.007	0.071	0.074	0.054	Bal.

3.2.2 ECAP processing

One of the two aged billets was subjected to ECAP at room temperature, with a pressing speed of 1 mm/min, using a 90° die channel. This billet will be referred as PA-ECAP. Aluminum foil wrapping was used to reduce the friction between the billet and the die. The schematic of ECAP process is shown in Figure 10. Three directions (extrusion, normal and flow direction) and their corresponding orthogonal planes are also given in the figure. Only flow plane was used for microstructure characterization and microhardness measurements. Route Bc with four passes was utilized in this study, which corresponds to the rotation of billet by 90° after each pass. This particular route was selected based on its

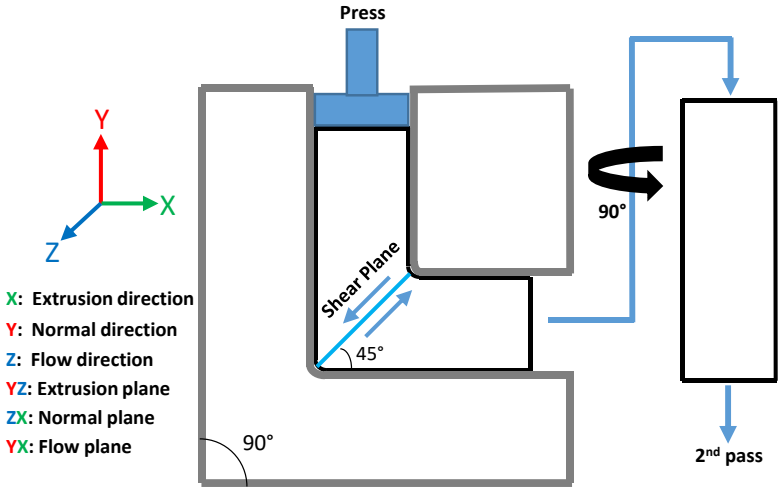

Figure 10 Schematic of an ECAP process illustrating orthogonal directions and planes. For route Bc, the billet was rotated 90° along y-axis, after each such pass as shown above.

established efficacy in obtaining uniform ultra-fine grain structure with high angle of misorientation as reported by several researchers for a range of different metallic alloys including aluminum [29], [59], [60]. Furthermore, four and more passes can accumulate sufficient strains to induce high-angle grain boundaries [54].

3.2.3 Mechanical characterization

Room temperature tensile tests and Vickers microhardness measurements were carried out on three specified conditions: 1) Homogenized only (H), 2) Peak-aged (PA), and 3) Peak-aged followed by ECAP (PA-ECAP). Tensile tests were conducted at a constant strain rate of $1x10^{-3}$ s^{-1} using an electromechanical MTS Insight 30 kN machine. Schematic of the miniature tensile specimen used in this study is given in Figure 11. Two specimens were tested at this condition to ensure repeatability.

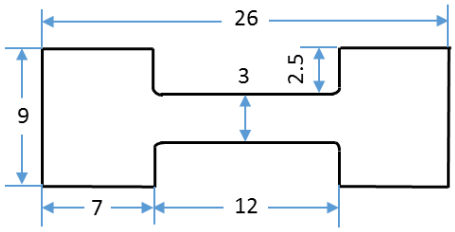

Figure 11 Sketch with dimensions of a miniature specimen used for tensile testing. All dimensions are in millimeters.

To study the hardness distribution and homogeneity, microhardness measurements on above-mentioned three conditions were carried out using 50 gf load and an indentation time of 10 s. Specimens of size 1 x 1 cm size were cut and polished down to 1 µm diamond polish to obtain a mirror-like finish. A grid profile was made with 1 mm step size in both x and y directions and then represented using contour plots.

Microhardness measurements after annealing heat treatments on PA and PA-ECAP specimens were taken to evaluate the thermal stability and grain coarsening resistance at elevated temperatures. Annealing heat treatments were carried out using the temperature range from 50 to 550 °C with 50 °C increments and holding time of 3 h at each temperature. In some limited cases, annealing data from an ECAPed (route 4Bc), commercially pure aluminum alloy (Al-1100) was included as a reference.

3.2.4 Microstructure characterization

All specimens for microstructure characterization were cut from the center of the cast billet and the flow plane of the ECAPed billet, using electro discharge machining. Specimens were ground down to 1200 grit size, followed by polishing using 3 and 1 µm diamond paste and 0.04 µm colloidal silica. Optical microscopy was employed to measure the grain sizes of H and PA specimens. Specimens were etched using Keller's reagent (20 mL HNO_3, 20 mL HCl, 5 mL and 20 mL H_2O) and observed under the light microscope to reveal the grain boundaries.

EBSD analysis was performed to observe the microstructural changes and obtain a map of grain size and orientation after ECAP. A FERA SEM with an EBSD attachment was used for mapping. The PA-ECAP specimen of area 25 x 25 µm was scanned using at a step size of 0.1 µm. Map noise reductions was conducted to the fifth degree before grain size and misorientation measurements. In addition, a FEI Quanta 400 SEM was employed to study the distribution of precipitates in the annealed PA-ECAP specimens and to explain their role in maintaining thermal stability. Imaging was done using a backscattered electron detector and an accelerating voltage of 20.0 kV.

3.3 Results and Discussions

The comparison of grain sizes in the optical images of H and PA, and EBSD map of PA-ECAP specimens are shown in Figure 12. Average grain size of H is 411 ± 232 µm and of PA is slightly coarser, 656 ± 385 µm. Larger grain size in PA was caused by the two-step aging treatment after homogenized condition. Another observation on H and PA micrographs is the subgrain structure seen (approximately 40 µm) in some of the grains, which may have been caused by the remnant primary precipitates that formed during solidification. These precipitates may inhibit recrystallization during the homogenization and aging treatments, as stated in previous studies [61], [62]. EBSD maps of the flow plane of PA-ECAP is shown in Figure 12c. Color mapping orientation was with respect to the Z direction for each sample (out of the page). Ultrafine grain size of 0.78 ± 0.44 µm was obtained after ECAP. Grains and sub grains can be clearly seen oriented and elongated along the shear plane.

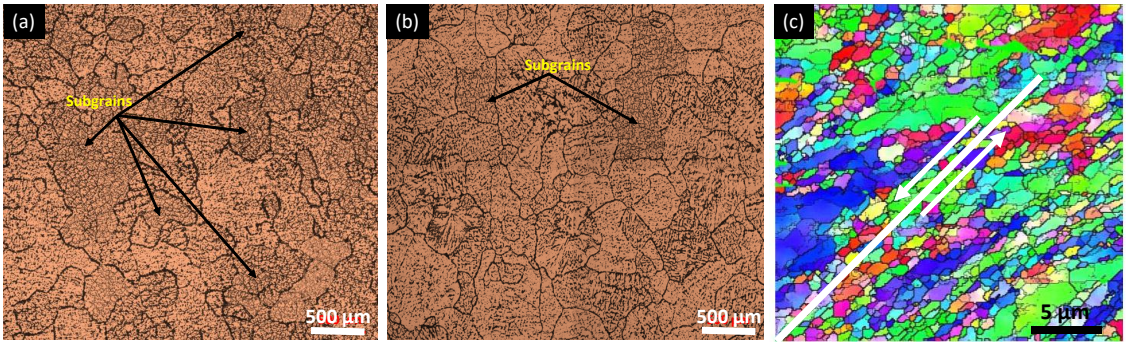

Figure 12 Optical micrographs of a) Homogenized (H) and b) Peak-aged (PA) specimens, at a magnification of 5X. EBSD map of c) PA-ECAP (flow plane) specimen, showing grains oriented along the shear plane. Theoretical shear plane at 45° is shown by white line in c).

Table 3 Summary of the results from tensile tests, microhardness measurements and microstructure analysis.

Designation	Yield strength at 10^{-3} s^{-1} strain rate (MPa)	Elongation at 10^{-3} s^{-1} strain rate (%)	Mean microhardness (HV)	Average grain size (µm)
H	50.7	31.6	29.4	411 ± 232
PA	115.6	24.2	52.4	656 ± 385
PA-ECAP	178.3	10.4	62.3	0.78 ± 0.44

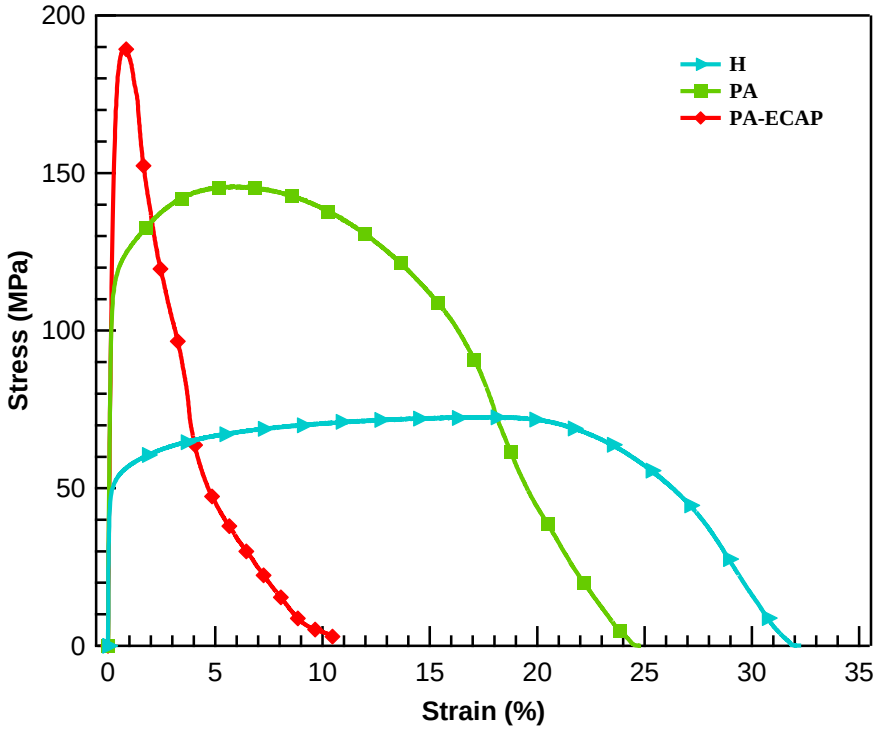

Figure 13 Tensile tests at a constant strain rate of 10^{-3} s^{-1} for three different processing conditions. A general trend of high yield stress and low ductility is observed after successive strengthening processes.

Room temperature stress vs. strain plots obtained at a constant strain rate of $1x10^{-3}$ s^{-1}, are shown in Figure 13. The relevant values of tensile data are given in Table 3. Three cases of strengthening can be seen here: 1) Solute strengthening (H), where most of the alloying elements are present in the form of a solid solution. The strength is low and mainly due to the interaction of dislocation with solute atoms, but large ductility of 31.6 % is obtained. 2) Precipitation strengthening (PA), where most of the solute atoms have precipitated out after aging treatments, in the form of tri-aluminide precipitates. These precipitates are elastically hard, coarsening resistant and coherent in nature, and exhibit high strength due to elastic interactions exerted by the mismatch in lattice parameter and precipitate-matrix modulus [63]. As a result, we see 2.3 times increase in yield strength as compared to the homogenized (H) condition, along with noticeable work hardening, and 6 % decrease in ductility. 3) Combination strengthening (PA-ECAP), where major source of strength is due to grain refinement, in accordance with Hall-Petch relationship, and some contribution is possibly due to the precipitate hardening. Consequently, maximum yield strength of 178.3 MPa was obtained at the expense of ductility. The decrease in ductility with increasing strength is due to insufficient strain hardening, as explained by Y.M Wang and E. Ma [64].

Figure 14 shows the contour plots of microhardness of the three conditions. This was done to illustrate the microhardness homogeneity after aging and ECAP. A very small microhardness spread of 27 – 30 HV in H shows that the primary precipitates which may have formed during solidification and remained undissolved during the homogenization treatment, have negligible effect on localized or overall strengthening. For PA specimen,

the microhardness distribution across the cross-section ranging from 48 – 55 HV, indicates slight inhomogeneity with high values at some local points, highlighted in orange color on the contour map. After ECAP there is homogeneity in the microstructure with microhardness distribution in the range of 59 – 63 HV. This is mainly attributed to the uniform grain refinement after ECAP. Cheng Xu et al. [65] studied the hardness homogeneity after ECAP in aluminum and its alloy and concluded that it gradually increases with number of passes.

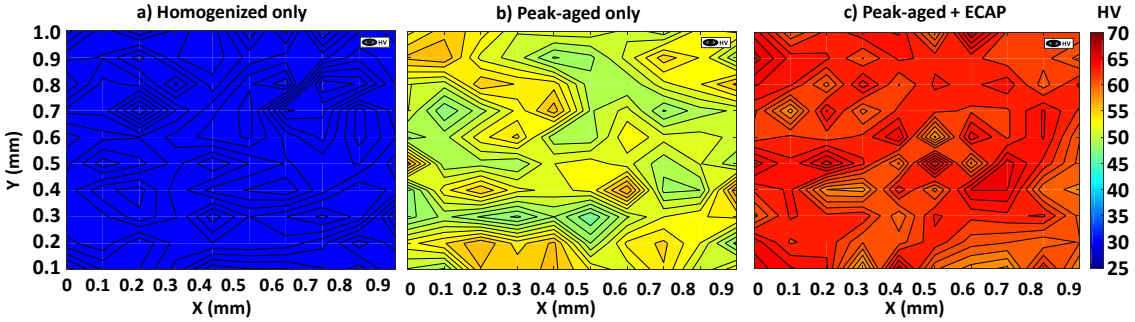

Figure 14 Contour plots showing Vickers microhardness distribution in 1 x 1 cm cross-section of a) H, b) PA, and c) PA-ECAP.

Figure 15 shows the annealing heat treatment curves for PA, PA-ECAP and Al-1100-ECAP. Pure aluminum alloy shows a sudden drop in microhardness after annealing at 150 °C for 3 h, followed by a sharp drop to 30 HV after 250 °C for 3 h, and ultimately reaching the nominal microhardness of 25 HV after 400 °C / 3 h. This trend is quite expected and is mainly due to rapid recrystallization and grain growth during annealing. Contrasting trend of microhardness can be seen in the newly developed alloy in PA and PA-ECAP conditions. PA shows slight increase up to 100 °C, thereafter displays a fairly small decrease in microhardness up until 400 °C. Sharp drops in microhardness beyond

400 °C corresponds to coarsening and dissolution of precipitates [9]. Nevertheless, annealing trend of PA indicates the potential of precipitates in maintaining the strength of the alloy when exposed to elevated temperatures. PA-ECAP alloy has fine grain structure and homogenous distribution of precipitates after ECAP, as illustrated by EBSD map and microhardness contour plots. Annealing heat treatments on PA-ECAP shows a slight increase in microhardness at 150 °C and thermal stability up until 250 °C. The main difference between PA-ECAP and Al-1100 is of course the presence of finely distributed, nanosized, coarsening resistant tri-aluminide precipitates. Thus, it is evident that when exposed to elevated temperatures these precipitates play a role of inhibiting, restraining and delaying the grain growth, therefore maintaining the combined strengthening [62].

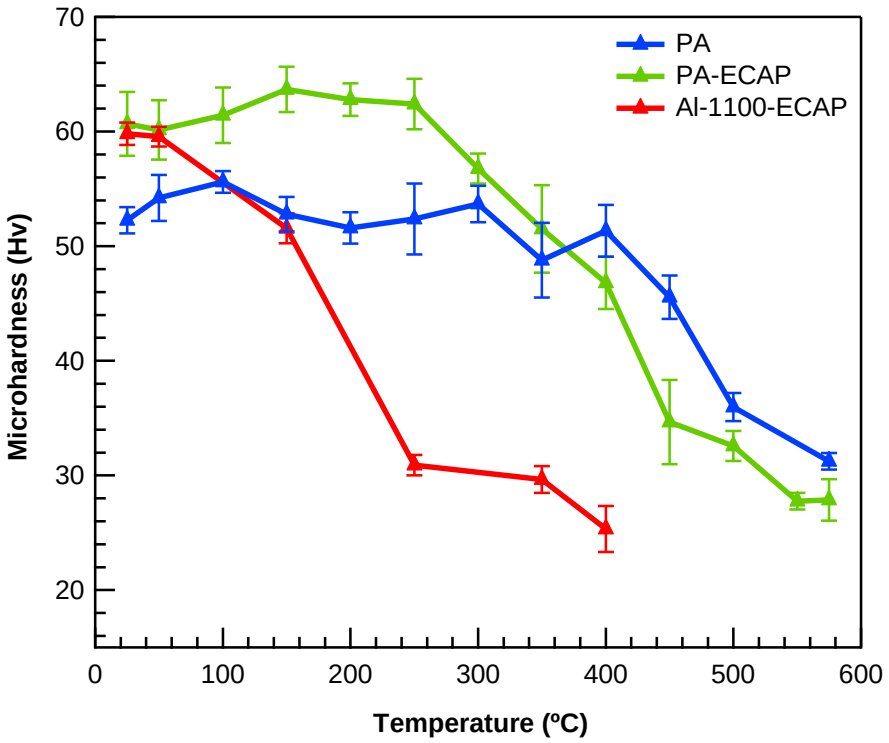

Figure 15 Microhardness measurements after annealing heat treatments on PA-ECAP and Al-1100-ECAP. Commercially pure Al-1100 was also ECAPed using route 4Bc and used here as a reference.

Microhardness eventually drops at temperatures greater than 300 °C, this is due to concurrent recrystallization, grain growth, and to a lesser extent, precipitate coarsening at elevated temperatures.

Size and distribution of precipitates after annealing at given temperatures is shown in Figure 16. All the SEM images are captured from the flow plane of the ECAPed billet. The arrangement of precipitates follows a definite trend and are distributed along the shear plane, which is at ~45° angle from the longitudinal plane as illustrated in Figure 16a. Elongated grains in the same direction are also visible (Figure 16d). The precipitates can also be seen decorating along the grain boundaries, more prominently in Figure 16e, 7f. These precipitates play a significant role in restraining the grain growth during annealing, thus maintaining the thermal stability of the microstructure. Precipitates sizes in these alloys are in the range of 50 – 500 nm, although sizes observed in previous studies are in the range of 10 – 100 nm [6], [13], [66]. Due to the fine scale of precipitates, the true number density of precipitates cannot be resolved in Figure 16a-d. These precipitates become visible at higher temperatures (Figure 16e-f) as a result of coarsening. Though, no evidence of fracturing or dissolution was observed in any case. In-depth TEM analysis may be required to have a better estimation of the precipitate number density. In addition to TEM analysis, it would be interesting to research how the precipitates evolve during ECAP and post-ECAP aging of a homogenized Al-Er-Sc-Zr-V-Si alloy. We expect a

significant increase in precipitation kinetics after ECAP of a supersaturated alloy. This is currently the focus of another ongoing study.

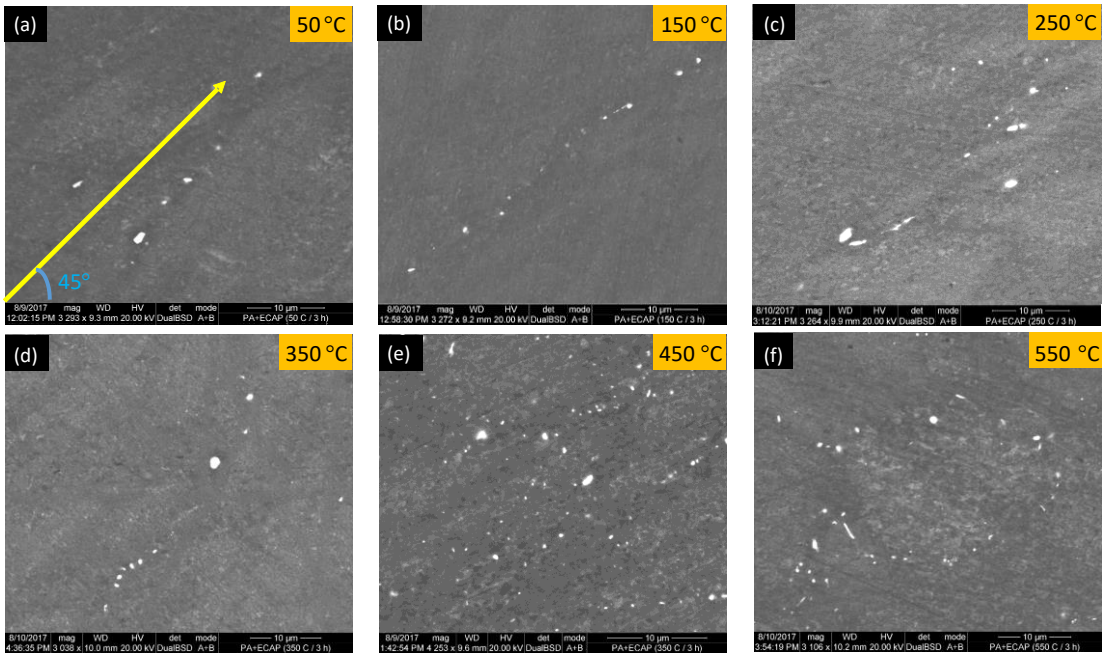

Figure 16 Scanning electron microscopy images after various step of annealing heat treatment. At each temperature, the specimen was held for 3 h and then quenched in water.

3.4 Conclusions

The effect of ECAP on the grain refinement and subsequent improvement in mechanical properties of Al-Er-Sc-Zr-V-Si alloy was studied using tensile tests, microhardness contours, heat treatments and microscopic imaging. Following conclusion can be drawn from this study:

1. Grain size refinement from 656 ± 385 μm to 0.78 ± 0.44 μm resulted after ECAP. Extensive subgrain formation was observed. Grains were oriented along the shear plane.
2. Enhancements in mechanical properties after ECAP was as expected, with a ~55 % increase in yield strength from peak-aged condition. This was attributed to the combined strengthening due to grain refinement and precipitate hardening. However, insufficient strain hardening capability resulted in the reduction of ductility.
3. Homogenous microstructure and distribution of precipitates after ECAP of peak-aged specimen resulted in hardness homogeneity across the specimen.
4. Annealing heat treatments show that precipitates play a vital role in maintaining microhardness by inhibiting and restraining grain growth at elevated temperatures. Therefore, the ECAPed alloy maintains thermal stability up to 250 °C / 3 h.

CHAPTER IV

DYNAMIC PRECIPITATION IN VANADIUM MICRO-ALLOYED AL-ER-SC-ZR-SI ALLOY DURING EQUAL CHANNEL ANGULAR PRESSING

4.1 Introduction

There is an ever-increasing demand for lightweight, high performance, corrosion resistant metallic alloys [67]. In particular, alloys that offer high specific stiffness and strength at ambient temperature and superior creep resistance at elevated temperature are highly sought after by various industries [1][2]. Therefore, an important practical goal is to develop new lightweight alloys and design optimal thermomechanical processing routes to further improve their mechanical properties and enhance performance at a suitable cost.

Scandium containing aluminum alloys are heat-treatable, precipitation-hardenable alloys [6], [7]. They contain coherent, finely distributed, hard, $L1_2$ ordered, nanosized Al_3Sc tri-aluminide precipitates that contribute to ambient temperature strength by either precipitate shearing or Orowan looping mechanism [6]. In addition, these Al_3Sc precipitates provide potent coarsening resistance and enable the use of Al-Sc alloys to significantly higher temperatures of up to 350 °C, as compared to conventional age-hardenable 2xxx and 6xxx series Al alloys [6]–[8]. Mechanical properties of Al-Sc alloys can be improved by ternary additions with rare earth or transition metals that partially substitute the rather expensive Sc to produce more coarsening resistant, coherent, $Al_3(Sc_{1-y}X_y)$ precipitates [9]–[11]. In fact, partial substitution of Sc by faster diffusing components such as Er, Zr and Yb results in the formation of core-shell morphology tri-

aluminide precipitates. First, a core forms which is rich in the highest diffusivity element, followed by the slower development of a Sc-rich Al_3(Sc, X) shell. The shell acts as a diffusion barrier and it slows down the rate of precipitate coarsening. In quaternary Al-Er-Sc-Zr alloys, multiple shells form and Zr promotes the formation of the final shell of such core/shell/shell precipitates. [10], [13]–[15].

In our recent work with Erdeniz et al., we reported on the development of a vanadium micro-alloyed Al-Er-Sc-Zr-Si alloy [16]. This system, after a suitable double-aging heat treatment, exhibited a peak microhardness of ~600 MPa at ambient temperature. This strength level was linked to a fine dispersion of nanosized, core-shell morphology, vanadium containing Al_3(Sc,Er,Zr,V) precipitates. In addition, the alloy also showed significant creep resistance up to 400 °C, which was linked to potent grain growth resistance provided by its unique, core-shell morphology, tri-aluminide precipitates. In this work, the potential of further enhancing mechanical properties of the Al-Er-Sc-Zr-Si-V alloy by severe deformation and subsequent heat treatments is explored.

Equal channel angular pressing (ECAP) is a well-known severe plastic deformation technique that routinely produces ultra-fine grained materials from bulk [30]–[32]. ECAP offers the ability to refine microstructure and manipulate texture in a range of different alloys [33]–[35]. UFG materials with wrought microstructure exhibit improved strengths and fatigue life at ambient temperature, and can even be superplastic at elevated temperatures [68], [69]. ECAP of precipitation hardenable lightweight alloys is more attractive because it further enhances the potential of such alloys for high performance industrial applications.

A growing body of literature has shown, precipitation kinetics, size, morphology and distribution of precipitates and second phase particles in the matrix of processed material, critically depend on the ECAP temperature and route [42]–[44], [70]–[72]. Researchers have either focused on achieving grain refinement in the precipitation hardenable alloys, first, and later, applied an aging heat treatment to achieve precipitation in the material. The other possibility that has received some attention is to start with a supersaturated alloy i.e. after an appropriate homogenization scheme, conduct ECAP at elevated temperatures and study the in-situ dynamic precipitation and its effect on the resulting mechanical properties. The literature on severe plastic deformation of heat-treatable aluminum alloys indicates post ECAP aging at a temperature much lower than the usual aging temperature, can yield superior strength by taking benefit of both grain-size effect and precipitates [48]. Sordi et al. studied the precipitation kinetics in an Al-Ag alloy [46]. They reported that diffusion kinetics accelerated rapidly after ECAP due to the presence of defect structure, comprising mainly of grain boundaries, sub-grains, and dislocations. Kim et al. compared pre-ECAP and post-ECAP aging of 6061 Al alloy [49]. They found post-ECAP aging to be more effective compared to the aging of unpressed material. However, they used a low aging temperature to suppress the recrystallization and growth during heat treatment. Contrary to the favorable aspects of post-ECAP aging, Fare et al. reported small but continual decrease in microhardness after aging of ECAPed Al-Mg-Si alloy at 180 °C [44].

The influence of thermodynamic state of the material prior to ECAP i.e. supersaturated/ homogenized, peak-aged or overaged condition; in such scheme of things

has also received some attention [71], [73]. It is also reported, that during severe plastic deformation dynamic precipitation can occur in various precipitation hardenable aluminum alloys [43], [74]–[76]. The question however still is, can we concurrently achieve deformation driven grain-size strengthening and dynamic precipitation strengthening and to what extent?

In this paper, we report on the effect of ambient temperature ECAP by route 4Bc on precipitation microstructure and mechanical properties of a supersaturated Al-Er-Sc-Zr-V-Si alloy. We carried out a detailed analysis by comparing pre- and post-ECAP aging response to reveal the relationship between strength and the nature, extent, and thermal stability of tri-aluminide precipitates.

4.2 Experimental

4.2.1 Materials and Processing

The material used in this work is a cast Al-Er-Zr-Si alloy micro-alloyed with vanadium. Its nominal composition is mentioned in Table 4 [16]. The as-cast billets were solution heat treated at 640 °C for 4 hours followed by water quenching to create the homogenized (H) i.e. the supersaturated condition. The homogenized billets were later subjected to one of the following treatments: (a) A two-step aging treatment to achieve the peak-aged (PA) condition. The details of the two step peak-aging treatment, selection of temperatures and durations for this particular Al alloy are discussed in detail in our previous work [16]. The first step was to conduct aging at 350 °C for 16 h, followed by a 2nd aging step at 400 °C for 12 h. All heat treatments were conducted in air and terminated by water quenching. This two-stage peak-aging treatment was critical to obtain a fine

dispersion of vanadium containing tri-aluminide precipitates in the material. (b) Both homogenized (H) and peak-aged (PA) billets were ECAPed to create homogenized followed by ECAP (H-ECAP) condition, and peak aged followed by ECAP (PA-ECAP) condition.

Table 4 Composition of Al-Er-Sc-Zr-V-Si alloy (at. %).

Sc	Er	Zr	V	Si	Al
0.013	0.007	0.071	0.074	0.054	Bal.

ECAP was carried out at ambient temperature in a 90° channel die, using route 4Bc with a pressing speed of 1 mm/min. The ECAP work-piece dimension in each case were 25.4 mm x 25.4 mm x 152.4 mm. Prior to ECAP, aluminum foil was wrapped on the work-piece to reduce friction between the work-piece and the die. In route 4Bc, a work-piece undergoes four ECAP passes with successive 90° rotations along its longitudinal axis after each pass. We choose route 4Bc because of its ability to efficiently produce UFG microstructure with high angle of misorientation [29]. A plethora of ECAP studies have conclusively shown that four passes by route Bc, impart adequate true strain to promote evolution of dislocation cell structure and sub-grain boundaries into high-angle grain boundaries in different materials [54], [57]. It has also been reported that strong textures can be created using route Bc. Cao et al. [58] studied the texture evolution of commercially pure Al with respect to number of passes using route Bc and found that the texture intensity increases as a function of accumulated strain (i.e. number of ECAP passes).

In the remainder of the text, the four different processed conditions of this alloy will be referred to as: homogenized (H), peak aged (PA), homogenized followed by ECAP (H-ECAP), and peak aged followed by ECAP (PA-ECAP). This material designation is summarized in Table 5 for the readers benefit.

Table 5 Material designation and processing condition of four different states of the alloys.

Material Designation	Processing Condition
H	Homogenized only
H-ECAP	Homogenized, followed by ECAP
PA	Peak-aged only
PA-ECAP	Peak-aged, followed by ECAP

*Initial homogenization treatment at 640 °C / 4 h is same for all alloys.

4.2.2 Microstructural characterization

Microstructure examination was carried out on metallographic samples sectioned using Electro Discharge Machining (EDM), from the center of unpressed billets parallel to the flow planes, containing normal direction (ND) and extrusion direction (ED), for both ECAPed conditions. The H and PA samples observed by optical microscopy. They were mechanically ground and polished using standard methods and then etched using Keller's reagent (20 ml HNO_3, 20 ml HCl, 5 ml HF and 20 ml DI H_2O). A Zeiss Axiovert 40 Mat optical microscope was used to observe the grain structure, while a Zeiss Stem 2000-C stereo optical microscope was employed for metallography where a higher depth of field was warranted.

The ECAPed samples (H-ECAP and PA-ECAP) were analyzed by Electron backscatter diffraction (EBSD) to evaluate grain size, grain orientations, and the nature of sub-grains. The EBSD specimens were polished sequentially on a silk cloth with 3 μm diamond suspension, a nylon cloth with 1 μm diamond suspension, and a synthetic velvet cloth with 0.25 μm diamond suspension. The final polishing step used a 0.05 μm colloidal silica solution on MultiTex cloth. The specimens were sonic-cleaned in anhydrous alcohol and rotated 90º between each step. The polishing was continued until all the scratches from the previous step were eliminated. The final step was continued until Kikuchi patterns were observed. EBSD analysis was performed using a FERA SEM with an EBSD attachment for mapping. Scans were carried out at an area of 25 x 25 μm utilizing a step size of 0.1 μm. All scans were run with an accelerating voltage of 20 KeV and at a probe current of ~10 nA. Map noise reductions were carried out before taking grain size measurements. Oxford Instruments' Channel 5 software was used for all map noise reductions and analyses.

FEI Techna transmission electron microscope (TEM) operating at 120 keV was employed to observe the nano-scale precipitates. TEM samples were prepared by starting from ~1.5 mm thin slices cut from the representative billets. The slices were subsequently ground by mechanical means to less than 100 μm thickness. Discs of 3 mm diameter were punched from the ground specimens and twin-jet electro-polished in 30 vol. % HNO_3 + 70 vol. % CH_3OH electrolyte at -10 °C, utilizing a 10 Vdc potential. Additional, Transmission electron microscopy (TEM) characterizations were carried out using an FEI Talos F200X TEM working at 200 kV. The TEM samples were prepared using the lift-

out technique in a FEI Versa 3D LoVac FIB-SEM Dual Beam system equipped with a FEI EasyLift system.

4.2.3 Isochronal and isothermal heat treatments

The difference between pre- and post-ECAP aging response of homogenized condition was characterized by isochronal and isothermal heat treatments. The isochronal aging treatment was conducted in the temperature range of 100 to 575 °C with 50 °C increments and a hold time of 3 h at each temperature step. The isothermal aging treatment was conducted at 400 °C for durations up to 507 h. All heat treatments were conducted in air and terminated by water quenching.

4.2.4 Mechanical characterization

Vickers microhardness was measured for all four conditions. In addition, periodic microhardness measurements were made after each step of isochronal and isothermal heat treatments in order to evaluate and compare the effect of precipitate evolution on microhardness. Specimens were ground and polished to 1µm finish using diamond paste prior to micro-indentation tests. At least 10 indentations were recorded per specimen by employing a 50 gf load and a dwell time of 15 s.

Room temperature tensile tests were performed, at a constant initial strain rate of 1x10-4 s-1. The specimens for tensile testing were cut using EDM from the middle sections of unpressed billets and along the extrusion direction (ED) of ECAPed billets. The size and dimensions of miniature tensile specimens used in this study are provided later in the text along with tensile results. The tensile tests were performed on MTS Insight 30 kN machine by using a contact extensometer to maintain constant strain rate during

tensile deformation and is expected to be consistent until necking. At least, two specimens were tested for each set of conditions to ensure statistical reliability.

4.2.5 Calorimetry Investigations

Calorimetry techniques are extensively applied to understand the phase transformations, homogenization, recrystallization, and solid state reactions such as precipitation [77]. A LabsysTM TG-DSC manufactured by SETARAM was used to perform differential scanning calorimetry (DSC) and differential isothermal calorimetry (DIC) analysis on H and H-ECAP conditions. The specimens for DSC and DIC were cut from the billet and trimmed down to around 25 mg mass. The weight of each sample was measured by Semi Micro Balance CX205 with an accuracy of ±0.03 mg. Each specimen was initially equilibrated at 25 °C for 5 min and a 20 ml/min nitrogen flow was used in all the experiments. DSC was performed at 20 °C/min for up to 600 °C. For DIC experiments, specimen temperature was ramped up to 400 °C at a rate of 20 °C/min, it was then held at this temperature for 24 h. The DIC experimental parameters were selected such that they mirror the 400 °C static aging heat treatment. In all cases, a multi-peak fitting analysis by IGOR software was carried out on the DSC and DIC data for base line correction.

4.3 Results

4.3.1 Microstructural characterization

Microstructures of all four conditions were analyzed for grain size and misorientation angle, precipitate size and distribution, using optical and electron microscopy. Figure 17 and Figure 18 displays a collage of optical micrographs and stereomicroscope images of H and PA condition, etched using Keller's reagent. The

microstructure of homogenized alloy has an equiaxed grain size of 420.7 ± 183.0 µm. Peak-aging heat treatment on this condition further grows the grains to 709.4 ± 464.7 µm, as shown in Figure 18.

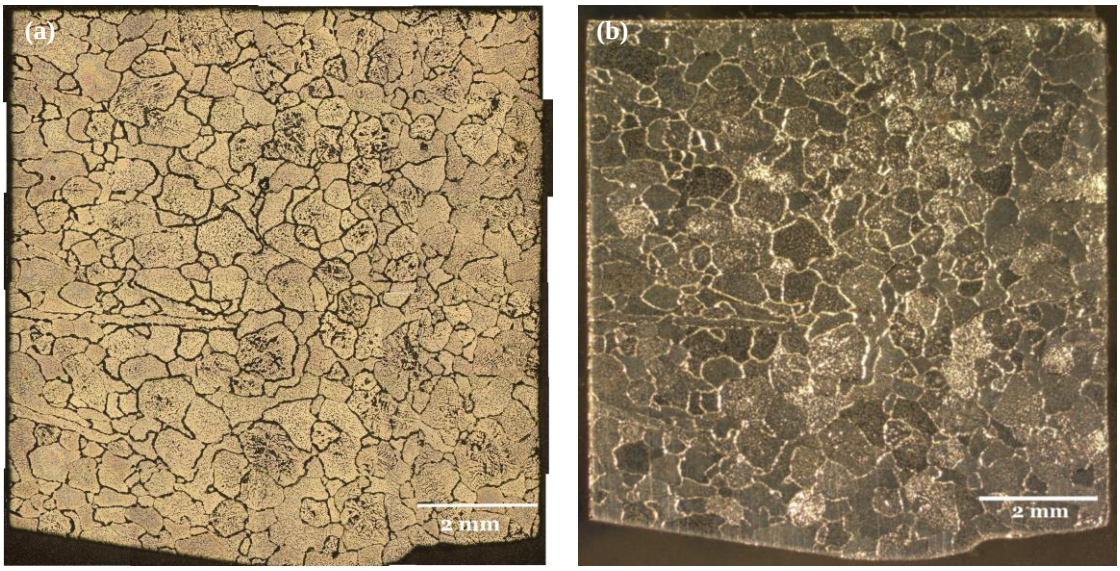

Figure 17 (a) Optical and (b) Stereomicroscope images of homogenized condition (H) showing equiaxed grain size of 420.7 ± 183.0 µm.

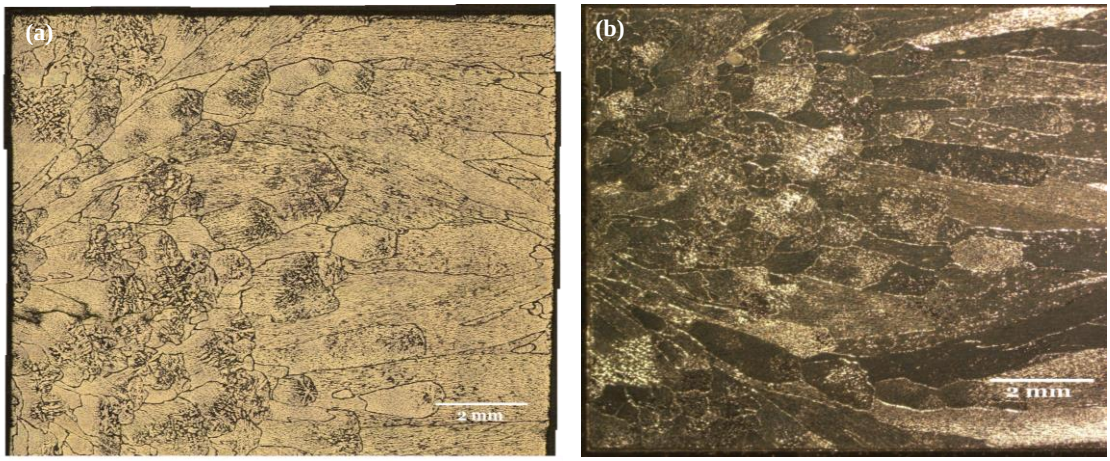

Figure 18 (a) Optical and (b) Stereomicroscope images of peak-aged condition (PA) showing grain size of 709.4 ± 464.7 µm.

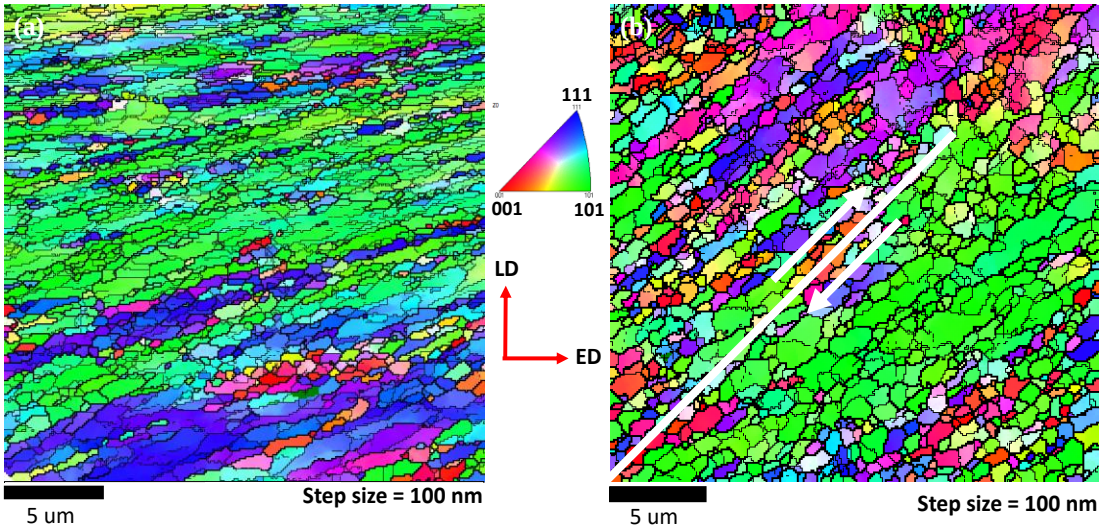

Figure 19 EBSD maps of the flow planes of (a) H-ECAP and (b) PA-ECAP, showing grain size refinement down to 308 nm ± 258 nm and 390 nm ± 330 nm, respectively. The white line and arrows shown in (b) indicates the theoretical shear plane for 90° ECAP channel.

The flow plane microstructure of ECAPed specimens (H-ECAP and PA-ECAP) was analyzed by electron microscopy. Figure 19 shows the EBSD maps for the two cases and it reveals an average grain size of 308 nm ± 258 nm and 390 nm ± 330 nm for H-ECAP and PA-ECAP, respectively. Both maps also show grain orientation approximately in the direction of shear plane, which is theoretically at 45°, as indicated by the white line in Figure 19b.

TEM micrographs of all four conditions are shown in Figure 20. The homogenized condition displays coarse grain structure, mostly precipitate free but shows some large primary precipitates as indicated by red circles on Figure 20a. Primary precipitates here are classified as those precipitates which remain undissolved during casting as well as homogenization and are typically carried on to the aged condition [78]. Quenched-in residual dislocation structure concentrated in the periphery of some grain boundaries can also be seen in the H condition. The grain structure after ECAP is much more refined with homogeneous distribution of coarse spherical precipitates (Figure 20b). After peak-aging we observe higher number density of precipitates, preferentially at heterogeneous nucleation sites, such as dislocations and grain boundaries. PA-ECAP (Figure 20d) shows similar grain refinement but relatively higher number density of precipitates as compared to H-ECAP. The size, number density, and different populations of precipitates in the four given conditions is discussed in more detail in the discussions section.

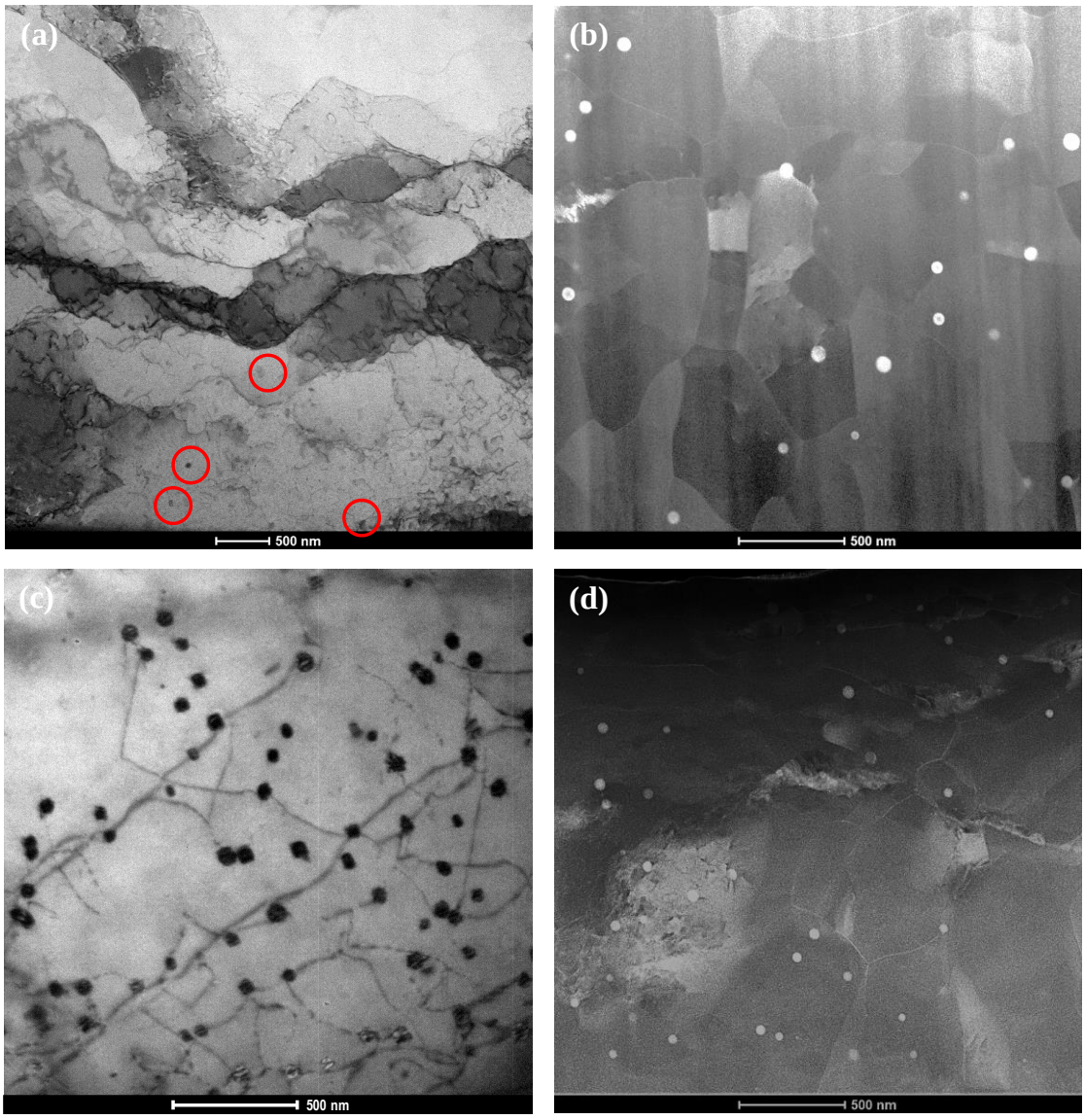

Figure 20 Bright field TEM images of (a) as-homogenized (H), (b) homogenized + ECAP (H-ECAP), (c) Peak-aged (PA) and (d) Peak-aged + ECAP (PA-ECAP). Red circles in (a) highlight the presence of primary precipitates after homogenization.

4.3.2 Mechanical characterization

Figure 21 compares the room temperature tensile behavior of the four different conditions. In homogenized condition H, the material shows lowest strength and maximum elongation. Any further processing (peak-aging and/or ECAP) results in higher yield and tensile strength, but at the expense of tensile ductility. In UFG Al alloys obtained by ECAP, the loss of ductility and work-hardening is often linked to the formation of shear bands due to strain localization [79].

The material in H-ECAP condition shows a 3-fold increase in yield strength in comparison to the homogenized condition. Similarly, the material in PA-ECAP condition shows 1.5 times increase in yield strength compared to the pre-ECAP peak-aged condition. Significant strengthening of about 3x in H-ECAP condition, compared to strengthening of about 1.5x in peak-aged condition, points towards possible higher degree of grain refinement or occurrence of dynamic precipitation during ECAP when starting from homogenized condition.

It is worth noticing that there is only a small 2% difference between yield strengths of H-ECAP and PA-ECAP conditions. Further experimental investigations discussed in this paper will investigate the reason behind the similar tensile response of PA-ECAP and H-ECAP conditions.

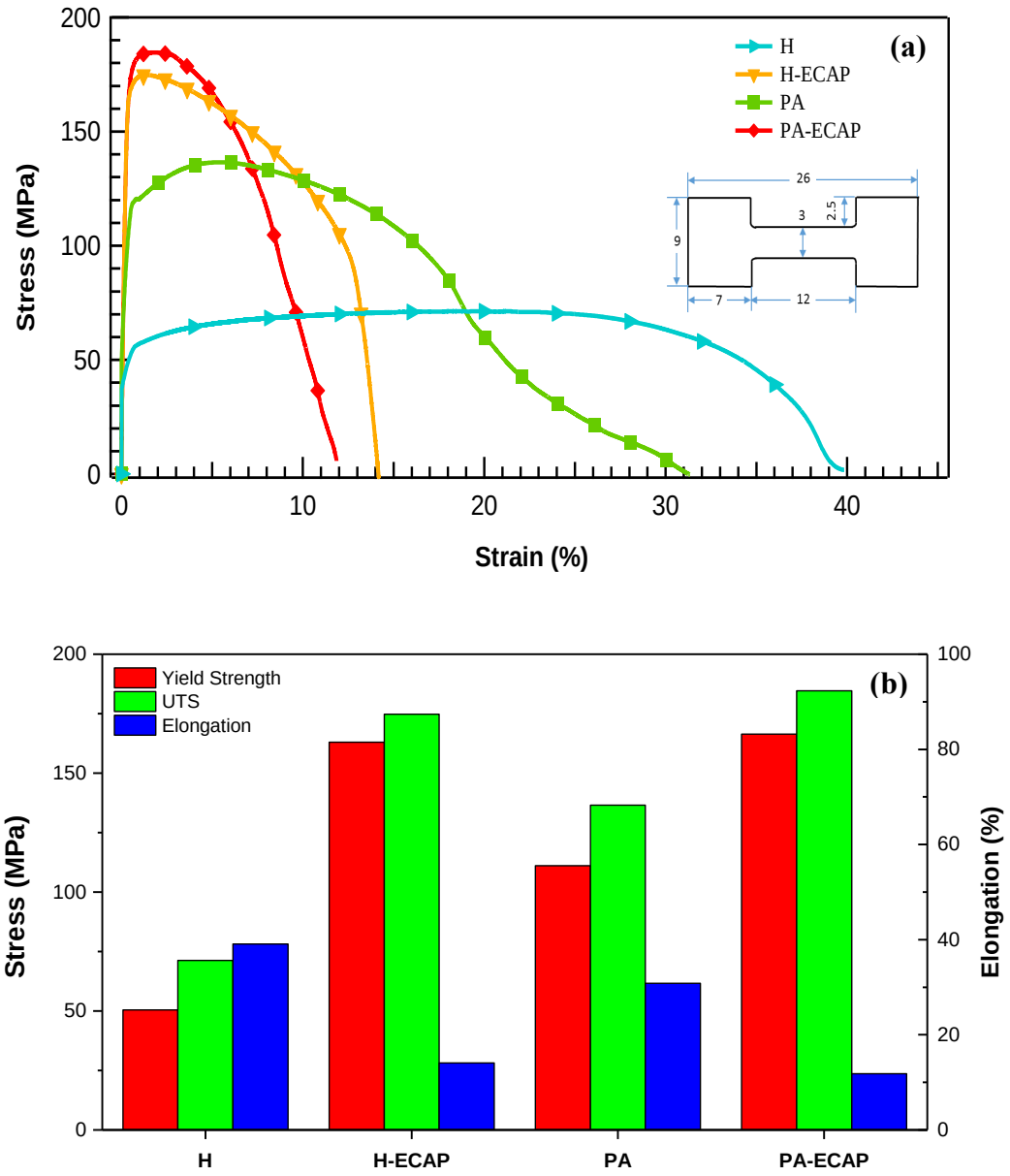

Figure 21 (a) Room temperature tensile properties of pre- and post- ECAP alloys in peak-aged and homogenized condition at nominal strain rate of 10^{-4} s^{-1}. The inset figure shows the dimensions, in millimeters, of a 1.5 mm thick flat dog-bone miniature tensile specimen used in this study. (b) Yield Strength, tensile strength and tensile elongation comparison for the four cases.

Figure 22 display the microhardness bar-chart of the four conditions. The trends observed here are consistent with tensile stress strain response. The increase in microhardness from homogenized condition to H-ECAP condition is ~2x, whereas the microhardness increase from PA to PA-ECAP is only ~1.2 times. In comparison to the tensile results, the increment factors of microhardness are not as pronounced. This may be because the cast alloys are often prone to porosity that may have influenced the tensile strength of H and PA conditions, whereas ECAP improved the quality of the cast by closing the pores due to the application of high pressure [80].

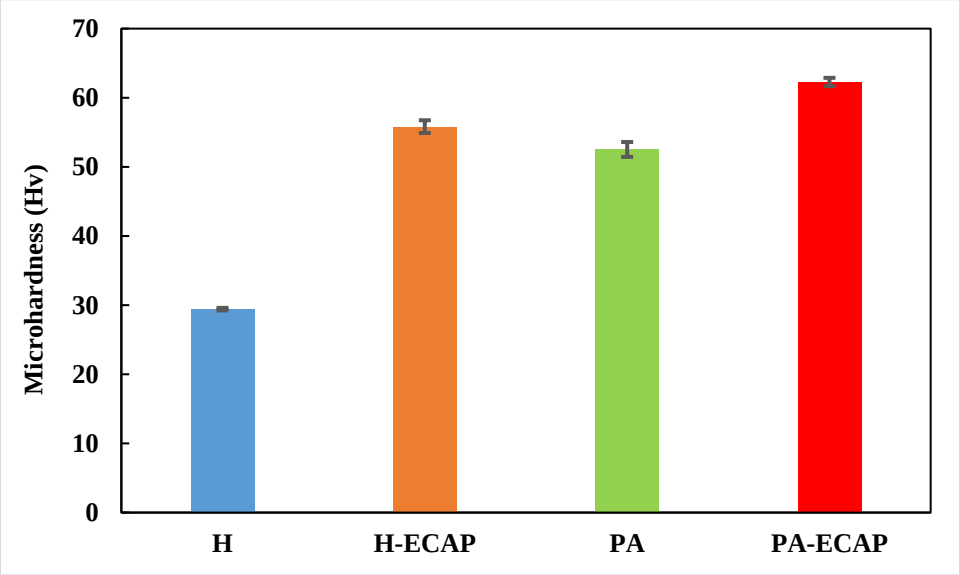

Figure 22 Comparison of Vickers microhardness for the four processed conditions of the alloy, showing increments in microhardness after ECAP.

4.3.3 Isochronal and isothermal aging

In order to understand the precipitation behavior before and after ECAP, evolution of microhardness with aging time and temperature was recorded after isochronal and isothermal heat treatments. Figure 23 shows microhardness evolution after isochronal heat treatment on H-ECAP samples using 50 °C / 3 h increments up to 575 °C. We have included the data for homogenized condition from our previous work for the benefit of the reader [13]. In summary, in homogenized condition precipitation starts around 200 °C and a small peak at 250 °C is linked to the Al_3Er precipitates [14]. Next peak at 350 °C corresponds to the Sc precipitation. Sharp increase beyond 350 °C is attributed to the precipitation of Zr and V. The specimen subsequently approaches peak-aged condition at 425 °C. At temperatures higher than 425 °C, precipitates coarsen and eventually dissolve in the solid solution, leading to a sharp decline in the microhardness [13].In contrast, isochronal aging curve for H-ECAP samples displays a slight increase in microhardness at 100 °C followed by a plateau until 250 °C. Continuous decrease after 300 °C is attributed to the combined effect of UFG, recrystallization and grain growth, and precipitate dissolution [44]. Absence of peaks in this condition at all aging temperatures, may be attributed to the interplay of recovery, precipitation, and associated grain growth [46]. A small increase in initial microhardness at 100 °C may be attributed to peak-aged condition.

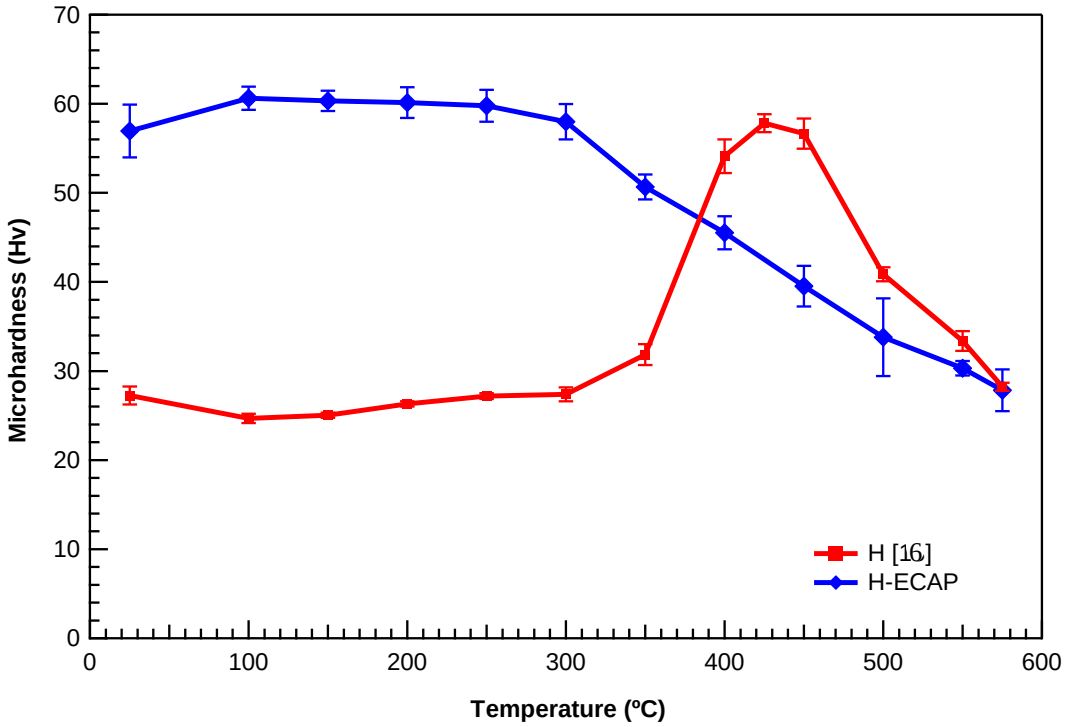

Figure 23 Microhardness variations with isochronal aging heat treatment of homogenized (H) condition before and after ECAP. The heat treatment was carried out in 50 °C increments, with a 3 h hold time at each temperature step. H curve, reprinted from Erdeniz et al. [16], shows a typical isochronal aging profile.

Figure 24 shows the isothermal aging treatments at 400 °C for up to 500 h, on homogenized and H-ECAP samples. In homogenized alloy, after an initial incubation period the onset of precipitation leads to increase in microhardness after 1 h and gradually increases until 16 h [16]. A small decrease in microhardness between 16 h and 24 h is attributed to the onset of coarsening of precipitates. The peak-aged condition which corresponds to peak microhardness is achieved after 24 h aging at 400 °C [16]. The isothermal aging curve of H-ECAP alloy, displays a trend similar to its isochronal aging response. Short times aging (5-15 min) shows slight increase in the microhardness which is consistent with accelerated aging kinetics expected after pre-deformation [81]. The

sudden drop in microhardness after 15 min (indicated by green line on Figure 24) aging is expected to be due to the onset of precipitate coarsening. Subsequent longer aging times result in combined effect of grain growth and precipitate dissolution, such that the alloy ultimately reaches the base microhardness of ~27 HV after 507 h of aging at 400 °C.

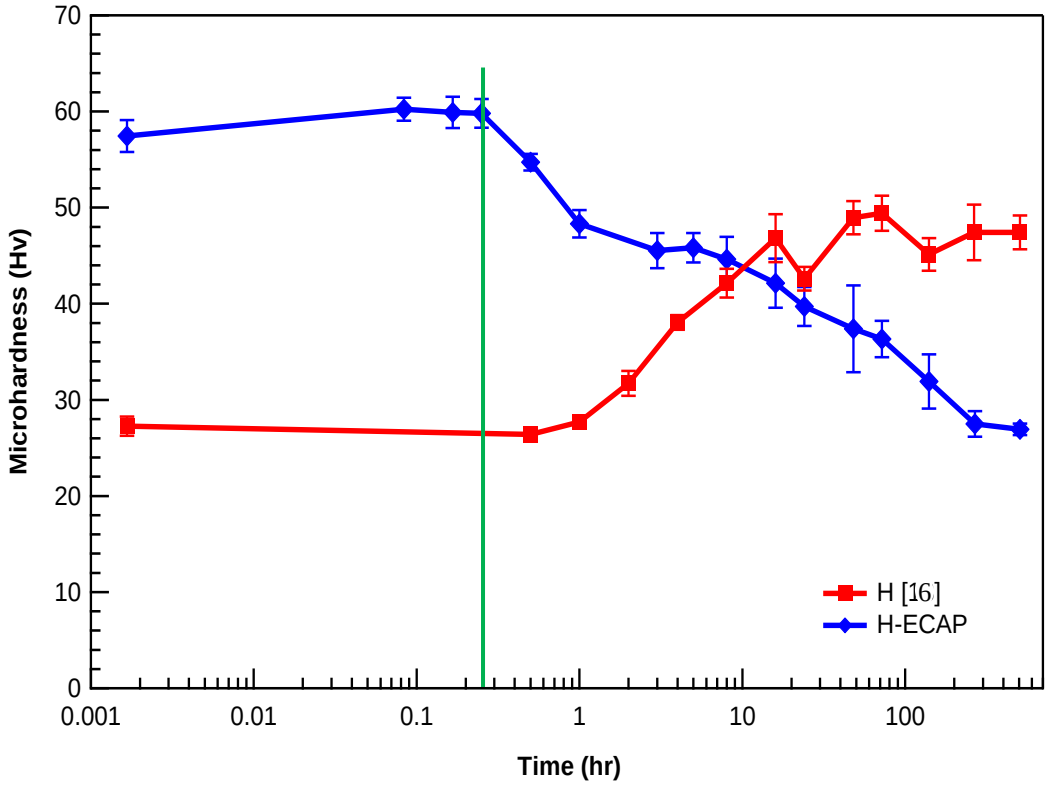

Figure 24 Microhardness variations with isothermal heat treatment of the homogenized (H) condition before and after ECAP, at 400°C for up to 507 h. The H curve, reprinted from Erdeniz et al. [16], is also included for comparison. H-ECAP displays only a slight increase in microhardness up to 15 min (indicated by vertical line), following a decrease in microhardness at longer aging times.

4.3.4 DSC and DIC

Calorimetry studies on homogenized and H-ECAP conditions were also conducted to better supplement the aging results and further validate the accelerated aging behavior. Figure 25 shows the differential scanning calorimetry result. In the homogenized condition, the first exothermic peak, followed by an endothermic peak are suspected to be related to GP zones formation and dissolution. Similar results have been observed for other Al systems and have been characterized as GP [82] and or GPB [83] zones. However, the authentication of GP zones in Al-Er-Sc-Zr-V-Si alloy system is beyond the scope of this paper and shall be investigated separately. In H-ECAP alloy only one precipitation peak at around 300 °C was observed, which could be attributed to Al_3Er. Other precipitation

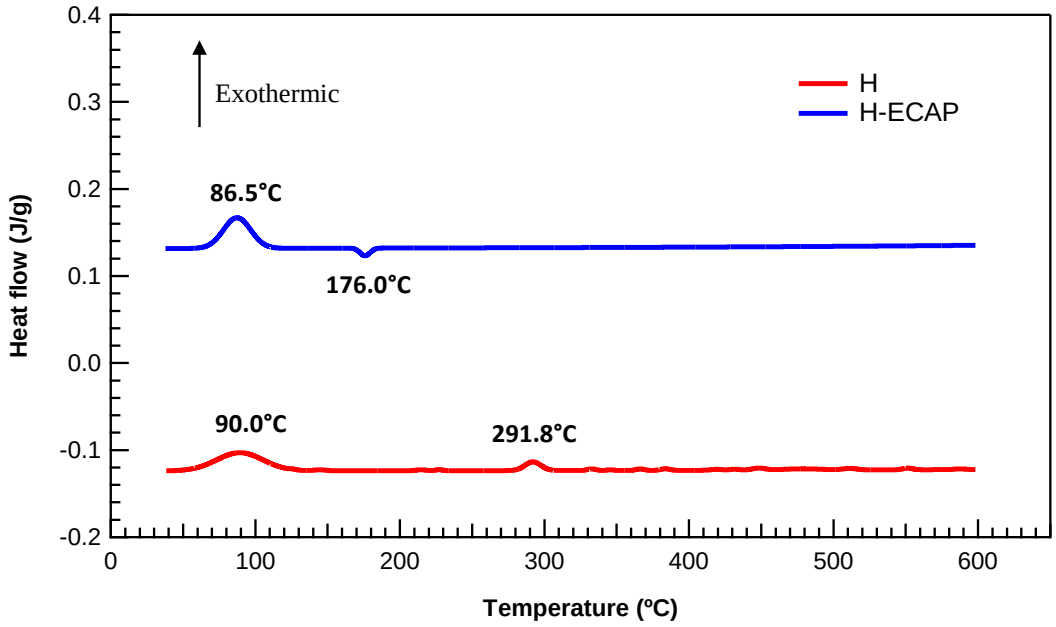

Figure 25 Differential scanning calorimetry of the alloy in H and H-ECAP conditions from 40 °C to 600 °C. The peaks below 200C represent GP zone formation, recovery and recrystallization events, while the exothermic peak at 292C is related to the precipitation of the fast diffusing Er.

peaks were not observed for this case. It was concluded that perhaps in the current DSC experiments the dwell time (at any temperature) was not sufficient to overcome the incubation period. Nevertheless, the higher intensity of the exotherm at 86.5 °C in H-ECAP curve points towards accelerated precipitation kinetics after ECAP.

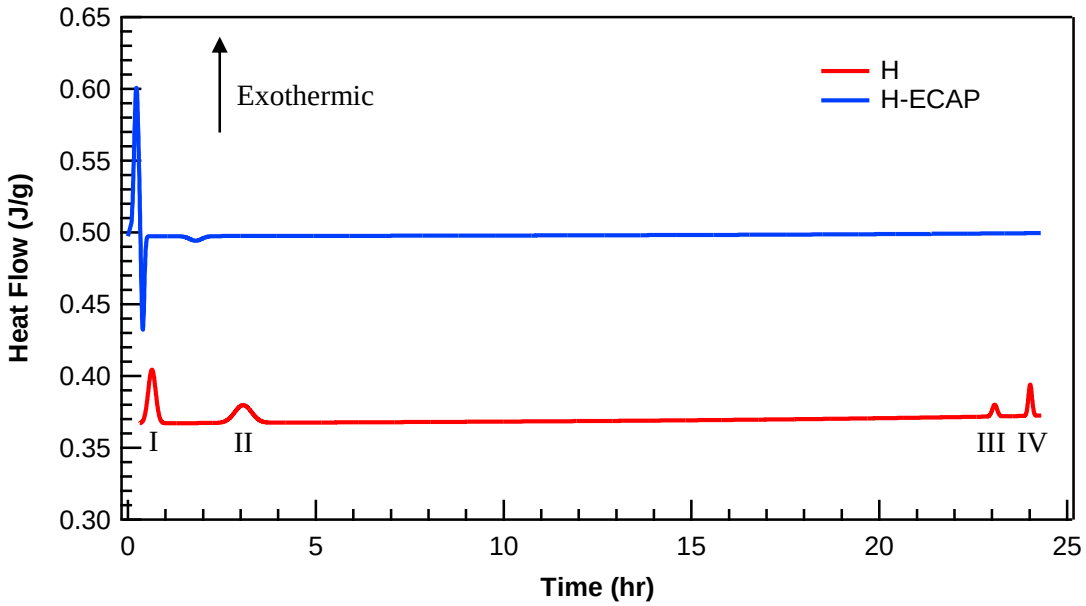

Figure 26 Differential isothermal calorimetry of H and H-ECAP conditions at 400 °C for 24 h. Four exothermic (I-IV) in H, at 0.64, 3.05, 23.06, and 23.99 h corresponds to Er, Sc, Zr, and V precipitation, respectively. Sharp exothermic peak followed by endothermic peak in H-ECAP, at 0.67 h, is possibly linked to formation of subsequent-shells by slower diffusing elements and recovery and recrystallization events. The small endothermic peak at 1.75 h is possibly linked to precipitation coarsening/dissolution.

DIC investigation was carried out to allow sufficient time for precipitation by holding at 400 °C temperature for 24 h. The contrasting trend in thermograms of H and H-ECAP conditions are presented in Figure 26. In homogenized alloy, four exothermic peaks (I-IV) were observed at 0.64, 3.05, 23.06, and 23.99 h, which corresponds to the

precipitation of Er, Sc Zr and V, respectively. This is due to sequential precipitation based on the intrinsic diffusivities of alloying additions and is consistent with our previous work and supported by other studies [14], [63], [84]. For H-ECAP condition, a high intensity exotherm quickly followed by an endotherm during the first 40 min of the scan indicates a combined effect of precipitation, recrystallization and grain growth.

4.4 Discussions

Alloying elements in Al-Sc-RE alloys have limited maximum solid solubility and therefore the supersaturated solid solution is unstable and susceptible to decomposition in response to small perturbations or chemical fluctuations [63], [85]. Furthermore, quenching from the high homogenization temperature of 640 °C, not only results in homogenous distribution of solute atoms but also creates potential vacancy sites which in-turn can facilitate the precipitation of tri-aluminide phases. The discussions in this paper are focused on the precipitation behavior during ECAP.

4.4.1 Grain refinement and precipitation during ECAP

TEM, Isothermal and Isochronal aging, DIC, and DSC were simultaneously employed to directly confirm the dynamic precipitation in supersaturated Al-Er-Sc-Zr-V-Si. The tensile strength and high microhardness of PA-ECAP alloy is due to combined strengthening effect of tri-aluminide precipitates from peak-aging heat treatment and grain refinement by ECAP. Consequently, the yield strength of PA-ECAP was expected to be much higher than H-ECAP, which was ECAPed without any prior aging. However, the tensile tests showed only 2 % difference in the yield strengths of the two cases. Possible reasons of similar tensile response of H-ECAP and PA-ECAP are: 1) higher degree of

grain refinement in H-ECAP, 2) possible partial dissolution, coarsening, and shearing of precipitates in PA-ECAP during ECAP, and 3) dynamic precipitation during ECAP in H-ECAP.

EBSD results in Figure 19 display uniform grain refinement, with almost identical grain size in the range of 300 – 400 nm, for H-ECAP and PA-ECAP. Nevertheless, the slight difference in grain size in both alloys may be correlated to the pre-ECAP grain size difference (H = 420.7 ± 183.0 µm and PA = 709.4 ± 464.7 µm).

Table 6 Precipitate number density and mean precipitate radius evaluated from TEM images for the four different processed conditions of the alloy.

Designation	Precipitate number density (coarse) (m^{-3})	Mean precipitate radius (coarse) (nm)	Precipitate number density (fine) (m^{-3})	Mean precipitate radius (fine) (nm)
H	1.67×10^{18}	37.1 ± 8.4	NA	NA
H-ECAP	3.29×10^{19}	33.2 ± 3.5	1.54×10^{22}	2.1 ± 0.5
PA	1.50×10^{20}	26.5 ± 5.9	1.77×10^{22}	1.7 ± 1.0
PA-ECAP	5.67×10^{19}	23.3 ± 4.5	1.25×10^{22}	3.9 ± 1.2

The size and number density of coarse precipitates in all four conditions, as shown in Figure 20, are given in Table 6. Primary precipitates in H have a relatively low number density of 1.67×10^{18} m^{-3} and larger radius of ~37 nm. These precipitates are most likely intergranular Al_3Zr, that forms during solidification and homogenization, and have been characterized in our previous study [16].

The number density of coarse precipitates increases after aging heat treatments and ECAP. The pre-ECAP precipitate evolution after several aging heat treatments has been discussed in detail by Erdeniz et al. [16]. Discussion in this section is mainly focused on the number density, sizes, distribution, and evolution of tri-aluminide precipitates after ECAP of H and PA conditions. High resolution TEM reveals extremely fine nanosized precipitates inside the grains of PA-ECAP and H-ECAP specimens.

High resolution TEM images of PA-ECAP are displayed in Figure 27. Quite a few coarse precipitates can be seen in Figure 27a and high magnification of one such precipitate of radius 13 nm, shows coherency of these precipitates with the aluminum matrix in Figure 27b. Also, it can be seen that these precipitates preserve their spherical morphology and do no fracture or shear after ECAP. Fragmentation and shearing of precipitates in aluminum based alloys, during ECAP has been observed in previous studies [46], [48], [74]. However, these precipitates are relatively larger in size and have plate-like and needle-like morphologies. For this alloy, no precipitate shearing was observed in the TEM analysis for PA-ECAP (Figure 20d).

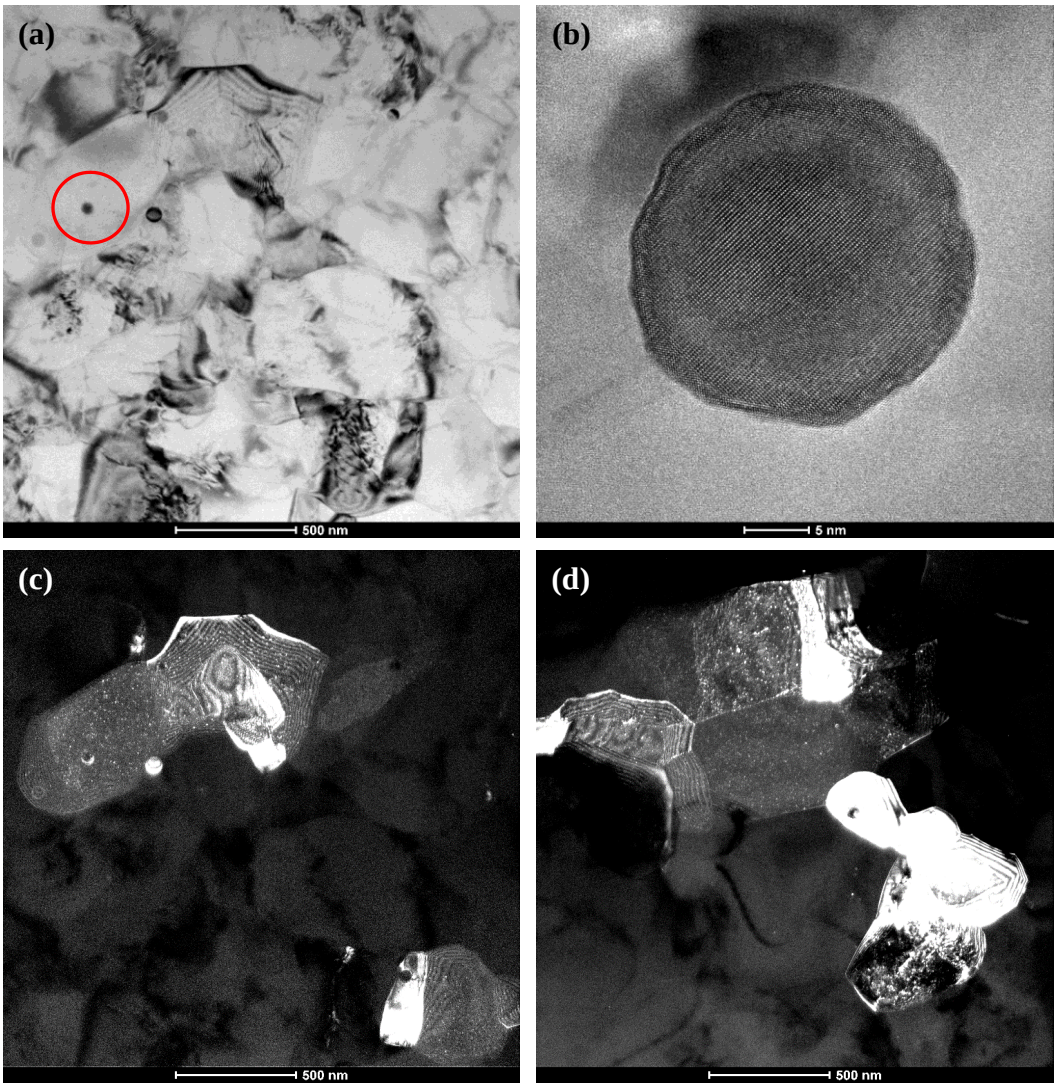

Figure 27 Bright field TEM from the flow plane of PA-ECAP showing (a) overall structure with grains elongated along the direction of ECAP shear plane, some coarse precipitates and high dislocation density after ECAP, (b) High magnification image of a 13 nm radius spherical $L1_2$ precipitate encircled in (a), shows no evidence of precipitate fracturing after ECAP. Dark field TEM showing (c-d) high density of fine precipitates distributed inside the grains, some coarse precipitates can also be seen along the grain boundaries.

Dark field TEM, shown in Figure 27c-d, reveals very fine precipitates with a number density of 1.25491 x 10^{22} m^{-3} and radius of 3.9 ± 1.2 nm, distributed inside the grains. These nanosized tri-aluminides play an important role in strengthening and creep resistance by impeding the motion of dislocations. Relatively larger precipitates ~13 nm radius, can be seen pinning the grain boundaries in Figure 27d. The precipitate size and distribution of PA-ECAP condition is approximately similar as compared to PA and H-ECAP, proving that no dissolution and coarsening took place in precipitation hardened alloy during ECAP. It was also highly unlikely because the solid solubility of the alloying elements is very limited at room temperature, even with the accelerated-precipitation kinetics after ECAP, the dissolution and precipitate coarsening is improbable. Moreover, high particle/matrix interfacial energy is necessary to initiate coarsening [86]. It is also reported that the onset of coarsening in V-containing Al-Sc alloys is at temperatures >400 °C [16].

Figure 28a present the TEM micrographs of H-ECAP displaying refined grain structure with high angle grain boundaries. The coarse precipitate (~33 nm radius) can be seen pinning at the triple junction in Figure 28a, is further magnified in Figure 28b. Unlike the precipitate observed in PA-ECAP (Figure 28b), this precipitate doesn't reveal contrast difference and is therefore, most likely a primary Al_3Zr precipitate. Presence of finely distributed, nanosized tri-aluminide precipitates of 2.1± 0.5 nm radius, shown in Figure 28c-d, confirms the dynamic precipitation hypothesis during room temperature ECAP of a supersaturated Al-Er-Sc-Zr-V-Si. The number density of 1.55 x 10^{22} m^{-3}, is on the same order as observed in PA and PA-ECAP. Similar type of formation of nanosized

precipitates inside the grains was also observed in Al 6061 after 4 ECAP passes at 100 °C [87]. That phenomenon, however, was termed as dynamic aging since the ECAP was performed at elevated temperature.

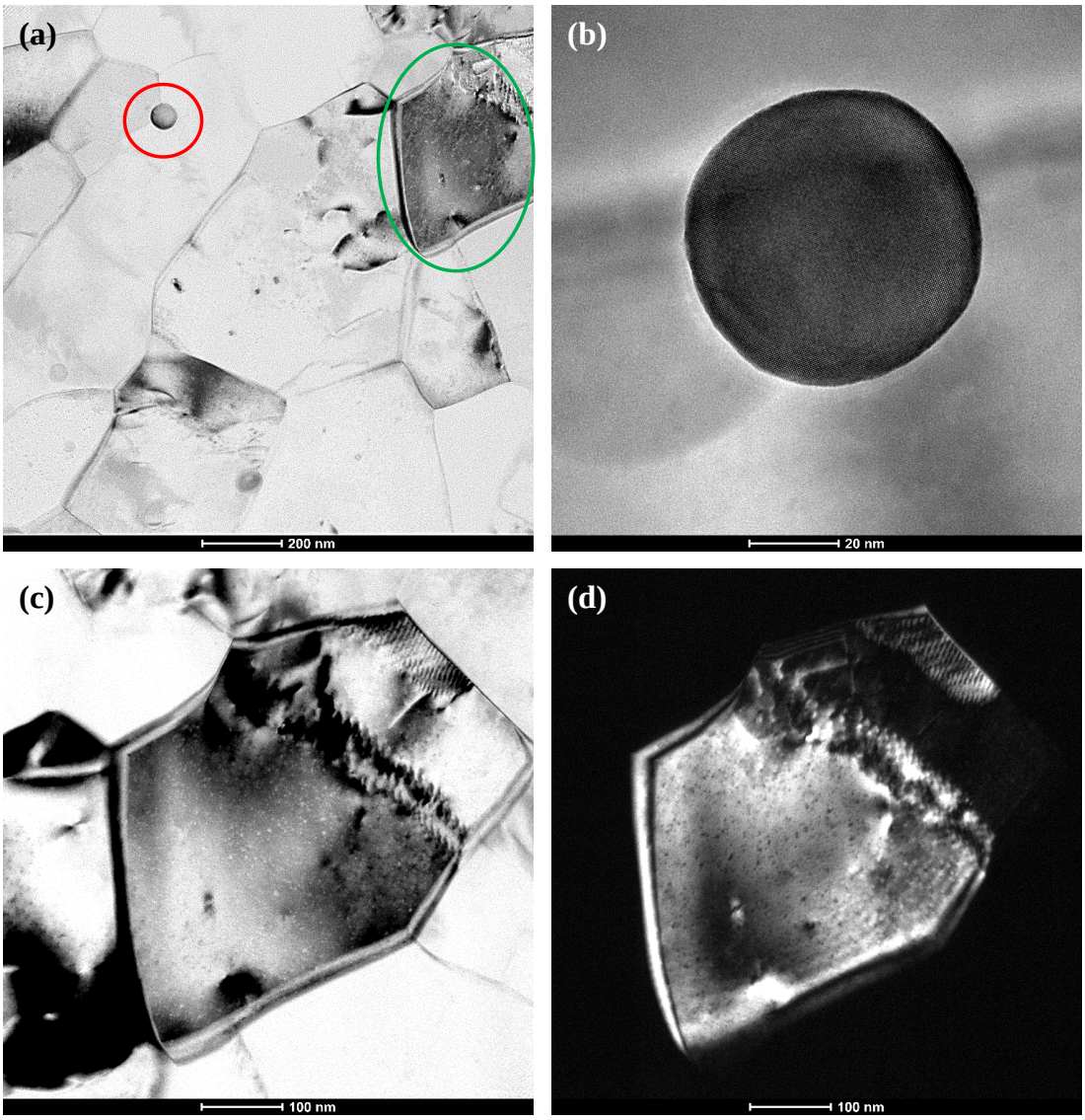

Figure 28 Bright field TEM from the flow plane of H-ECAP showing (a) ultra-fine grain structure with high angle grain boundaries, (b) high magnification image of a ~33 nm radius primary precipitate. (c) Bright field and (d) dark field TEM image showing extremely fine, nanosized trialuminides in grain interior as result of dynamic precipitation during room temperature ECAP.

The decomposition of supersaturated solution during ambient temperature ECAP is due to the deformation-accelerated diffusion instead of thermally-activated diffusion. Diffusion-controlled transformations during conventional work-hardening methods can be directly correlated to the process temperature. For instance, diffusion is negligible and often neglected during a cold work process, however, diffusion fluxes at elevated temperatures, during a hot working process, result in recovery and dynamic recrystallization processes in conjunction with deformation [88], [89]. Accelerated solid-state diffusion under the application of intensive periodic plastic deformation such as mechanical alloying, has also been known for quite long [90]–[92]. However, this phenomenon during room temperature SPD is relatively new and has gained some interest recently [88], [93]–[96]. Unlike cold-working, severe straining during room-temperature ECAP results in the production of vacancy and interstitial sites, which can induce diffusion controlled processes during [74] or after ECAP [93]. The formation of $L1_2$ ordered precipitates in Al-Mg alloy has recently been observed during elevated temperature (>300 °C) ECAP by Buanova et al. [94]. The main driving force in the decomposition of Al-Er-Sc-Zr-V-Si alloy is the supersaturation. During SPD of a supersaturated alloy, there is a competition between non-equilibrium and equilibrium states [88]. Severe straining results in grain refinement which shifts the structure away from equilibrium. The excess stored energy in the system is utilized in decomposition of the kinetically suppressed phases and tend to restore the equilibrium. It has been discovered that four passes of ECAP route Bc

induces enough strain energy to initiate deformation-accelerated precipitation in Al-Er-Sc-Zr-V-Si.

4.4.2 Dynamic precipitation vs. static precipitation

Dynamic precipitation refers to nucleation of precipitates as a by-product of a primary plastic deformation process. Whereas, static or conventional aging occurs at elevated temperature and excludes any deformation. Aging heat treatments and calorimetry analysis were employed to understand the precipitate evolution during isothermal and isochronal heating before and after ECAP. Peak-aged condition in H-ECAP is subsequently obtained after 3 h aging at low temperature of 100 °C (Figure 23) and 5-10 min aging at 400 °C (Figure 24). A small increase in microhardness of H-ECAP during aging heat treatments indicate that the dynamic precipitation during ECAP was partial. H-ECAP showed thermal stability for up to 3 h at 300 °C and 1 h at 400 °C. A uniform distribution of precipitates was observed in H-ECAP and PA in general, nevertheless a large number $Al_3(X)$ precipitates also nucleate at the grain boundaries and dislocations (Figure 27d and Figure 28a). These precipitates inhibit grain coarsening during isothermal and isochronal aging of ECAPed H-ECAP. Hence, during the initial aging time and temperature, there is a synergism between precipitation and resistance to grain growth. This is possibly beneficial for initial high temperature stability but its effect on creep performance still needs to be investigated.

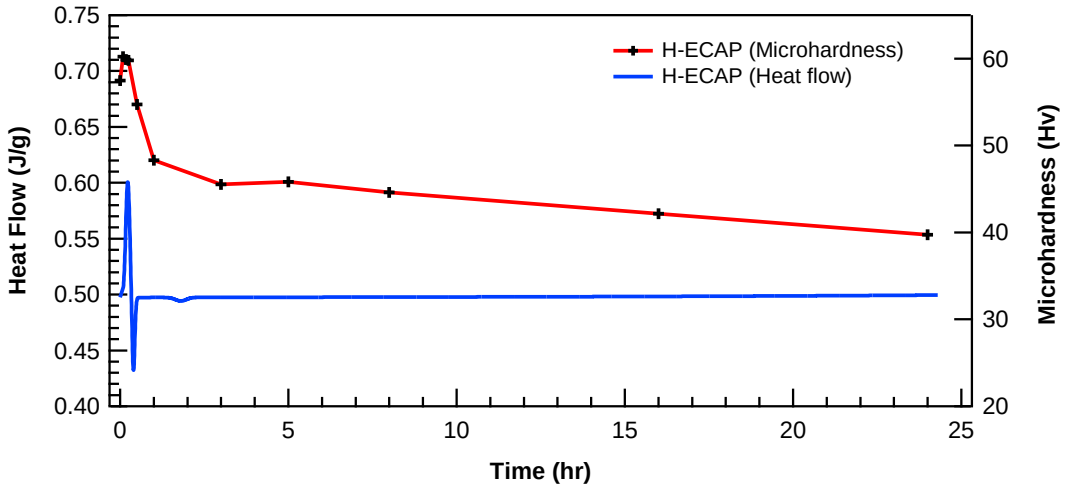

Figure 29 Overlay of differential isothermal calorimetry and microhardness evolution of homogenized alloy after ECAP. Combined effect of precipitation, recovery and recrystallization, conforms to the small increase and subsequent drop in microhardness.

Figure 29 shows the overlay of 400 °C isothermal aging and DIC thermogram of H-ECAP. The microhardness trend in post-ECAP alloys during isothermal aging is in good agreement with its DIC result. A large exothermic peak during the first 15 min followed by an endothermic peak may be correlated to the combined effect of precipitation, recrystallization and grain growth, and onset of precipitate coarsening. Heat is released during the vacancy and dislocation annihilation, giving an exothermic peak in DIC [97]. Starink [77] explains that the heat released during recrystallization is much smaller than it is for precipitation and can overlap the precipitation temperature regime. In this particular case, high heat flow during exothermic peak is expected to be due to the combined effect of microstructure restoration and precipitation. This also explains the small increase in microhardness during the first 15 min of aging. Subsequent sharp

decrease in microhardness during the first 3 h of isothermal aging can be attributed to grain growth and precipitate coarsening, which is also shown by the two endotherms. At times >3 h, the microhardness decreases gradually until reaching the base alloy microhardness after 507 h. Despite high homologous temperature, grain structure resists coarsening during isothermal aging because of precipitates pinning at the grain boundaries. Similar observation was made by H. Hallem et al [98] for Al containing Hf, Sc, and Zr, which showed recrystallization resistance due to the formation of tri-aluminide precipitates.

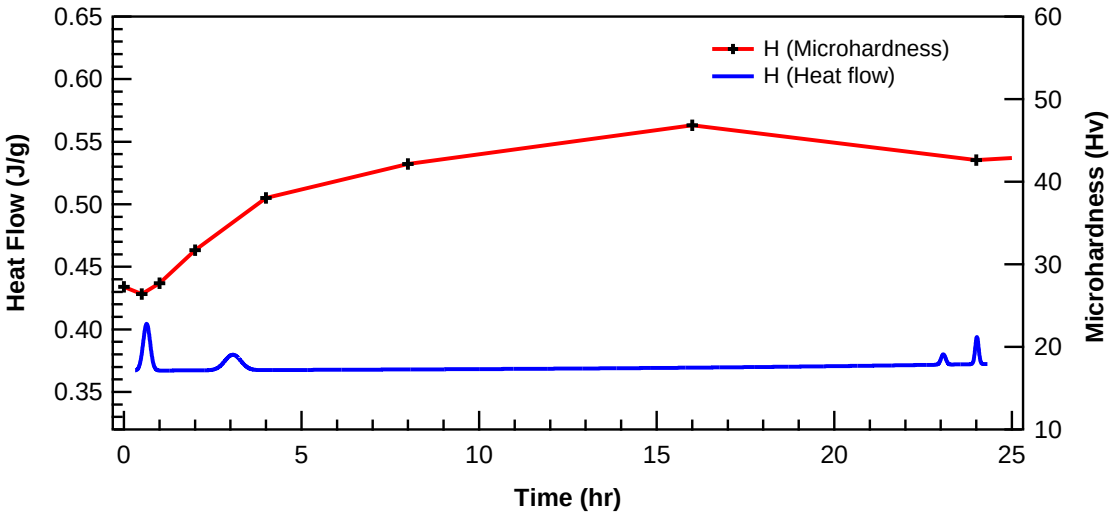

Figure 30 Overlay of differential isothermal calorimetry and microhardness evolution of homogenized alloy before ECAP. The evolution of microhardness is in agreement with the onset of precipitation peaks in from DIC thermogram.

Figure 30 shows the overlay of 400 °C isothermal aging and DIC thermogram of H. The DIC peaks represent the precipitation sequence during aging of homogenized Al-Er-Sc-Zr-V-Si. Knipling et al. [63] reviewed the measured activation energies of several transition elements in aluminum. Among all the given alloying elements, Er has the lowest

activation energy for diffusion in Al [99], and is expected to precipitate first. Hence, the first DIC peak is attributed to the nucleation of Al_3Er. The core-shell precipitation configuration [16] start to take form with the onset of precipitation of Sc, Zr, and V shells at 3, 23, and 24 h, respectively. The continuous increase in microhardness can be directly correlated to the precipitation peaks observed in DIC.

4.5 Conclusions

The effect of ECAP on the precipitate evolution and mechanical behavior of an Al–0.02Sc-0.005Er–0.07Zr–0.08V–0.06Si at. % alloy was studied. The following conclusion can be drawn from this work:

1) Similar grain refinement, down to 308 nm ± 258 nm for homogenized condition and 390 nm ± 330 nm for peak-aged condition, was attained after ambient temperature ECAP using route 4Bc. The improvement in strength at the expense of ductility after ECAP was as expected. Only a small difference of ~2 % in yield strengths between homogenized and peak-aged conditions after ECAP was noted.

2) TEM analysis showed two different populations of precipitates, referred to as coarse (~30 nm radius) and fine (~2.5 nm radius), in ECAPed conditions. Formation of nanosized tri-aluminides inside the grains of homogenized condition after ECAP confirmed dynamic precipitation. The decomposition of supersaturated solid solution during ambient temperature ECAP is due to the deformation-accelerated diffusion instead of thermally-activated diffusion. Precipitates in peak-aged alloy maintain their spherical shape after ECAP.

3) Differential isothermal calorimetry at 400 °C revealed: i) several peaks corresponding to the sequential precipitation of Er, Sc, Zr, and V in homogenized condition and ii) an exothermic followed by an endothermic peak corresponding to recrystallization, grain growth and precipitate coarsening in homogenized condition after ECAP. Consequently, a good agreement between the DIC thermograms and microhardness plots after isothermal aging heat treatments was observed.

4) Peak-microhardness state after 3 h aging at low temperature of 100 °C or 15 min aging at 400 °C was achieved for homogenized condition after ECAP. Furthermore, the alloy showed a thermal stability for up to 3 h at 300 °C and 1 h at 400 °C. This was attributed to the synergism between precipitation and resistance to grain growth during aging. TEM showed pinning of precipitates at the grain boundaries, which inhibits grain growth.

CHAPTER V

STRESS-INDUCED GRAIN GROWTH AND HIGH-TEMPERATURE MECHANICAL PROPERTIES OF ULTRA-FINE-GRAINED AL-ER-SC-ZR-V-SI ALLOY

5.1 Introduction

Aluminum alloys are notable for their low density and can be tailored to exhibit combination of adequate strength and ductility through precipitation hardening and severe plastic deformation (SPD) processes. Aforementioned attributes make these alloys potential candidates for applications in aerospace, automotive, and power transmission industries [1], [3], [67].

Aluminum alloys, used in applications such as internal combustion engines, brake rotors, and high temperature wires, can be exposed to high temperatures with or without externally applied loads. It is important to understand the microstructural and mechanical changes that occur in these alloys under such conditions. Static grain growth (SGG) mechanisms and kinetics of nanostructured and ultra-fine-grained (UFG) aluminum alloys subjected to elevated temperatures (isothermal or isochronal annealing), have been reported in various theoretical and experimental studies [100]–[105].

The interface or the grain boundary network has a certain free energy per unit area of the boundary that serves as a driving force for grain growth during isothermal annealing [106]. Another important and relatively less explored phenomenon is dynamic grain growth (DGG), also known as stress-induced grain growth and it primarily depends on the

nature of applied stress, strain rate, strain, and temperature [107]–[115]. DGG is more pronounced in refined grain structures and can occur under various scenarios including tension [116], compression, creep [117], nanoindentation [118], and even SPD [119], [120]. Liao et al. studied deformation-induced grain growth in nanocrystalline Ni in high pressure torsion and reported that there is a certain critical stress/deformation mode that can induce grain growth, i.e. if the growth is primarily driven by stress and not diffusion.

However, there is an upper cap to this form of grain growth, and the net result is the balance between grain refinement and grain growth [120]. Since DGG may occur under several stress modes and adversely affect the mechanical properties, it has important implications in manufacturing processes (hot rolling, forging, extrusion) and in-service applications (components that undergo uniaxial/multiaxial stresses during operation) [121]. DGG mechanisms include grain sliding, rotation, and grain boundary migration, which can also account for plasticity during deformation [109], [115], [122]. Stress assisted grain growth in an ECAPed commercially pure Al at elevated temperature using in-situ TEM was reported by Mompiou et al. [109]. They found coupling between shear and migration mechanisms during stress-assisted grain growth.

Stress assisted grain growth in dispersion and precipitation strengthened aluminum alloys is also controlled by the size, volume fraction, and interaction of precipitates with the grain boundaries. In this context, Lin et al. [123] studied stress-induced grain growth in spark plasma sintered nanostructured Al containing Al_2O_3 and found that grain growth was inhibited during annealing in the absence of stress but significant growth occurred during hot extrusion. It is known that the presence of second phase particles or precipitates

can influence the recrystallization and grain growth kinetics. Al-Sc alloys subjected to ECAP can yield UFG structure that can be stabilized by Zener pining by trialuminide precipitates [66], [124]. The question here is the effectiveness of these precipitates in resisting the grain growth during high temperature uniaxial deformation when both diffusion and stress-induced growth factors are at play, along with the dominant mechanisms of elevated temperature DGG in precipitation-hardenable Al alloys.

The model alloy selected to study this phenomenon is a recently developed high temperature Al-Er-Sc-Zr-V-Si alloy. After a double-aging heat treatment of 350 °C/12 h and 400 °C/16 h from a homogenized condition, nanostructured trialuminide Al_3X (X represents rare-earth and transition metal micro-additions) precipitates form which are hard, coherent, and thermally stable [16]. Erdeniz et al. [16] characterized core-shell structure of the precipitates, exhibiting superior coarsening resistance in Al-Er-Sc-Zr-V-Si system. A large volume fraction of these precipitates preferentially grow at the grain boundaries and exert a Zener pinning effect resulting in the impedance of grain growth during isothermal annealing [66][125].

The role of trialuminide precipitates on the static and dynamic grain growth and their corresponding high temperature mechanical properties in ECAPed Al-Sc-X alloys has not been reported previously. Therefore, the aim of this research is to investigate the role of trialuminide precipitates in restraining the grain growth during static and dynamic isochronal annealing and their subsequent effect on elevated temperature tensile properties. Hence, to develop a better understanding, we report here: 1) the mechanical properties of Al-Er-Sc-Zr-V-Si at elevated temperatures, before and after ECAP, and 2)

the kinetics of static grain growth (annealing without any load) and its comparison with dynamic grain growth (under uniaxial tensile deformation at elevated temperature). Mechanisms related to contrasting trend of mechanical properties (yield strength and ductility) at room temperature and elevated temperature are discussed.

5.2 Experimental Procedure

5.2.1 Alloy production and microstructure modification

An aluminum alloy with micro additions of Sc, Er, V, Zr, and Si was selected for this study. The nominal at. % composition of the alloy is given in Table 7. The alloy production, optimization and selection of the aging parameters and corresponding precipitation sequence has been reported in our previous work [16]. The as-cast alloy was peak-aged by employing a special heat treatment. As described by Erdeniz et al., [16] the as-cast billets were first homogenized (H) at 640 °C for 4 hr and quenched in water. Later, they were subjected to a double-aging heat treatment of 350 °C/12 hr and 400 °C/16 hr to achieve a peak-aged (PA) condition comprising of finely distributed nanosized trialuminide Al_3(Er, Sc, Zr, V) core-shell precipitates in Al matrix. The average grain sizes in homogenized only (H) and peak-aged (PA) conditions were measured to be 411 ± 232 μm and 656 ± 385 μm, respectively. Optical micrographs of initial microstructures are shown in Figure 31. Grain refinement in H and PA alloys was achieved through Equal Channel Angular Pressing (ECAP) at room temperature using route 4Bc, and in the text these conditions for convenience will be referred to as H-ECAP and PA-ECAP. ECAP had an internal angle of 90° between the die channels. ECAP route Bc with 4-8 number of passes have been reported to produce uniform ultra-fine grained structure exhibiting

high degree of misorientation and high angle grain boundaries in various alloys including aluminum [29], [59], [60].

Table 7 Composition in at. %, of alloying additions in aluminum.

Sc	Er	Zr	V	Si	Al
0.013	0.007	0.071	0.074	0.054	Bal.

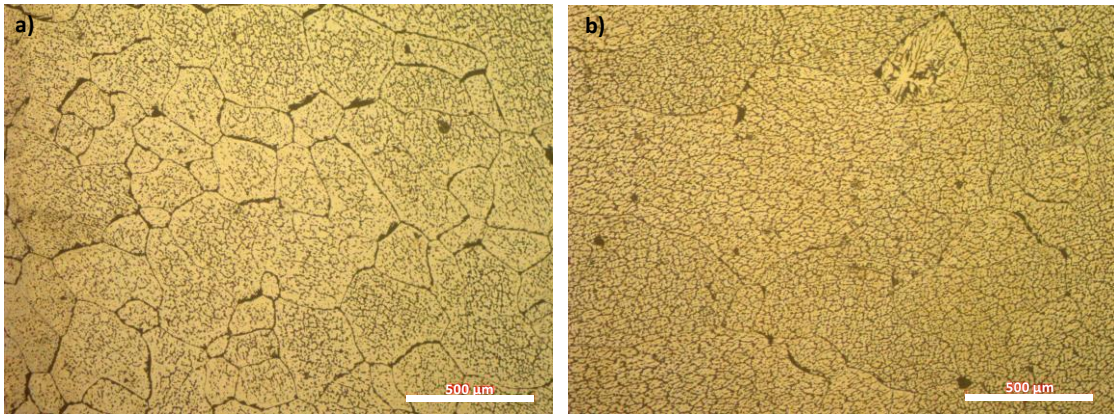

Figure 31 As-received optical microscopy images of Al-Er-Sc-Zr-V alloys in a) Homogenized (H) condition with average grain size of 411 ± 232 µm and b) Peak-aged (PA) condition with average grain size of 656 ± 385 µm.

5.2.2 High temperature tensile deformation

This specific Al-Er-Sc-Zr-V-Si alloy was developed for high temperature applications and its creep behavior has been reported by Erdeniz et al. [16]. The tensile properties of this alloy after ECAP at high temperatures of up to 400 °C (~ homologous temperature = 0.72) are reported here. Uniaxial tensile tests were carried out on flat dog-bone, miniature specimens of 26 mm overall length (11 mm gauge length). The tensile

specimens were electro-discharge machined from the middle section of PA billet and flow planes, and, along extrusion direction for H-ECAP and PA-ECAP billets. Tests were performed using an MTS Insight machine equipped with a 1 kN load cell and a split tube single zone furnace. The temperature of the specimens was maintained within ± 2 °C of the intended temperature, measured with a thermocouple placed on the surface of the specimen. All the tensile tests were conducted at an initial strain rate of 10^{-4} s^{-1} and strain was measured using a high temperature Epsilon Model 3549, 0.5 in. gauge length contact extensometer with measuring range of +100/-5%.

In addition, decremental step strain-rate tensile tests were conducted at 200, 300, and 400 °C to evaluate strain rate sensitivity (SRS) of UFG H-ECAP and PA-ECAP conditions. At each temperature the initial strain rate of 10^{-2} s^{-1} was used for up to 10 % strain to overcome work hardening and achieve steady stress. Thereafter, one order of magnitude strain rate step decrement was applied until 10^{-5} s^{-1}.

Incremental and decremental strain-rate sensitivity are two most commonly used methods, and their comparison was made by Hedworth and Stowell [126]. Incremental strain rate, in particular, is susceptible to structural changes such as dynamic grain growth and defect structure. In this study decremental strain-rate sensitivity method was applied because decremental step strain-rate tests are more efficient in reaching steady-state stress and maintaining isostructural condition [127]. SRS tests were conducted at 200, 300, and 400 °C.

5.2.3 Annealing heat treatments and microstructure characterization

First, PA, H-ECAP, and PA-ECAP conditions were subjected to isochronal annealing heat treatments to compare their thermal stability which is gauged by their ability to maintain microhardness after being subjected to annealing at various temperatures. The isochronal annealing was conducted in the temperature range of 50 to 575 °C with 50 °C increments and a hold time of 3 h at each temperature step. Vickers microhardness was periodically measured after each heat treatment step. At least 10 indentations were recorded per specimen by employing a 50 gf load and a dwell time of 15 s. Prior to Vickers microhardness testing, the heat-treated specimens were ground and polished to 1μm finish using diamond paste.

Second, to understand grain growth in the H-ECAP and PA-ECAP materials, annealing heat treatments at 400 °C were carried out under static and dynamic conditions. All specimens were electro-discharge machined from flow planes and along extrusion direction. In dynamic annealing, specimens were subjected to interrupted uniaxial tensile tests at 400 °C. The tensile tests were carried out at an initial strain rate of 10^{-4} s^{-1} and interrupted after the specimens were deformed to plastic strains of 10 % and 30 %. In order to allow for direct comparisons, static annealing experiments for times similar to tensile tests were carried out on specimens with similar dimensions, inside the same furnace setup. All heat treatments were terminated with water quenching.

Electron backscatter diffraction (EBSD) was employed to evaluate grain size and misorientation angle distributions, and sub-grains after static and dynamic annealing heat treatments. For the dynamic case, EBSD specimens were electro-discharge machined from

uniformly deformed gauge sections of the tensile specimens with 10% and 30% strain. EBSD specimens were ground to 1200 grit size in several steps, then polished using 1 μm, 0.25 μm diamond paste and final polishing using 0.05 μm colloidal silica. For the isochronal aged specimens EBSD maps were measured using the Tescan FERA-3 Model GMH under an accelerating voltage of 20 kV with varying step sizes from 0.1 microns to 1.5 microns due to varying grain sizes. For the dynamic annealing study, a Philips XL30 FEG SEM with an accelerating voltage of 20 kV and spot size 5 (about 5 nA current) was used to perform EBSD. The step size was 0.2 microns. EBSD data was collected and analyzed using Oxford Instruments Aztec, Channel-5, EDAX TEAM and OIM Analysis softwares. In all EBSD images grain tolerance angle of >1° or >5° was used, as specified in the figure captions.

FEI Techna Transmission electron microscope (TEM), operating at 120 KeV was employed to observe nano-precipitation behavior in H-ECAP and PA-ECAP conditions of Al-Er-Sc-Zr-V-Si. TEM samples were prepared by starting from ~1.5 mm thin slices cut from the representative billets. The slices were subsequently ground by mechanical means to less than 100 μm thickness. 3 mm diameter discs were punched from the twin-jet electro-polished specimens in 30 vol. % HNO_3 + 70 vol. % CH_3OH electrolyte at -10 °C, utilizing a 10 V_{dc} potential.

5.3 Results

The aspects of grain refinement and precipitate microstructure in H and PA materials after ECAP and their corresponding room temperature mechanical properties are discussed in a related publication [128].

Some key ambient temperature mechanical properties are summarized in Table 8 for the benefit of the reader. One key conclusion was that the small difference in yield strengths of H-ECAP and PA-ECAP alloys at ambient temperature were mainly due to differences in precipitation behaviors during ECAP (Chapter 4).

Table 8 Grain size and room temperature mechanical properties of Al–Sc–Er–Zr–V–Si alloy in Homogenized (H), Peak-aged (PA), Homogenized + ECAP (H-ECAP), and Peak-aged + ECAP (PA-ECAP) conditions.

Sample/ Properties	Grain size (μm)	Yield Strength (MPa)	Ultimate tensile strength (MPa)	Microhardness (HV)
H	420.7 ± 183.0	50.7	71.3	29.42 ± 0.19
PA	709.4 ± 464.7	111.1	136.5	52.52 ± 1.07
H-ECAP	0.308 ± 0.258	163.2	174.8	55.82 ± 0.92
PA-ECAP	0.390 ± 0.330	166.4	184.6	62.28 ± 0.60

5.3.1 Microhardness variations with temperature

At elevated temperatures, the ability of ECAP processed aluminum alloys to maintain their microhardness is important from potential applications stand-point. Therefore, a detailed isochronal heat treatments study and periodically measured microhardness was carried out. Figure 32 shows the variation of microhardness after static annealing heat treatment for 3 hr at each temperature and dotted lines represent the mean

stability range and corresponding microhardness for each case. The variation in microhardness of peak-aged alloy prior to ECAP is also presented for comparison.

Prior to heat treatments, PA-ECAP condition possessed the highest microhardness due to combined strengthening effect of precipitates and ultra-fine grains. It maintains its microhardness, with a mean microhardness of 62 HV, for up to 250 °C followed by steady decrease at higher temperatures. H-ECAP shows a similar trend but maintains a mean microhardness of 59 HV up to higher temperature of 300 °C.

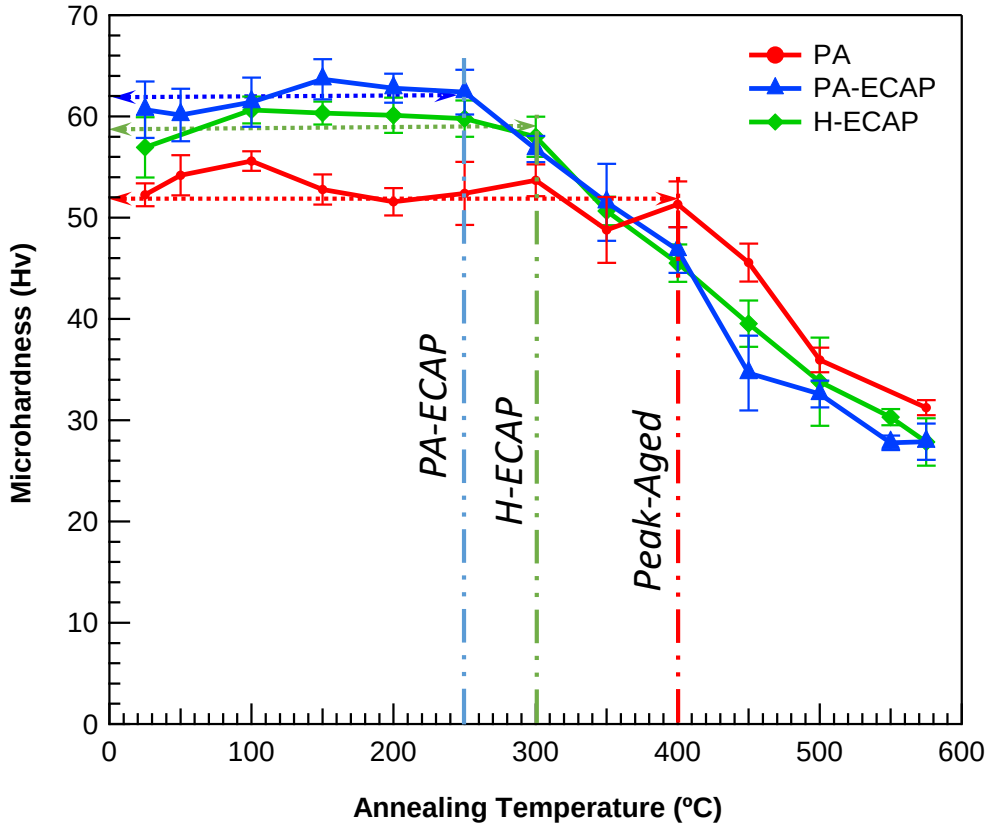

Figure 32 Evolution of microhardness after isochronal annealing heat treatment using temperature step of 50 °C and time of 3 h / step. Dotted lines represent the range of thermal stability for each case. PA has an average microhardness of 52 HV up to 400 °C. H-ECAP has microhardness of 59 HV up to 3000 °C. PA-ECAP has microhardness of 62 HV up to 250 °C.

In comparison, the peak-aged alloy prior to ECAP maintains appreciable microhardness of 52 HV up to 400 °C, which coincidently is also the temperature utilized for achieving the peak-microhardness in this alloy in the two-step aging heat treatment, described in Section 2.1. Precipitates play an obvious role in maintaining microhardness levels when the alloy is exposed to elevated temperatures for extended periods of time, in both pre- and post-ECAP conditions.

In an earlier study, we compared the mechanical response of our current model alloy and an Al-1100 (commercially pure Al with no precipitates) after ECAP, using route 4Bc. In ECAPed condition, Al-1100 showed a sharp drop in microhardness after 150 °C / 3 hr annealing [128]. Horita et al. [129], also reported that yield strength and UTS of ECAPed Al-1100 starts to show decline after 150 °C which was attributed mainly to grain growth at high temperatures in the absence of precipitates.

Figure 33 and Figure 34 shows EBSD orientation maps of Al-Er-Sc-Zr-V-Si in H-ECAP and PA-ECAP conditions at various stages of the isochronal annealing heat treatments. Corresponding grain sizes and their variation with annealing temperature are presented in Figure 35. H-ECAP alloy shows rapid initial growth rate from 0.31 to 0.80 μm at 50 °C, resulting in a polygonised grains and sub-grain structure. Growth of grains and sub-grains in the PA-ECAP alloy can be seen along the direction of the shear plane, which is approximately at an angle of 45° in the micrographs of the flow plane.

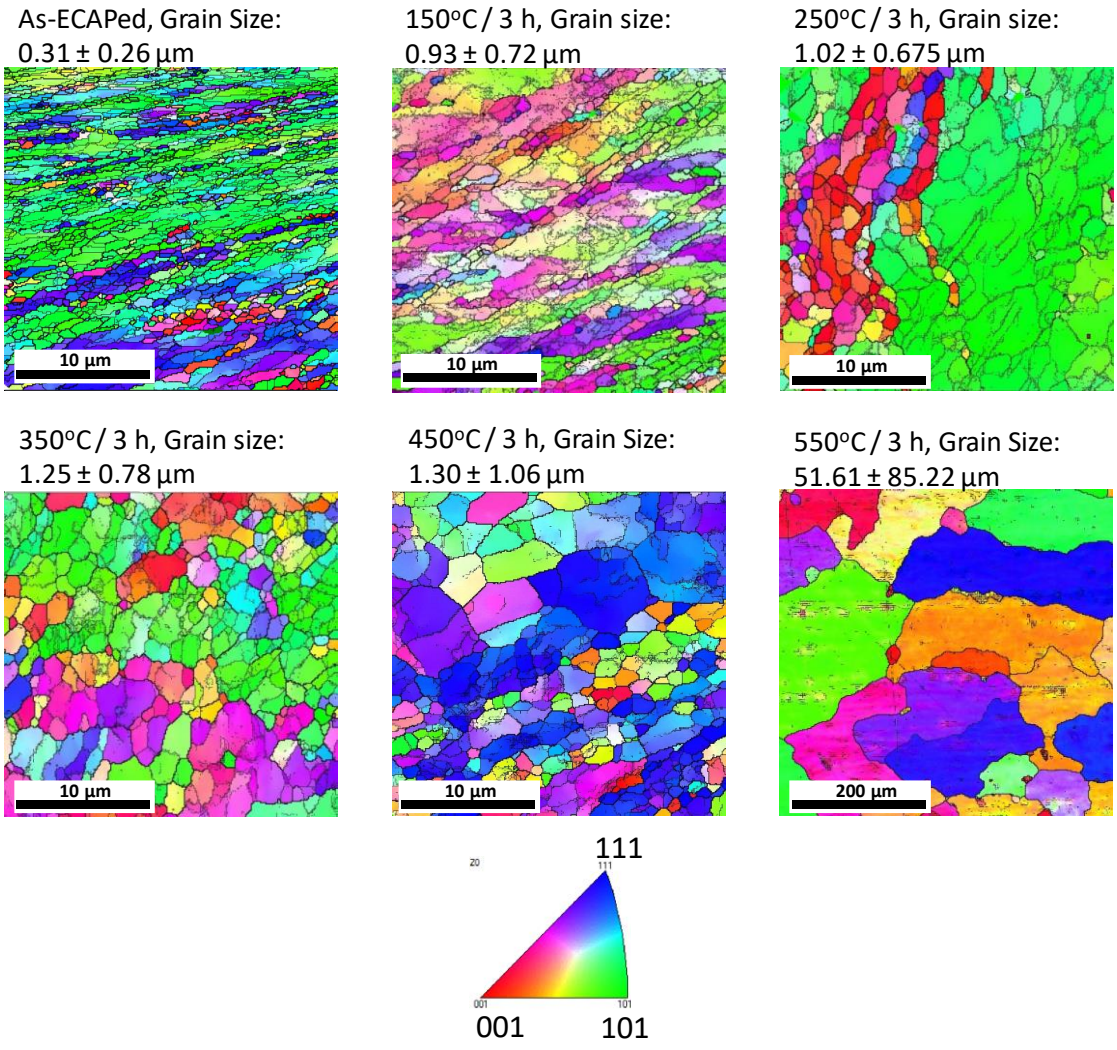

Figure 33 EBSD orientation maps with grain tolerance angle of >1° displaying evolution of microstructure of H-ECAP after isochronal annealing heat treatment using temperature step of 100 °C and time of 3 h / step. Grain growth is relatively uniform up to 350 °C. Discontinuous grain growth is observed at 450 °C and 550 °C.

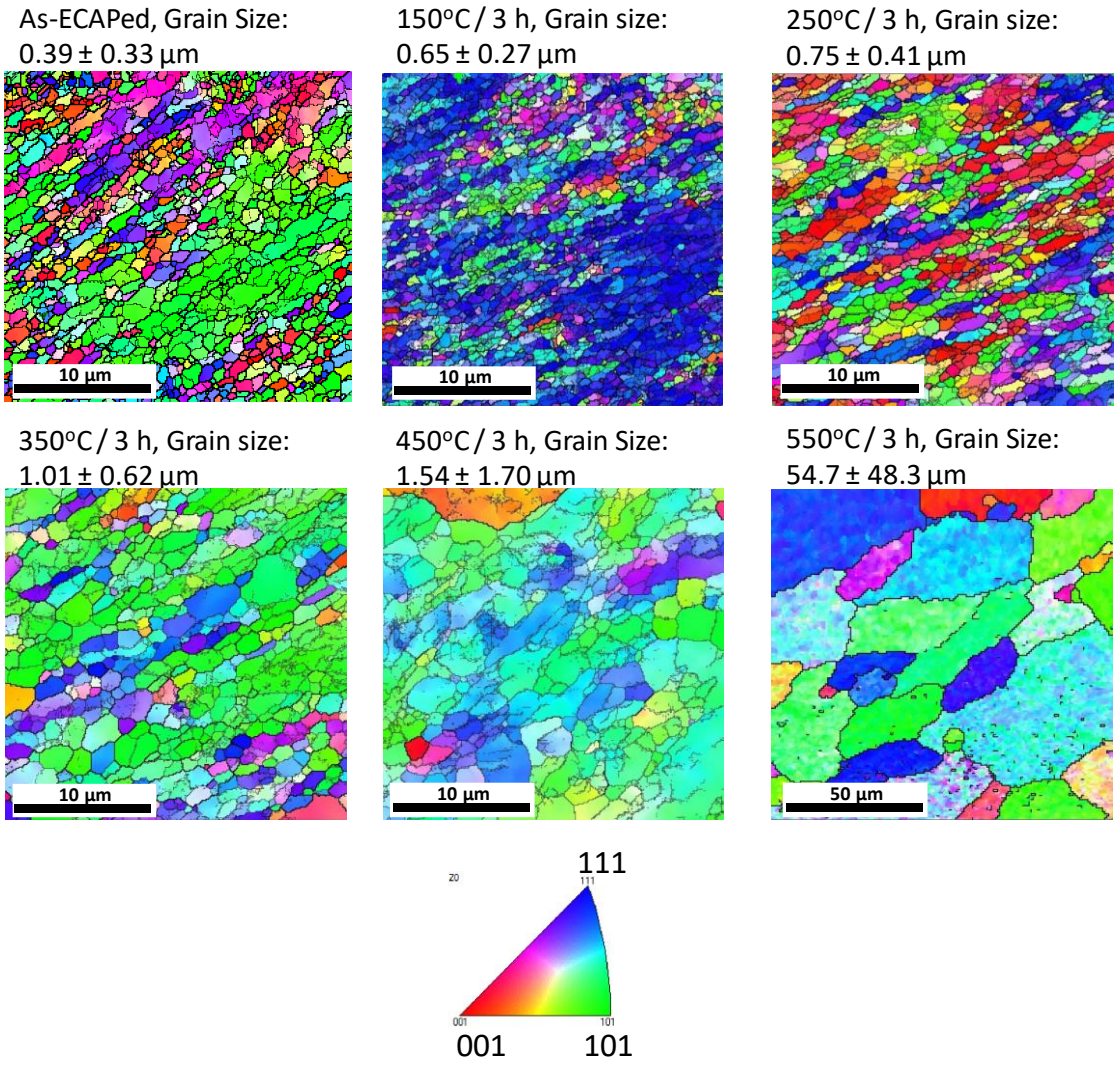

Figure 34 EBSD orientation maps with grain tolerance angle of >1° displaying evolution of microstructure of PA-ECAP after isochronal annealing heat treatment using temperature step of 100 °C and time of 3 h / step. Grain are orientated along the shear plane of ECAP at ~45°. Grain growth is relatively uniform up to 350 °C. Discontinuous grain growth is observed at 450 °C and 550 °C.

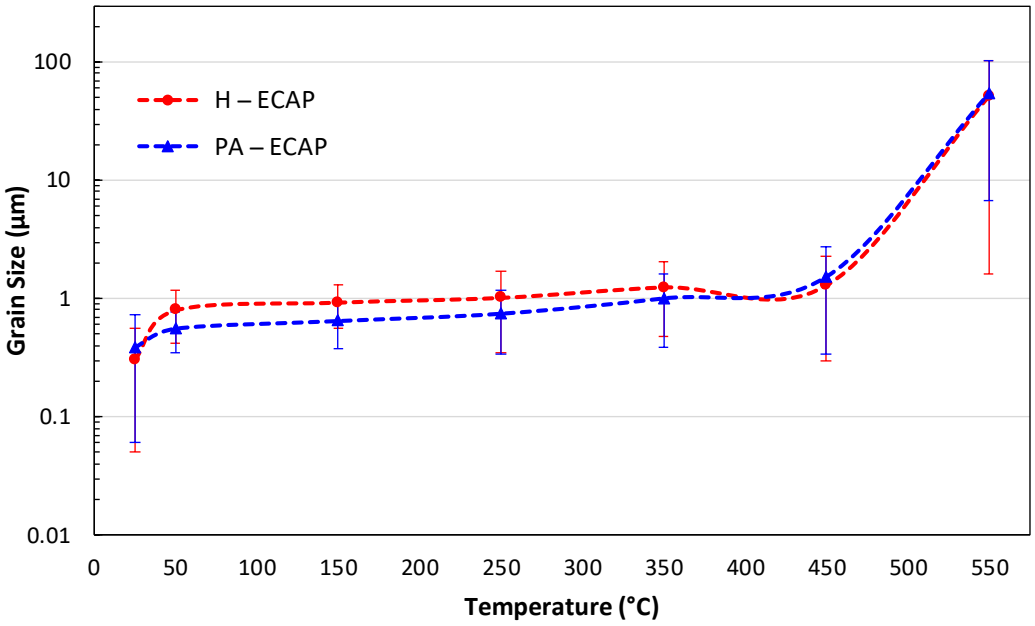

Figure 35 Static grain growth represented by grain diameter as a function of annealing temperature. Grain growth for both remain limited up to 450 °C

Also, the PA-ECAP alloy, shows superior resistance to grain growth as compared to the H-ECAP under similar conditions. However, both conditions display similar trends in grain growth as temperature is increased. Relatively, continuous grain growth was limited up to 450 °C but at 500 °C both conditions exhibit discontinuous grain growth resulting in a more pronounced bimodal microstructure. Similar observation were reported by Bommareddy [130], during annealing of deformed Al(0.1% Sc) using 8 passes of ECAP with 90° rotation. However, it is proved here that as low as 0.013 at. % Sc and substituting the rest of it with lower cost elements of Er, Zr, and V elements can still give a similar response as far as resistance to discontinuous grain growth is concerned.

5.3.2 High temperature tensile properties and strain rate sensitivity

Tensile stress vs. strain plots at temperatures of 200, 300 and 400 °C for H-ECAP, PA-ECAP, and PA alloys, obtained by utilizing initial strain rate of 10^{-4} s^{-1} are displayed in Figure 36. The variations of ultimate tensile strengths and % elongations with temperature are plotted in Figure 37. Solid and dotted lines represent tensile tests at 10^{-4} s^{-1} initial strain rate and % elongations, respectively. As mentioned previously, at ambient temperature the H-ECAP alloy showed comparable strength to the PA-ECAP, which was largely attributed to partial dynamic precipitation during ECAP (Chapter 4). However, the nature of the precipitates that form during ECAP compared to the double-aging heat treatment of cast alloy remains an unanswered question and will be the subject of a subsequent study.

Tensile strength of ECAPed conditions is higher than PA up to 300 °C. A drop in ductility of PA can be observed at higher temperatures whereas ECAPed conditions display increase in ductility with an increase in temperature which is a typical for an ECAPed material having high grain misorientation. At elevated temperatures, H-ECAP alloy possess superior UTS at all test temperatures compared to PA-ECAP alloy. But largely speaking, both ECAPed alloys show similar trends in strength decrease with increase in test temperature accompanied with increase in tensile elongations from 20 % at room temperature to up to 85 % at 400 °C. These trends are largely consistent with earlier reported results on high temperature tensile response of ECAP processed metallic alloys [131]. In comparison, PA condition prior to ECAP has an UTS of 140 MPa at ambient temperature, which is approximately 30 % lower than the ECAPed conditions. At

elevated temperatures, the PA alloy shows a steady drop in strength up-to 300 °C, thereafter at 400 °C it maintains strength of 20 MPa. At about 350 °C, all alloys (with and without ECAP), show similar strengths, which is also consistent with microhardness variation plots presented in Figure 32.

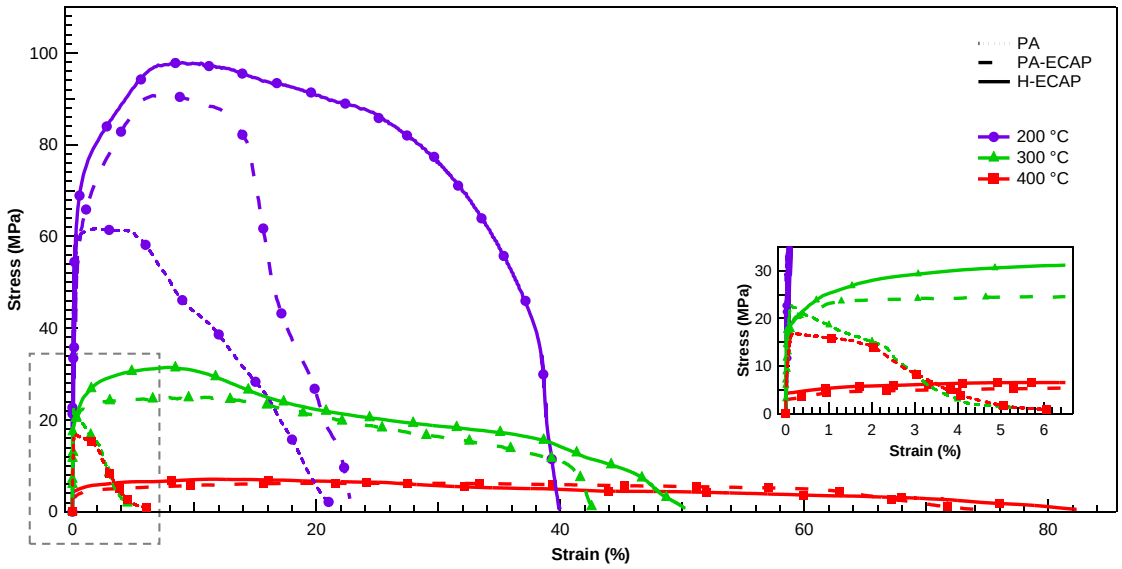

Figure 36 Stress vs. strain plots at 200, 300, and 400 °C, utilizing tensile tests at constant strain rate of 10^{-4} s^{-1}. Line texture represents processing condition of Al-Er-Sc-Zr-V-Si, while colors denote the test temperature. Inset image shows magnified section of 300 and 400 °C plots.

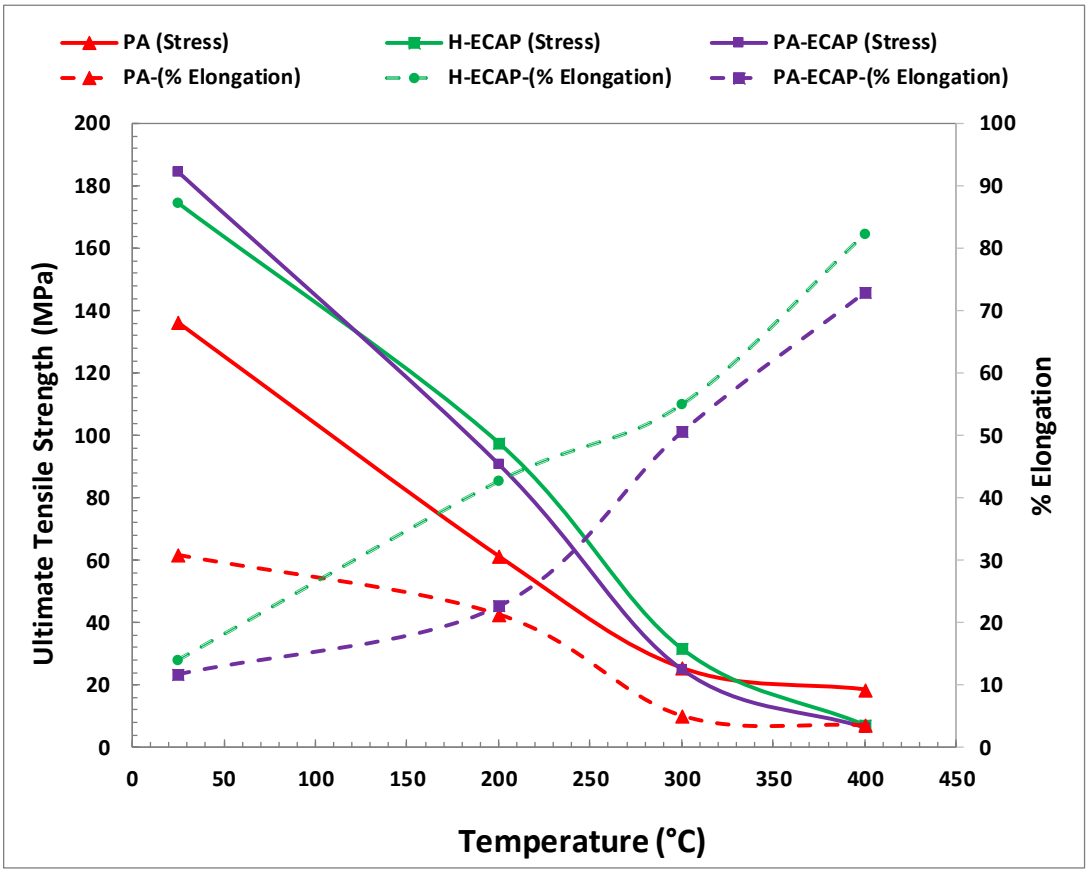

Figure 37 Ultimate tensile strengths and % tensile elongations are plotted as a function of test temperature for Al-Er-Sc-Zr-V-Si alloy in peak-aged (PA), homogenized and ECAPed (H-ECAP) and Peak-aged and ECAPed conditions. Continuous drop in strengths can be observed for all three conditions. PA stabilizes after 300 °C with an average value to 20 MPa.

Strain rate sensitivity of UFG, H-ECAP and PA-ECAP alloys at elevated temperatures was evaluated using decremental step-strain rate tensile test. During strain rate jump test steady strain rate sensitivity is a sum of instantaneous and transient sensitivity, hence, m is computed using the relationship:

$$m = (d \ln \sigma) / (d \ln \dot{\epsilon}) \qquad (1)$$

$$\sigma = [C \dot{\epsilon}^m]_{\epsilon,T} \qquad (2)$$

where flow stress, σ is taken by extrapolating the stress after transient period following the strain rate ($\dot{\epsilon}$) decrement, as also reported by Picu et al. [132]. Empirical constant, C and strain rate sensitivity parameter, m is evaluated from steady-state stress vs. strain rate plots. Steady state stress variation with strain rate for each alloy condition and temperature is shown in Figure 38(a). Figure 38 (b) shows the variation of m values with temperature and both ECAPed conditions showed similar trends in m-value. Similar conclusion was drawn by Xu et al. [133] in their SRS investigation utilizing micro-compression testing on UFG pure Al. The aspects of strain rate sensitivity in micro-alloyed aluminum and its role in dynamic grain growth is discussed in greater detail in the discussions section.

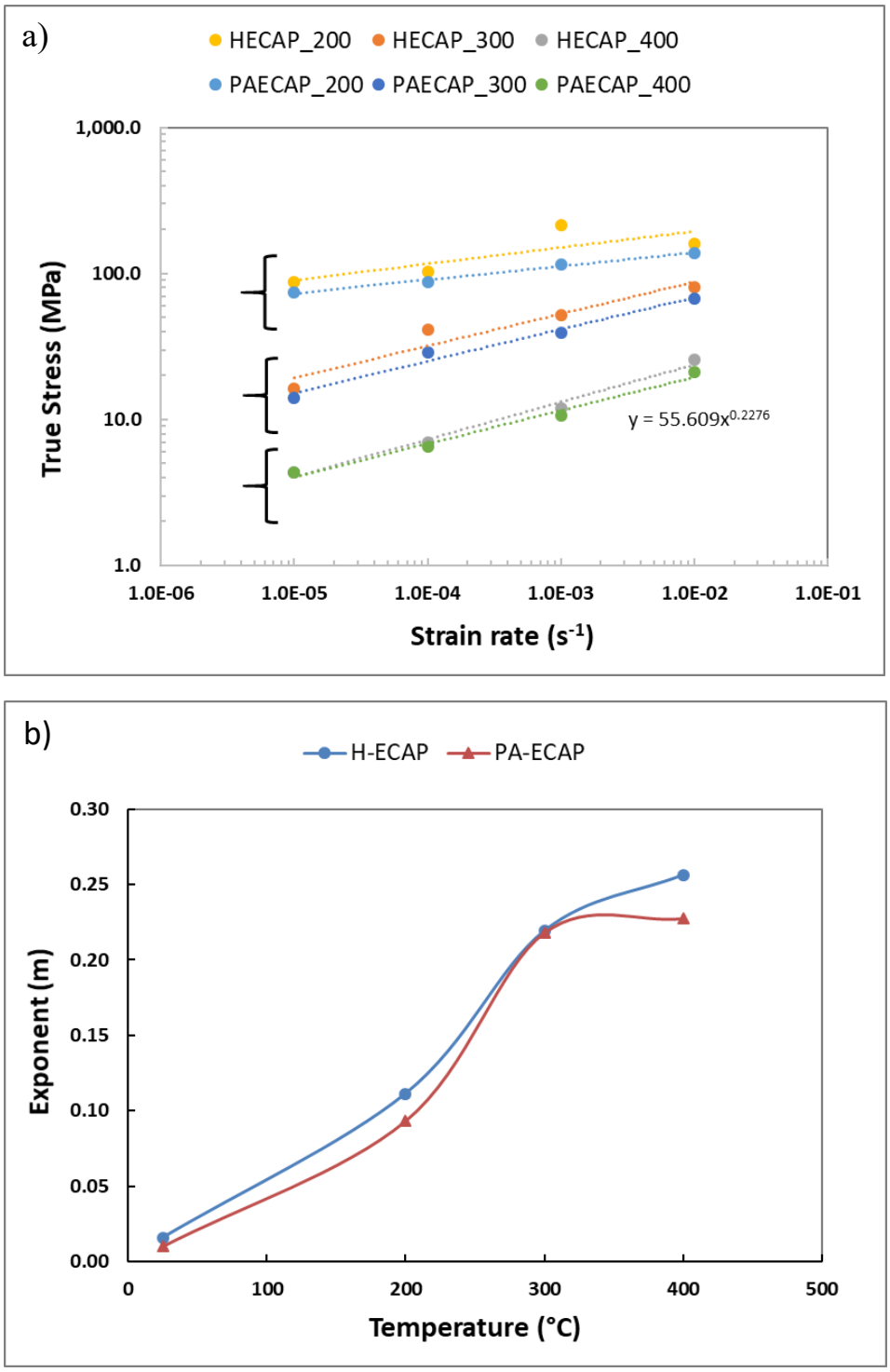

Figure 38 a) Steady state stress values evaluated from decremental strain rate tests and plotted as function of strain rate to calculate strain rate sensitivity (m) values. b) m values plotted as function of test temperature illustrate strong dependence.

5.3.3 Grain growth during static annealing and high temperature tensile deformation

EBSD was carried out to study grain growth in both alloys under dynamic conditions after being subjected to elevated temperature tensile deformation.

Figure 39 shows unique grain color maps of H-ECAP and PA-ECAP with grain tolerance angle of > 5°, prior to deformation (static case), and after 10 % tensile strain at 400 °C. Figure 40 shows the corresponding grain sizes and distribution plots. The static i.e. zero load condition here represents samples exposed to 400 °C for 32.67 min which is the total time it took for the tensile sample to reach set temperature (at 25 °C / min, 16 min) and be deformed to 10% strain (16.67 min). The static grain growth results in similar grain morphologies for both H-ECAP (Figure 39a) and PA-ECAP (Figure 39b) conditions and average grain sizes of 1.40 ± 1.15 µm and 1.29 ± 1.01 µm, respectively.

After 10% tensile strain, in H-ECAP alloy (Figure 39c), a larger grain size of 2.00 ± 1.64 µm evolves and uniform DGG is dominant with a hint of grain rotation mechanism as shown by the alignment and elongation of many grains along the tensile direction (marked on the figure). In comparison, after 10% tensile strain, a grain size of 1.47 ± 1.25 µm evolves in PA-ECAP condition, with some evidence of non-uniform DGG, as shown in Figure 39d.

Figure 40 shows moderate right skewness in grain size distributions with slightly heavy right tails for all conditions. H-ECAP (no load) grain size distribution curve in comparison with H-ECAP (10 %), shows a larger peak and translation towards larger grain size, which also indicates a uniform stress-induced grain growth.

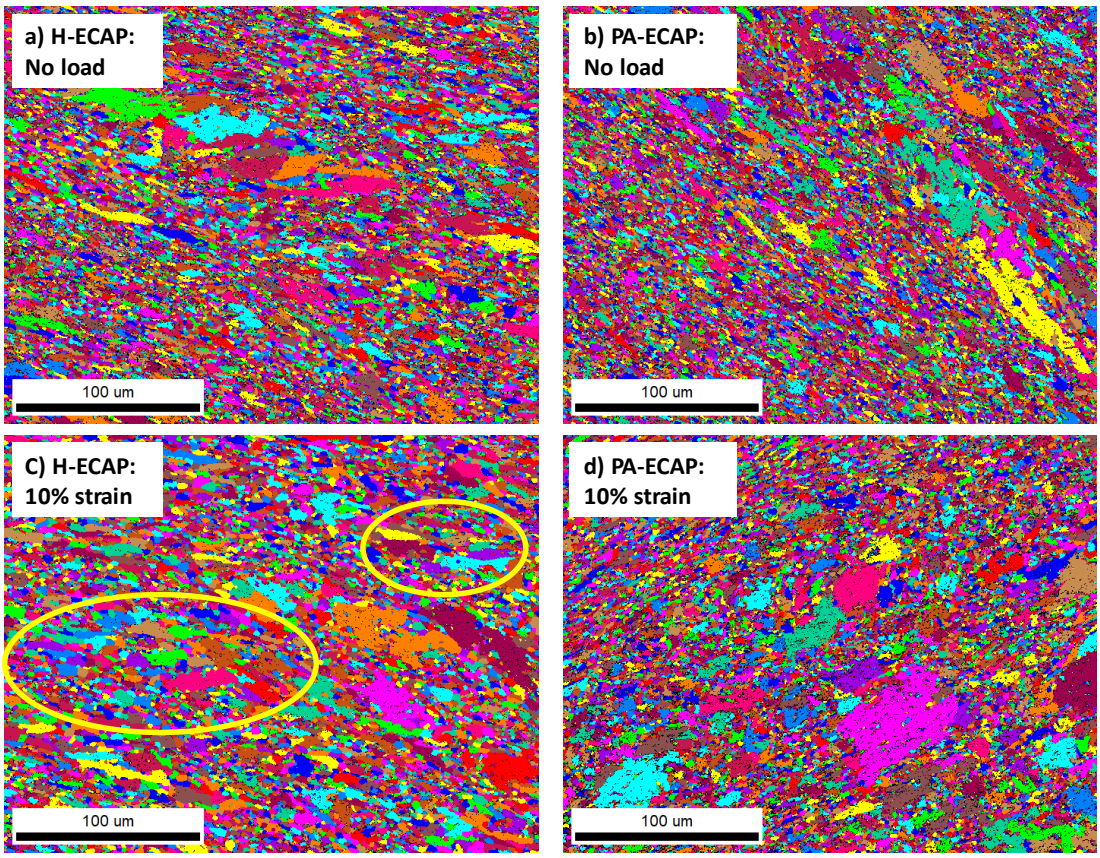

Figure 39 Unique grain color plots with grain tolerance angle of >5°, after static and dynamic annealing (10 % strain, utilizing initial strain rate of 10^{-4} s^{-1}) at 400 °C. Annealing time for 'no load' test conditions was matched with the total time that loaded experiments were exposed to 400 °C

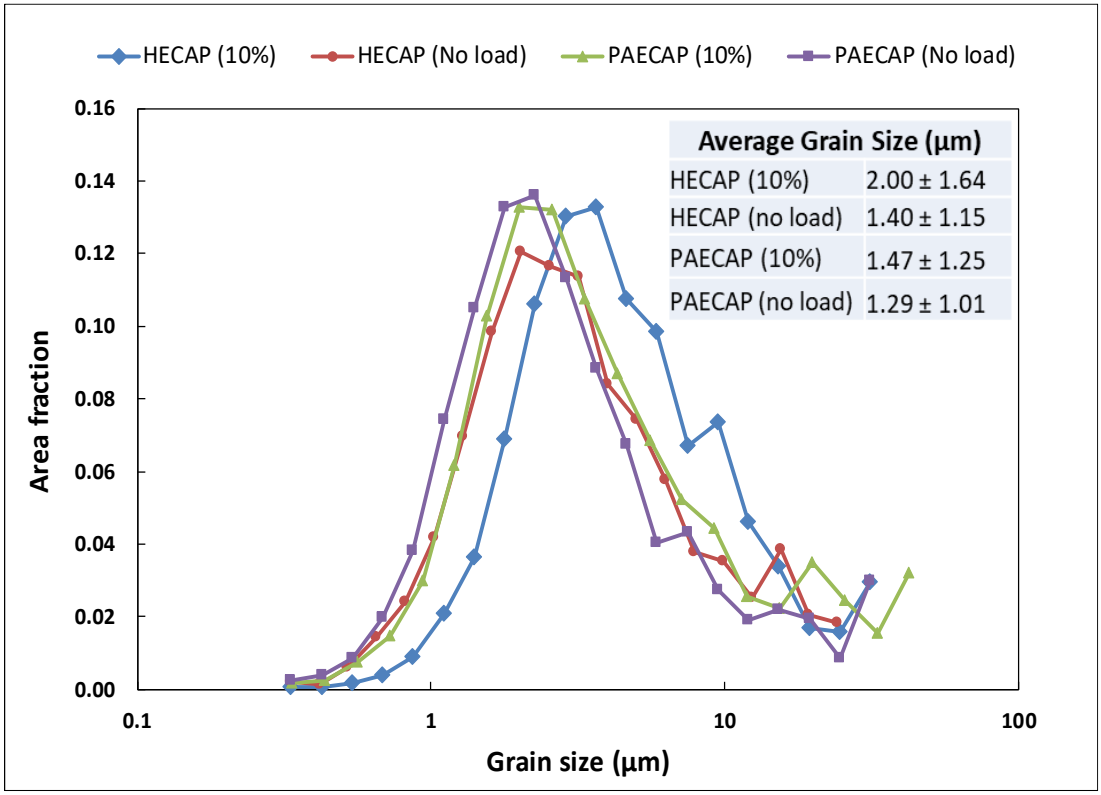

Figure 40 Grain size distribution plots after static (no load) and dynamic annealing (10 % strain, using strain rate of 10^{-4} s^{-1}) at 400 °C.

Second series of interrupted tensile tests were conducted up to 30 % strain to study growth effects in both conditions. Figure 41 shows unique grain color maps of H-ECAP and PA-ECAP alloys after 30 % strain at 400 °C. Figure 42 display the corresponding grain size distributions. Static annealing (no load) heat treatments for this case are for 66 min (heating + holding time). During static annealing, both conditions again maintain fine grain structure and comparable grain sizes (Figure 41 a-b). The PA-ECAP alloy exhibits higher resistance to grain growth, with average grain size of 1.38 ± 0.91 μm, compared to the H-ECAP alloy which has an average grain size of 1.60 ± 1.15 μm. However, under dynamic conditions, after 30% tensile strain, grain growth results in an average grain size of 1.93 ± 2.25 μm in the H-ECAP alloy, which is quite similar to the 10% tensile strain case. Dynamic grain growth in the PA-ECAP alloy showed an increase to 1.76 ± 1.69 μm.

There is now non-uniformity in DGG of the H-ECAP alloy, as shown by multiple peaks of its grain distribution curve. DGG distribution curve of the PA-ECAP alloy shows strong bimodality with first peak appearing at 3 μm and second peak with almost similar area fraction at ~22 μm. The discontinuous DGG comprising of mixed fractions of fine and coarse grains is prevalent in both conditions at higher strains.

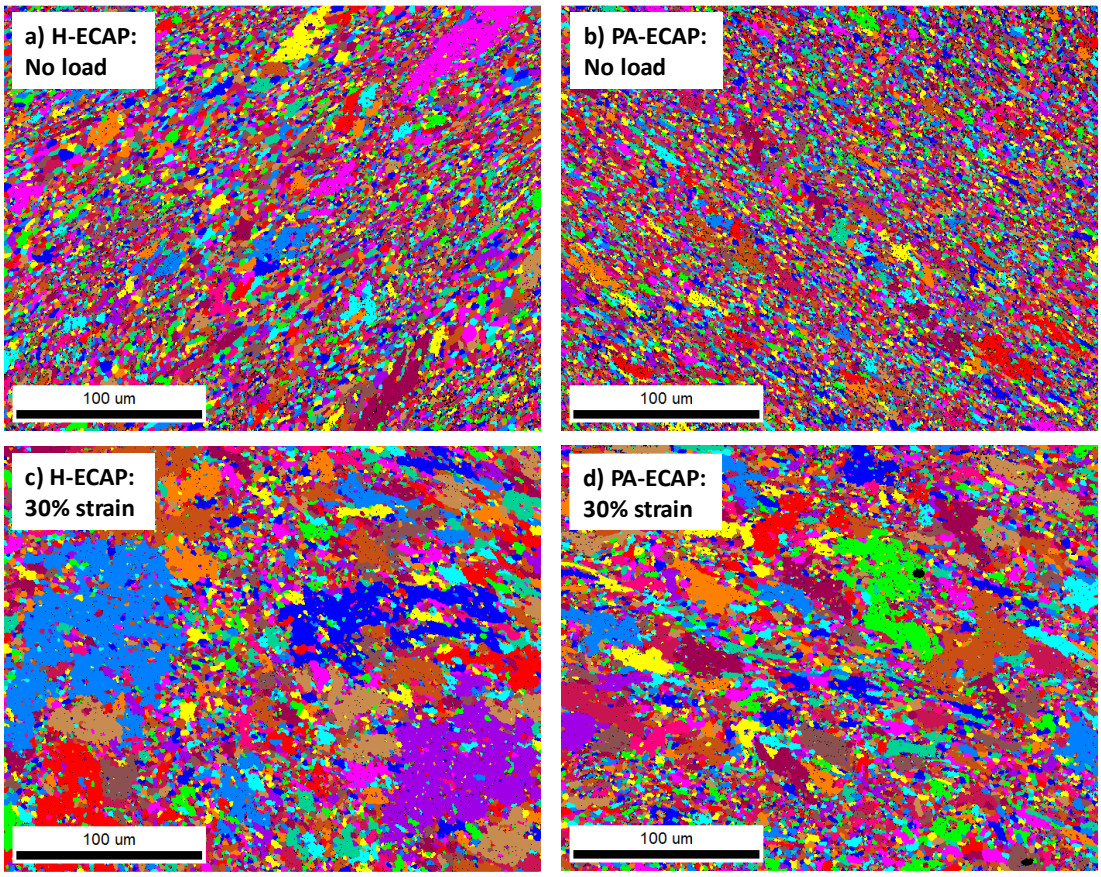

Figure 41 Unique grain color plots with grain tolerance angle of >5°, after static (no load) and dynamic annealing (30 % strain, utilizing constant strain rate of 10^{-4} s^{-1}) at 400 °C. Annealing time for 'no load' test conditions was matched with the total time that loaded experiments were exposed to 400 °C.

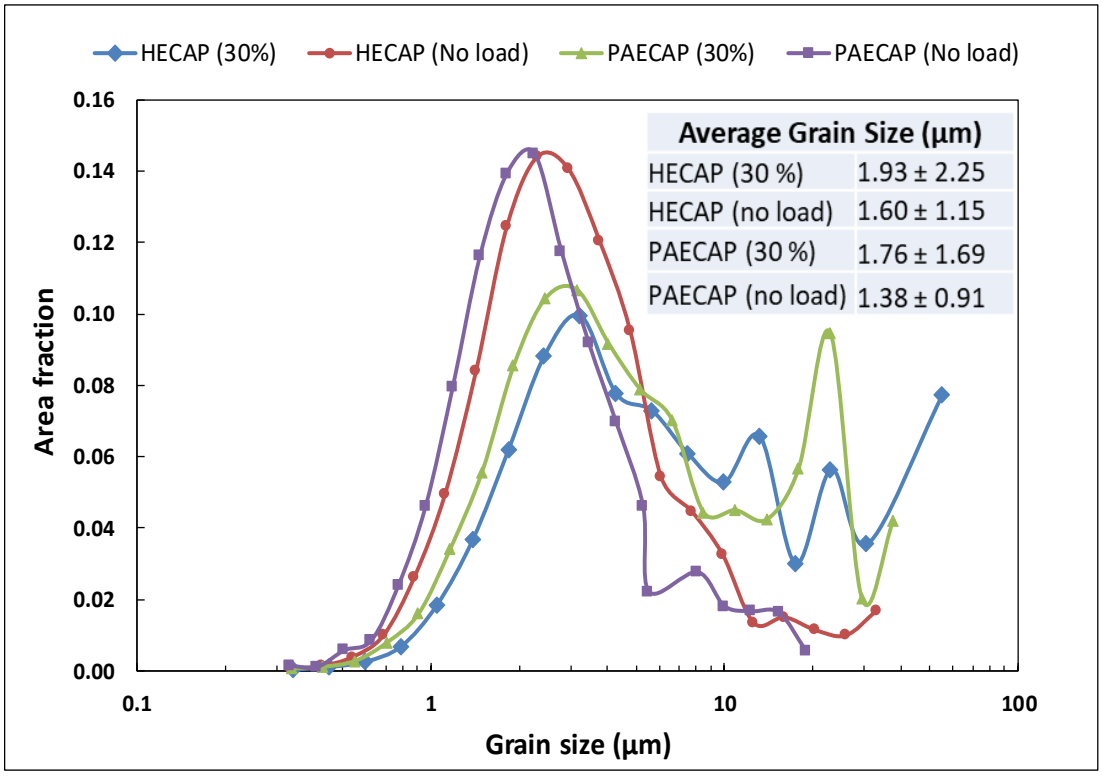

Figure 42 Grain size distribution plots after static (no load) and dynamic annealing (30 % strain, using strain rate of 10^{-4} s^{-1}) at 400 °C.

5.4 Discussions

Ambient and elevated temperature mechanical behavior and microstructure evolution during static and dynamic annealing of a high temperature Al-Er-Sc-Zr-V-Si alloy deformed by equal channel angular pressing (ECAP) was carried out to understand the role of precipitates in maintaining strength i.e. thermal stability, and restraining grain growth.

5.4.1 Strengthening mechanisms and dynamic strain aging

Strengthening in PA condition directly stems from the precipitation of core-shell nano-precipitates as explained by numerous studies on Al-Sc alloys [16], [128], [134]–[136]. In PA-ECAP, strengthening is believed to be due to grain size reduction and dislocation strengthening) as well as due to the presence of precipitates created prior to ECAP by double aging. It was expected for H-ECAP to exhibit strengthening mainly due to grain size reduction after ECAP and some fraction due to solid solution strengthening from alloying additions.

However, previous investigation into H-ECAP led to the conclusion that there is partial dynamic precipitation which occurs during room temperature ECAP of a homogenized Al-Er-Sc-Zr-V-Si alloy (Chapter 4).

Each strengthening mechanism has their specific contribution to the overall stress and they are often considered to follow additive rule with the assumption that they are independent of each other [40], [137]:

$$\sigma = \sigma_o + \sigma_{ss} + \sigma_{ppt} + \sigma_{gs} + \sigma_\rho \qquad (3)$$

where σ_o is the Peierls stress, σ_{ss} is the contribution from solid solution strengthening, σ_{ppt} is the contribution from precipitation strengthening, σ_{gs} is the contribution from grain size strengthening, and σ_ρ is the contribution from dislocation strengthening. These mechanisms are difficult to individually quantify in situations where they superimpose and/or rapidly change when subjected to elevated temperatures. This is because high energy grain boundaries and high dislocation density together with remaining partial degree of supersaturation (for H-ECAP condition) tends to reach thermodynamic equilibrium when subjected to annealing. Consequently, the alloy can undergo reduction in strength due to grain growth and precipitate coarsening and concurrent increment in strength due to decomposition of saturated solid solution. This mechanism can be used to explain thermal stabilities (ability to maintain hardness) of PA-ECAP and H-ECAP in Figure 32. Partial dynamic aging during annealing treatment allows the thermal stability range in H-ECAP up to 300 °C. Whereas, microhardness in PA-ECAP alloy shows a drop after 250 °C, since the precipitates in this alloy are expected to have higher coarsening kinetics compared to its undeformed counterpart (PA alloy). This is because SPD processed alloy have increased dislocation and vacancy density and high grain boundary area that increases effective diffusion coefficient of the alloy and reduces time/temperature at which maximum hardness can be sustained [40], [71], [138]. Consequently, we observe higher thermal stability (ability to maintain hardness) range, of up to 400 °C in PA alloy, with mean microhardness of ~52 HV. Difference in the mean microhardness between H-ECAP and PA-ECAP corresponds to the difference in grain size plateaus in the same temperature range (50 to 450 °C) shown in Figure 35.

Dynamic strain aging can be substantiated by the transient UTS curve of H-ECAP at 200 °C as shown in Figure 37. J. Morris [139] discussed some characteristic flow stress vs. temperature curves for aluminum alloys which are subjected to dynamic strain aging behavior. The transient behavior in the curve signifies the extent of dynamic strain aging in an alloy. It is observed in Figure 37 that H-ECAP surpasses stress levels of PA-ECAP at all temperatures above room temperature which is attributed to partial dynamic strain aging. However, dynamic strain aging has occurred to a lesser extent since there already had been partial precipitation during ECAP as discussed in the previous chapter. Higher grain growth resistance of H-ECAP, particularly at temperatures above 400 °C, is also attributed to concurrent precipitation during static annealing.

Ductility has also been observed to be higher for H-ECAP with up to 82 % elongation at 400 °C. This is a consequence of higher intragranular precipitation instead of intergranular. Figure 43 shows TEM images of H-ECAP and PA-ECAP taken from the flow planes. No significant grain boundary precipitation can be seen in H-ECAP (Figure 43a) whereas evidence of intragranular precipitation in H-ECAP can be observed in Figure 43b. In contrast, precipitates in PA-ECAP can be seen decorating along the grain boundaries in Figure 43c. Higher magnification TEM of PA-ECAP in Figure 43d shows a combination of intergranular as well as intragranular precipitation. During conventional aging grain boundaries act as preferred nucleation sites for precipitation [16], [140]. However, ECAP of a supersaturated solid solution can suppress intergranular precipitation and assist precipitation in grain interiors due to numerous nucleation sites in form of high dislocation density and vacancies [141]. L. Jiang et al. [142] also reported exceptional

increase in ductility of UFG Al-Cu-Sc by suppressing intergranular precipitation and promoting it in the grain interiors. On the contrary, low ductility in PA may also be attributed to intergranular precipitation assisted grain boundary fracture.

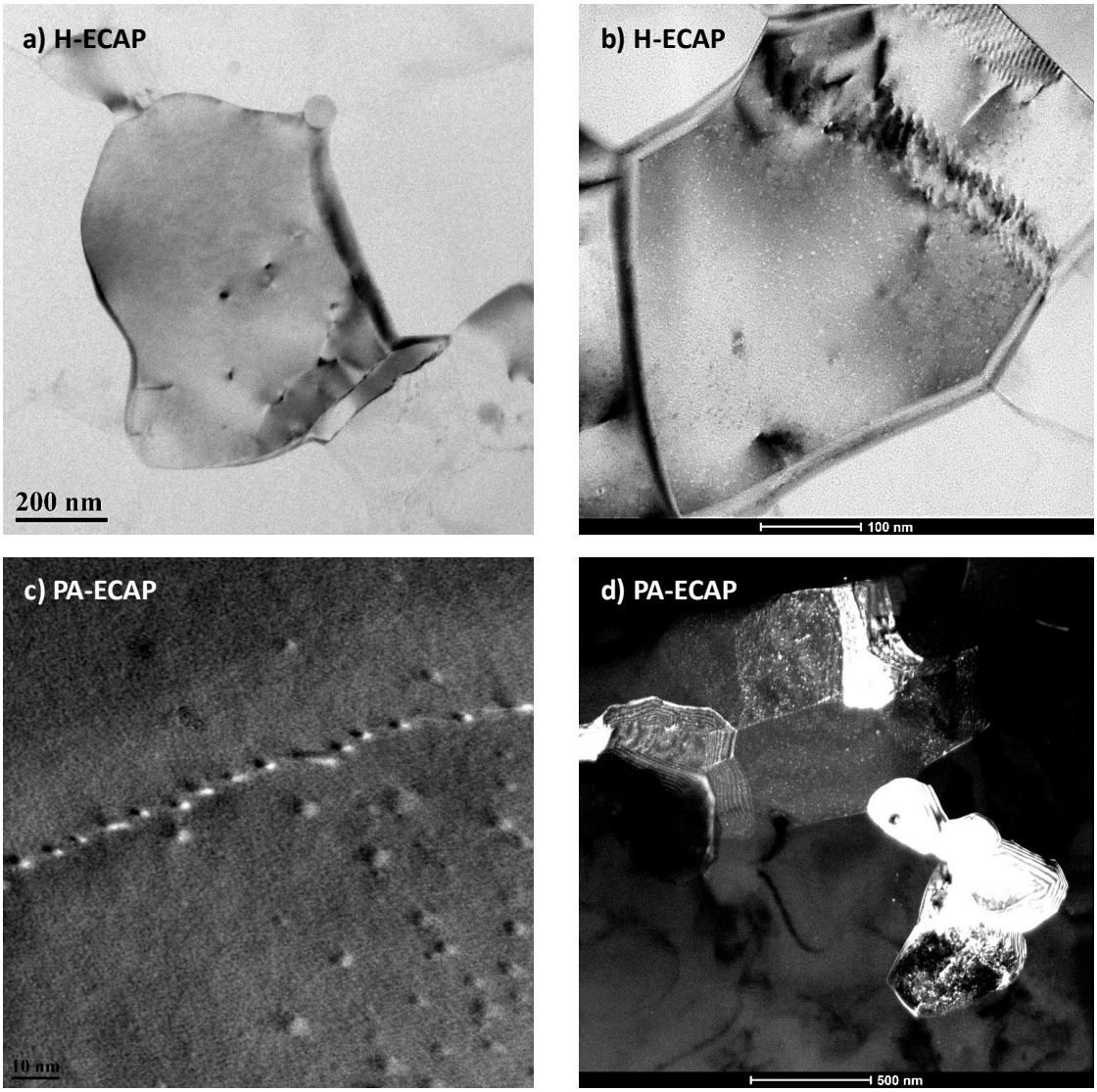

Figure 43 (a) TEM from the flow plane of H-ECAP show essentially precipitate free grain boundaries. (b) High magnification TEM of H-ECAP show finely distributed nanosized precipitates in the grain interior. (c) Precipitates in PA-ECAP decorating along the grain boundary. (d) High magnification shows grain interior precipitation with high fraction of precipitation along grain boundaries as well.

Strain rate sensitivity is another important parameter that gives insight into material deformation behavior at varying strain rates. Results in Figure 38 indicate that there is a strong dependence of SRS on temperature for both ECAPed conditions. This is attributed to high dislocation density as also reported by Hu et al. [133]. For Al-Er-Sc-Zr-V-Si, SRS is further enhanced by interaction of dislocations with nano-precipitates. Temperature plays a role by increasing dislocation mobility and reducing the mean free time for interaction with precipitates. SRS higher than 0.25 for H-ECAP after 300 °C may also be attributed to intragranular dynamic strain aging.

5.4.2 Static grain growth as a function of annealing temperature

Remarkable grain coarsening resistance, under 2 µm diameter for up to 450 °C, has been observed for PA-ECAP as well as H-ECAP. The comparable growth behavior of H-ECAP is due to partial dynamic precipitation and accelerated aging kinetics as discussed earlier. A. Bommareddy et al. [130] compared the grain diameter as a function of annealing temperature of Al-0.1%Sc. Results of Al-Sc-Er-V-Si alloy (H-ECAP and PA-ECAP) here show similar trend but higher grain growth resistance compared to Al-0.1%Sc alloy. However, it is also necessary to mention that Al-0.1%Sc alloy in their study was subjected to 8 passes ECAP and 10 h / step isochronal annealing treatment. Nevertheless, it is important to highlight our present findings that Sc content as low as 0.013 at. %, with partial substitutions of Er, Zr, and V, can also effectively maintain refined grain structure up to 450 °C.

EBSD images in Figure 33 and Figure 34 for H-ECAP and PA-ECAP, respectively, shows resistance to discontinuous grain growth up to 450 °C which was also

observed by Bommareddy et al. [130]. Nano-trialuminide precipitates play a vital role in restraining both continuous and discontinuous grain growth. A study on commercial pure aluminum deformed using 8Bc ECAP route could maintain microstructure stability at temperature below 250 °C and discontinuous grain character appears in temperature range of 275 – 300 °C [143].

5.4.3 Mechanisms and kinetics of stress-induced grain coarsening

Stress-induced grain growth has important implications for this alloy in applications where it will undergo stress at elevated temperatures. Grain boundaries are high energy areas and grain growth occurs to lower the excess free energy [115]. Characterization of DGG has been used here to compare the kinetics with that of SGG and understand the effective role of precipitates in each case. It can be observed from Figure 39d that discontinuous grain growth starts in PA-ECAP with only 10 % strain at 400 °C. While there is still noticeable resistance to grain growth for both conditions after 10 % strain (corresponding to 32.67 min static annealing), onset of transition from continuous to discontinuous grain growth in PA-ECAP (10 % strain) has been sharply accelerated compared to static annealing where it first appeared during 450 °C / 3 h annealing heat treatment. However, H-ECAP still display relatively uniform and continuous grain growth. Discontinuous DGG in PA-ECAP is imposed by Zener-drag on a large fraction of grains due to pinning of precipitates at the grain boundaries. Ability of precipitates in stabilizing the grain and sub-grain structure of a deformed alloy is well established and reported for Sc containing aluminum alloys [144].

Unique grain color maps in Figure 41 shows sharp abnormal stress-induced grain growth when H-ECAP and PA-ECAP are subjected to 30 % strain. At this point, H-ECAP is believed to have been fully dynamically aged with both intergranular and intragranular precipitation. Precipitation along the grain boundaries effectively maintains the sub-grain structure and precipitation which is only of intragranular character, allow the grains to rotate and grow along the tensile deformation direction. As a result, we observe multiple peaks in H-ECAP grain size distribution as shown in Figure 42. For PA-ECAP, there is also strong bimodal DGG, however there is limited grain rotation as evident from grain orientation which is maintained along shear plane of ECAP due to effective pinning. Hence, the primary deformation mechanism in PA-ECAP is grain boundary migration and sliding. High tensile ductility of 70 – 80 % in ECAPed alloys at 400 °C is also a consequence of inhomogeneous grain growth, as reported by authors previously in their deformation studies of nanocrystalline and UFG alloys [116], [145], [146]. Han et. al. [147] compared tensile ductility in nanostructured aluminum alloys processed by SPD and powder metallurgy, and found that there is a general trend of decrease in ductility with grain refinement, however, development of bimodal structure by adding small volume fraction of un-milled coarse-grained powders improves the ductility of the alloy.

In this study, such bimodal microstructure is spontaneously produced during high temperature deformation. Fine grains contribute to the strength according to Hall-Petch relation, while coarse grains allow enhanced dislocation mobility resulting in higher ductility.

Kinetics of grain growth during static and stress-induced annealing can be described by the grain growth relationship:

$$R^n - R_o^n = Kt \qquad (4)$$

Where R and R_o are final and initial grain radius at time t, n is the grain growth exponent which is generally between 2 and 4, $n = 3$ is expected for grain growth in alloys with the presence of fine precipitates [148]. K is defined by an Arrhenius type relation given by $K = A\exp(-Q/RT)$, where A and R are constants, T is absolute temperature and Q is activation energy.

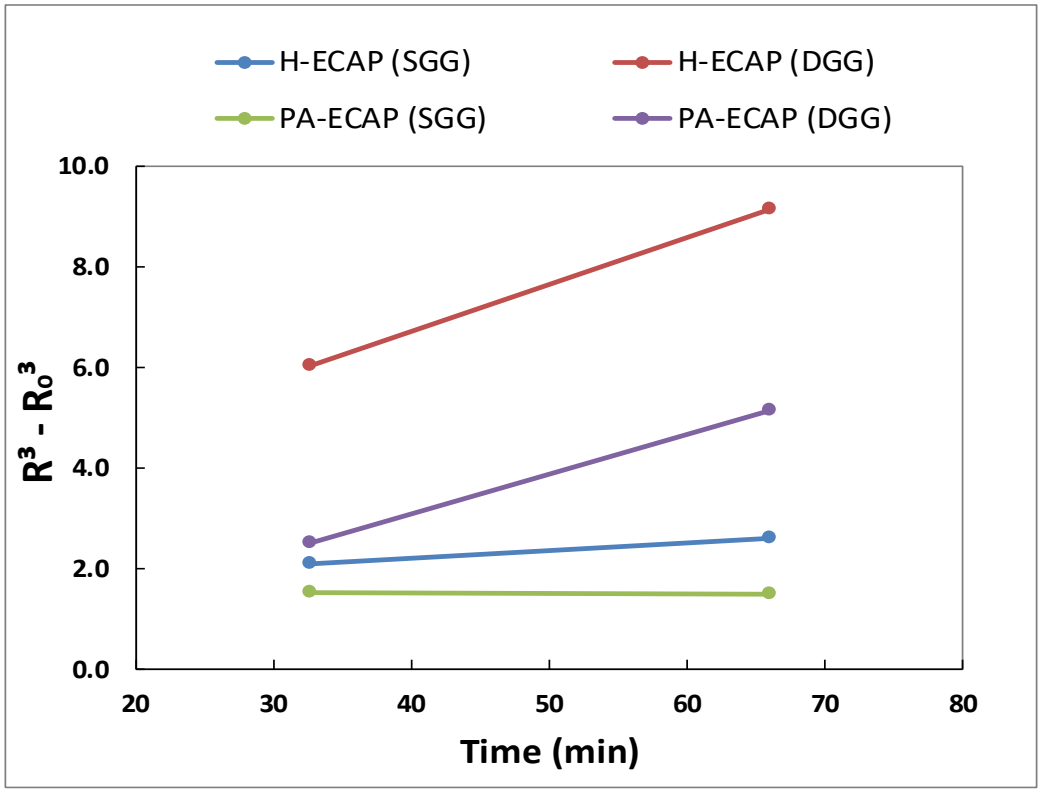

Figure 44 Grain radius difference ($R^3 - R_o^3$) plotted as a function of annealing time at 400 °C, under static (SGG) and stress-induced (DGG) conditions.

Figure 44 shows the plot of grain radius difference ($R^3 - R_o^3$) as a function of annealing time according to Equation 4, with grain growth exponent of 3. Under static conditions, PA-ECAP has the highest grain coarsening resistance and slowest kinetics as compared to H-ECAP which is consistent with grain growth results at various temperatures discussed in Section 4.2. During DGG there is a ~5 – 6 fold increase in grain growth kinetics. H-ECAP alloy does not exhibit significant difference in DGG kinetics compared to PA-ECAP alloy. Hence, it can be concluded that there is no effect of partial dynamic precipitation and DSA on DGG kinetics of H-ECAP alloy. However, their effect is clear in terms of the magnitude of grain growth and the difference in mechanical properties of H-ECAP and PA-ECAP alloys.

5.5 Conclusions

Al-Er-Sc-Zr-V-Si alloy was subjected to ECAP route 4Bc at ambient temperature before and after peak-aging heat treatment. The following conclusions were made:

1. There is a slight tradeoff between mean microhardness and thermal stability range. PA-ECAP has the highest mean microhardness of 62 HV with stability range up to 250 °C. H-ECAP has slightly low microhardness of 59 HV with range of up to 300 °C. In contrast PA condition has highest thermal stability range up to its aging temperature of 400 °C but at an even lower mean microhardness of 52 HV.
2. H-ECAP and PA-ECAP both show high resistance to grain coarsening during isochronal annealing. Transition from continuous to discontinuous grain growth was observed at 450 °C for both alloys. This also corresponds to the decrease in microhardness. PA-ECAP exhibited higher resistance to grain growth up to 350C

than H-ECAP due to Zener pinning effect on the grain boundaries. At 450 °C and beyond, H-ECAP has relatively lower average grain diameter due to concurrent aging and pinning of precipitates during annealing.

3. Dynamic strain aging (DSA) in H-ECAP alloy was evaluated from the transient in the tensile strength vs. test temperature curve, which allows higher strength than PA-ECAP at these temperatures. Reduction in strength due to grain coarsening is compensated by nucleation of precipitates when subjected to elevated temperatures. Higher ductility and strong dependence of strain rate sensitivity to temperature for H-ECAP is expected to be due to intragranular precipitation during DSA.
4. Different mechanisms of DGG were observed in H-ECAP and PA-ECAP. In PA-ECAP grain growth was due to boundary migration and sliding and maintained the direction of ECAP shear plane. After DGG in H-ECAP, grain rotation along the tensile direction, in addition to boundary migration and sliding, was observed from EBSD pole figures. Transition from continuous to discontinuous DGG for PA-ECAP was observed after 10% strain. H-ECAP still maintained continuous and uniform DGG at this strain. Different modes of grain growth also play an important role that results in higher strength for H-ECAP compared to PA-ECAP. Discontinuous DGG was observed in both alloys at 30 % strain.
5. DSA and delayed on-set of continuous to discontinuous grain growth in H-ECAP had no effect on kinetics of grain growth as compared to PA-ECAP. However, the magnitude of SGG and DGG was higher for H-ECAP at these test conditions.

CHAPTER VI
EFFECT OF VANADIUM, NIOBIUM OR TANTALUM MICRO-ALLOYING ON THE MECHANICAL AND ELECTROCHEMICAL PROPERTIES OF AL-ER-SC-ZR-SI ALLOY

6.1 Introduction

In the last decades transition and rare earths (RE) micro-alloying additions in aluminum has been investigated widely to substitute the iron-based alloys and titanium alloys exposed to intermediate temperatures (250–400 °C) and low stresses i.e. < 20MPa [14]. The age-hardenable Al-Sc alloys containing nanosized and coherent Al3Sc (L12-ordered) precipitates are extensively used for high-temperature structural applications including aerospace and automotive systems owing to their high strength/weight ratio, toughness, good oxidation resistance, and good electrical properties. Past studies showed that Sc, Zr etc. micro-alloying addition improves the strength and creep resistance temperatures at higher temperature (above ~250 ºC), corrosion resistance, and other service performance, by forming coarsening resistant Al3(ScxZr1-x) (L12) core-shell precipitates [12], [16], [24], [149]–[151]. Further, to reduce the cost of dilute Al-Sc-Zr alloys associated mainly with Sc without compromising on the creep resistance, replacement of Sc with lower-cost Erbium (Er) has proven to be effective. In Al-Er-Sc-Zr alloys, precipitates structure consists of core/double-shell structure where Er-enriched core is surrounded by Sc-enriched and Zr enriched inner and outer shell respectively [24]. Moreover, in recent years, extensive research has been dedicated to find other alloying elements which can further improve the service temperature and replace some of the Sc

content, while maintaining the requirement of forming coherent tri-aluminide nanoprecipitates (L12-ordered) [152]. Recently, Erdeniz et al. investigated the effect of micro-addition of Vanadium on coarsening and creep-resistant properties of Al-Er-Sc-Zr-Si alloys. The authors reported that after optimizing the peak-aging parameters, the alloy showed a maximum hardness of *600 MPa due to the presence of L12-ordered, coherent Al3(Er,Sc,Zr,V) precipitates [16].

While precipitation hardening improve the certain properties of Al alloys, it also introduces electrochemical heterogeneities which promote the corrosion [153]. These precipitates form galvanic couples between matrix and themselves which lead to severe intergranular corrosion (IGC). The spontaneous formation of thin invisible oxide layer on Al surface upon exposure to corrosive solution, is a key characteristic of aluminum. This highly resistive and self-protecting skin on Al avoids the further oxidation of underlying metal and protects it until the film breakdown. Moreover, it was reported that compared to non-heat-treatable alloys, increasing alloying content in heat-treatable alloys also results in the formation of nonhomogeneous surface film. The nonhomogeneous oxide layer is usually more susceptible and sanitized to the onset of localized corrosion [154]. Hence, a tradeoff exists between mechanical and corrosion properties in precipitation hardenable Al alloys [153].

The alloying addition of Zr and Sc to Al has been proven effective in terms of corrosion resistance by improving the properties of oxide film present on the surface [155]. Neubert et al. reported that Sc containing Al alloys forms oxide film consisting of Sc2O3 fine particles and dense and less defective layer of Al oxy-hydroxides. The protection

action of Sc can be divided into two parts, first fine Sc2O3 mechanically blocks the surface and promotes the sluggishness of the pits occurred. Second, the partial dissolution of Sc increases the vacancy concentration in the oxide layer results the increased thermodynamic activity of Al in the defective oxide layer thereby promoting the formation of thick and compact dense oxide layer [155]. Also, the role of Zr in improving corrosion resistance of Al-Sc-Zr is similar as it does in conventional Al alloys. In Al-Zr alloys, Zr enriches the surface layer owing to its lesser electronegativity and higher affinity to oxygen compared to pure Al [156]. Similarly, Bhardwaj et al. studied the surface oxide properties of Al-Ta alloys using scanning tunneling microscopy in 0.01M NaCl solution and showed that Ta reduced the Al rate of dissolution about 100 times compared to pure Al sample for the first 30 h of immersion. The investigation releveled that concentration of Ta species in the oxide layer were more than Al and where Al-Ta bonds are stronger than Al-Al bonds resulting compact oxide layer. This behavior was probably blocking the paths used by Cl- ions to reach the oxide/metal interface [157]. Similarly, a study made on influence of Nb and V on surface films of titanium-based alloys, showed increased corrosion resistance in order of Ti-Nb>Ti>Ti-V. The protection action of Nb was attributed to the stabilizing effect of the Nb+5 cations on the passive film formed at the Ti surface. The stoichiometric defects such as anion vacancies caused by the presence of sub-oxides were compensated by Nb+5 cations. The alloy containing V showed sensitivity towards the localized corrosion which was correlated to the dissolution of vanadium at the electrolyte/oxide film interface. The dissolution reaction was attributed to the solid-state diffusion process at interface comprised of generation of cation vacancies and their

diffusion through the oxide film [158], [159]. Rosalbino et al. evaluated the influence of heavy rare earth elements i.e. Er on the corrosion properties of Al-Er and Al-Mg-Er alloys in borate buffer 0.1 M NaCl solutions. The investigation revealed that as the concentration of Er increases in the alloy, it appears to provide a beneficial effect on the corrosion behavior of the investigated alloys. The protection action of the Er in Al-Er alloy was described as improved stability of oxide/passive film due to less negative effects exerted by the Al3Er-matrix galvanic coupling compare to other phases that predominates at low Er contents [160].

The current interest in micro-alloyed Al with multiple elements centers on an excellent combination of mechanical properties without sacrificing its service performance in corrosive environment. Therefore, in present research the purpose is to study the synergistic effects of micro-alloying addition of V, Ta, or Nb to Al-Er-Sc-Zr-Si alloys on the mechanical and corrosion behavior using tensile testing and electrochemical techniques, respectively. The detailed microstructural characterization, trialuminide nanoprecipitates analysis and creep properties of micro-alloyed Al-Er-Sc-Zr-Si (BM), Al-Er-Sc-Zr-Si-V (BM-V), Al-Er-Sc-Zr-Si-Ta (BM-Ta), and Al-Er-Sc-Zr-Si-Nb (BM-Nb) alloys have already been discussed elsewhere indicating the wider application of these alloys [16], [134], [150], [161], [162]. Moreover, the review by Luca et al. also discussed briefly the effects of rare-earth, transition metals, inoculants and solid solution elements onto the L12 Al3M precipitates [152]. In this study the preliminary investigations are undertaken as the mechanical and corrosion behavior of these alloys has not been previously explored.

6.2 Materials and Methods

6.2.1 Fabrication and Mechanical Characterization

The peak aged alloys for corrosion studies were used as-received. The alloys are cast aluminum with micro-alloying additions of Sc, Er, Zr, V, Si, and X (where X = V, Nb, or Ta). Nominal compositions of Al–Sc–Er–Zr–Si alloys with V, Ta and Nb labeled as BM, BM-V, BM-Ta, BM-Nb respectively are given in Table 9. The as-received peak-aged alloys were cast according to the procedure mentioned elsewhere [16], [134]. A short description for the casting procedure is as follows. Four alloys with nominal composition were arc-melted with the target composition (Table 9) (flipped and re-melted five times) in a water-cooled copper hearth furnace, using 99.99 at.% pure Al, 99.9 at.% pure Nb, 99.9 at.% pure Ta, and master alloys consisting of Al–5.9 wt% Er, Al–2 wt% Sc, Al–8 wt% Zr, and Al–12.6 wt% Si. The alloys were subjected to a homogenization treatment at 640 °C for 4 h. Following homogenization treatment, each alloy was peak-aged utilizing the time/temperature aging profile as optimized by Erdeniz et al. for BM, BM-V [16] and BM-Ta, BM-Nb [134].

To evaluate the mechanical properties of Al-Er-Sc-Zr-Si-X, tensile tests on BM-V, BM-Nb, and BM-Ta were carried out at room temperature and elevated temperature (200 °C). Tensile tests were carried out using MTS 30 kN test frame with contactable high temperature extensometer to maintain constant strain rate of $1x10^{-3}$ s^{-1}. To ensure repeatability of results, at least two specimens were tested at each temperature.

Table 9 Nominal composition in at. %, of alloying additions in aluminum.

Specimen	Sc	Er	Zr	Si	V	Ta	Nb	Al
BM	0.02	0.005	0.07	0.06	-	-	-	Bal.
BM-V	0.02	0.005	0.07	0.06	0.08	-	-	Bal.
BM-Ta	0.02	0.005	0.07	0.06	-	0.08	-	Bal.
BM-Nb	0.02	0.005	0.07	0.06	-	-	0.08	Bal.

6.2.2 Electrochemical tests

Electrochemical behavior of received Al alloys was assessed under naturally aerated conditions using a Gamry series G 300™ Potentiostat/Galvanostat/ZRA controlled by a personal computer. The corrosion properties of the surface films were studied in 1% (w/v) NaCl aqueous solution at 23±1 °C in a closed Gamry Paracell™. The dilute electrolyte concentration was selected to avoid rapid destruction of oxide films due to aggressive nature of chloride ions. It would allow a more detailed study of mechanisms involved in corrosion protection offered by oxide thin film systems [163]. The setup consisted of Al-alloy substrate as working electrode, graphite plate as counter electrode, and bridge tube containing Ag/AgCl reference electrode. The working volume of corrosive solution was kept at 250 ml and exposed areas for working and counter electrodes were 1 cm^2. Specimens (working electrode) were prepared by gradually grinding with 180-, 360-, 600-, 800- and finally 1200- grit papers in succession. The surface of the specimens was then polished with 3 µm diamond suspension using suitable cloth to give it a mirror like finishing followed by cleaning with deionized water, degreasing with ethanol and drying in air. Different corrosion studies were performed by

means of open circuit potential (OCP) followed by Electrochemical Impedance Spectroscopy (EIS) for different periods of immersion up to 78 h. The electrochemical measurements (OCP, EIS) were taken after every 0.5, 1.5, 6.0, 13, 19, 26, 32, 39, 45, 55, 64, 78 hours. Potentiodynamic (PD) measurements were carried out only for single time i.e. 80 hours of immersion. EIS was conducted by sweeping the frequency from 105 to 102 Hz at 10 mV AC amplitude. PD curves were recorded in corrosive solution starting from free potential and moving the potential from cathodic to anodic direction i.e. from -2.0 volts and ended at 1.5 volts at a scan rate of 0.5 mV/s. Electrochemical tests were duplicated to ensure the repeatability.

6.3 Results and Discussion

6.3.1 Mechanical properties

It has been reported previously by Vo et al. [162] and De Luca et. al. [164] that partial substitution of Sc in Al-Sc alloys with Si, Zr, and Er (designated in this study as BM) significantly reduces the cost yet maintaining high temperature creep resistance. This is due to the formation of coherent nanoprecipitates with core/double-shell structure because of sequential precipitation pertaining to different diffusivities of alloying elements. Consequently, BM-X alloys, with microadditions of V, Nb, or Ta, are reported to have high ambient-temperature strength and elevated temperature creep resistance than BM [16], [134]. Hence, the objective of this section is to compare mechanical properties of BM-X alloys.

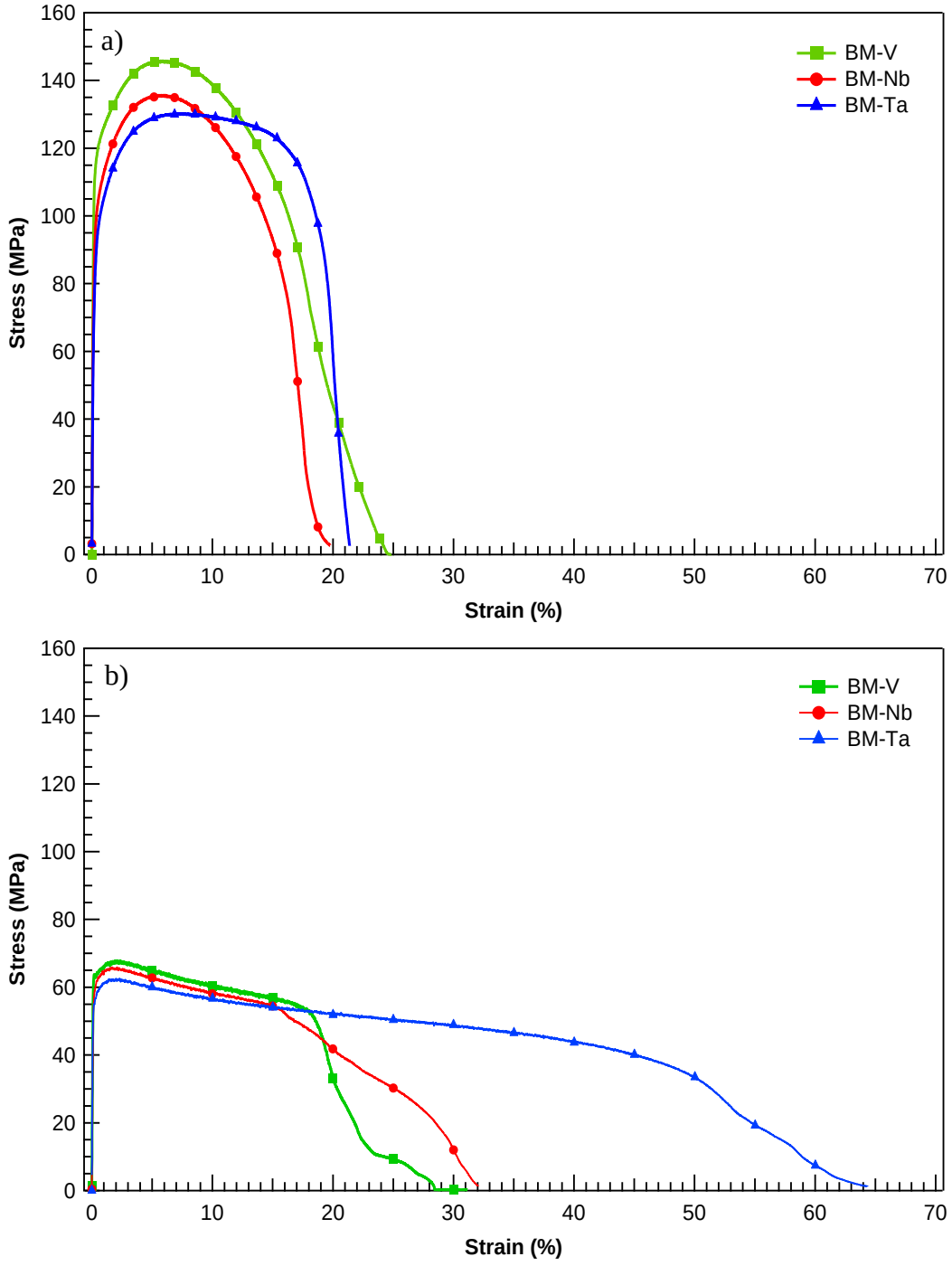

Figure 45 Stress-strain curves at a constant strain rate of $1x10^{-3}$ s^{-1} at a) Room temperature and b) 200 °C. BM-V has highest strength at both conditions, however, the difference of strength at elevated temperature is quite small.

Figure 45 Stress-strain curves at a constant strain rate of $1x10^{-3}$ s^{-1} at a) Room temperature and b) 200 °C. BM-V has highest strength at both conditions, however, the difference of strength at elevated temperature is quite small.

Figure 45a shows room temperature tensile test results at $1x10^{-3}$ s^{-1} strain rate. The order of yield and tensile strengths is that BM-V > BM-Nb > BM-Ta, whereas all BM-X alloys have % elongations in the range of 19 – 25 % at room temperature. Figure 45b compares high temperatures tensile properties of BM-X alloys at 200 °C and $1x10^{-3}$ s^{-1} strain rate. Similar trend can be observed in terms of strengths, as seen at room temperature but with narrow differences. Table 10 display yield strength and % drop strength of BM-X alloys. Percent drop in strength from room temperature to elevated temperature is an important metric to evaluate the high temperature performance of these alloys. BM-V has highest yield strength of 115.4 MPa at room temperature, however the drop by 45.5 % at 200 °C is also highest compared to BM-Nb and BM-Ta. According to this criteria BM-Ta with only 33.3% drop in yield strength has shown highest tendency to maintain strength at elevated temperature. Therefore, Ta- as well as Nb- containing alloys have more effective high temperature precipitation strengthening than V-containing alloy. This is in agreement with the characterization results published by Erdeniz et al. [134] which show that Ta- and Nb- containing alloys have improved precipitate coarsening resistance than V-containing alloy at 400 °C.

Table 10 Summary of yield strength values for Al-Er-Sc-Zr-Si-X alloys, obtained from stress-strain generated at ambient temperature and 200 °C using constant strain rate of 1 x 10-3 s^{-1}.

Alloy / Properties	Yield Strength (MPa)		Drop in strength (%)
Temperature (°C)	**RT**	**200**	--
BM-V	115.4	62.9	45.5
BM-Nb	96.7	59.9	38.1
BM-Ta	84.8	56.6	33.3

6.3.2 Open circuit potential

The variations in the OCP vs. time usually provide information about redox reactions occurring on the surface, and properties and behavior of the resulting oxide/passive layer formed at the metal/electrolyte interface. Generally, in oxygenated and neutral medium, Al oxidation process is two-sided: on one side of oxide layer, oxidation reaction occurs between corrosive environment and metal surface dividing the two solids i.e. Al and Al oxide layer; while on outer side solid Al oxide layer remains in contact with corrosive medium. The formed passive layer dissolves extra stoichiometric Al, water and oxygen converting into two-sided non-stoichiometric phase. The thickness of the Al film increases due to the flux of cations and anions. The resulting oxide layer is composed of inner crystalline adherent, compact, and stable, whereas outer porous and less stable layer [165]. For dilute Al alloys, the growth mechanism of oxide film can be considered as

growth on the pure Al as in both cases the films are comprised primarily of amorphous alumina [166].

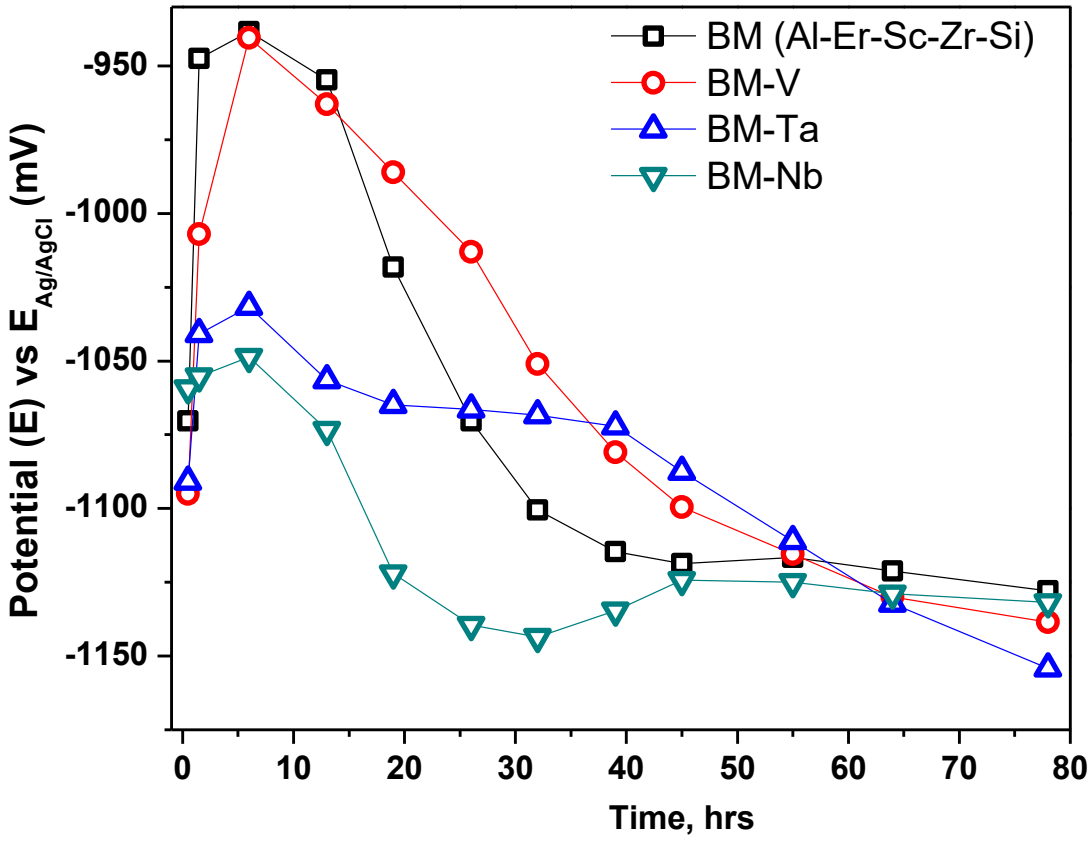

Figure 46 Variations in OCPs vs. Time for Al-Er-Sc-Zr-Si (BM) and BM alloys with V, Ta and Nb during 80 hours of immersion in 1 wt. % NaCl aqueous solution.

A set of OCP transient vs. time plot for BM, BM-V, BM-Nb, and BM-Ta alloys obtained after immersing freshly polished specimens are presented in Figure 46. In general, three main regions were observed in the OCP plots: (a) steady increase in potential up to 13 hr of immersion, (b) decaying potential up to 45 hr of immersion, and (c) steady-state potential up to 78 hr. From the OCP plots, the initial potentials of BM and other compositions show similar values around ~-1080 mV ±15 mV, after that BM and BM-V

potential shifts steeply upward. It can be seen that after 13 hr of immersion BM and BM-V alloy exhibited potential of around ~-954 mV and ~-963 mV respectively. In comparison, after 13 hr the potentials of BM-Ta and BM-Nb did not show sharp rise in the beginning and remain at the value of ~-1056 mV and ~-1073 mV respectively. For Al, it is already established that formation of resistive oxide film increases the potential of Al surface from its theoretical potential ~-1855 mV to around ~-755 mV vs. Ag/AgCl in sodium chloride neutral aqueous solution [167]. The initial free potentials of BM and alloys indicate a difference of ~-250 mV (more negative) from the characteristic potential (~-755 mV) of Al surface covered with oxide in NaCl aqueous solution. This difference in the shifting of OCP indicates the effect of added element on electrochemical properties of BM and alloys. It was also reported that addition of minor amounts of other elements in pure Al can shift the OCP into the negative direction. For instance, alloying with gallium in a small amount can shifts the free potential of pure Al towards negative direction as much as ~850 mV [168]. The electrochemical behavior of peak aged BM and alloys can be attributed to micro-precipitates accumulated at the grain boundaries along with nanoprecipitates enriched Al matrix [16], [134], [164] which electrochemically activates the Al surface [165]. In main matrix or at grain boundaries these precipitates wet or create metallic contact between the metal and added elements enriched phases and provide depassivation of the overlying film at such locations to some extent.

During first region of OCP plot, BM and BM-V shows sharp rise in the potential (positive direction) indicating the exposed cathodic sites which can easily shift polarization under anodic control. With the addition of Nb and Ta this behavior seems to

be suppressive which is an indication of higher electrochemical activity of Nb and Ta containing precipitates at the metal-oxide interface. This behavior seems to be agreed with the fact that in the presence of protective oxide layer including covering the cathodic sites, the surface can easily be polarized towards the direction of negative potential under cathodic control. This behavior is more pronounced during second region of OCP plot, where potential is significantly becoming negative under cathodic control indicating the coverage of cathodic sites present on the surface. The OCP of BM-Nb shows a minimum of ~-1145 mV potential after 32 hr of immersion indicating the higher activity of BM alloys with the inclusion of Nb. Nb and Ta has very high reactivity towards almost all salt solution and acids generating amorphous oxide films which places them at the nobler end of electromotive series [169]. It was also reported previously that OCP transient in the negative direction can be attributed to electrochemical activation of a surface layer of metal which in turn causes the poor filiform corrosion susceptibility [170]. The potential of BM showed a rapid decline moving towards negative direction and became almost similar to BM-Nb i.e. ~-1120 mV after 45 hr. From this behavior it can be inferred that in case of BM, in first region of OCP plots, anodically control reactions (positively potential) change to cathodically control reaction (negatively potential) in second region of OCP plots. Compare to BM, BM-V exhibited a delayed drop in the potential towards negative direction and after 45 hr it showed ~-1098 mV similar to BM-Ta ~-1090 mV. However, in second region, compared to other alloys, BM-Ta showed a gradual decline in the potential up to 45 hr of immersion. In third region of OCP plots, the potential transients seems to be stable and can be thought at a value corresponding to the pitting potential of

bulk Al matrix which usually can be found after anodic dissolution of active layer in polarization curves (potential vs current) [170]. In third region, contrary to BM and alloys, BM-Ta showed a continuous decline in the potential and ended at ~-1155 mV. This behavior can be attributed to the delayed activity shown by Ta precipitates compared to Nb precipitates. Also, in third region of OCP plots, BM, BM-V and BM-Nb showed virtually stable potential up to 78 hr and ends at a similar value of potential around ~-1130 mV ±5 mV. This stable potential cannot be classified as passivity but instead as stationary activity [171].

6.3.3 Electrochemical impedance spectroscopy

In order to obtain information about characteristics of surface layer formed on BM and alloys, EIS tests were carried out in 1 wt. % NaCl over different period of immersion. EIS is a useful and non-destructive method which provide qualitative and quantitative information about the processes occurring on working electrode surface. The nature of the passive oxide layer on Al effects the corrosion rate and nature of corrosive attack. Impedance spectra have been presented as Bode magnitude, Bode phase plots and Nyquist plots in Figure 47 (a-b), Figure 48 (a-b) and Figure 49 (a-b) for BM and BM alloys obtained after 6 and 78 hr of immersion respectively. The EIS plots obtained after 0.5 and 1.5 hr (not shown here and modeled) for BM alloys (except BM) exhibited large data scattering indicating large current fluctuations due a surface film with large number of discontinuities at the beginning of immersion. The equivalent circuits used to model the EIS spectra for BM and alloys, and values obtained after fitting the spectra are presented in Figure 50 (a-c), and Table 11 respectively.

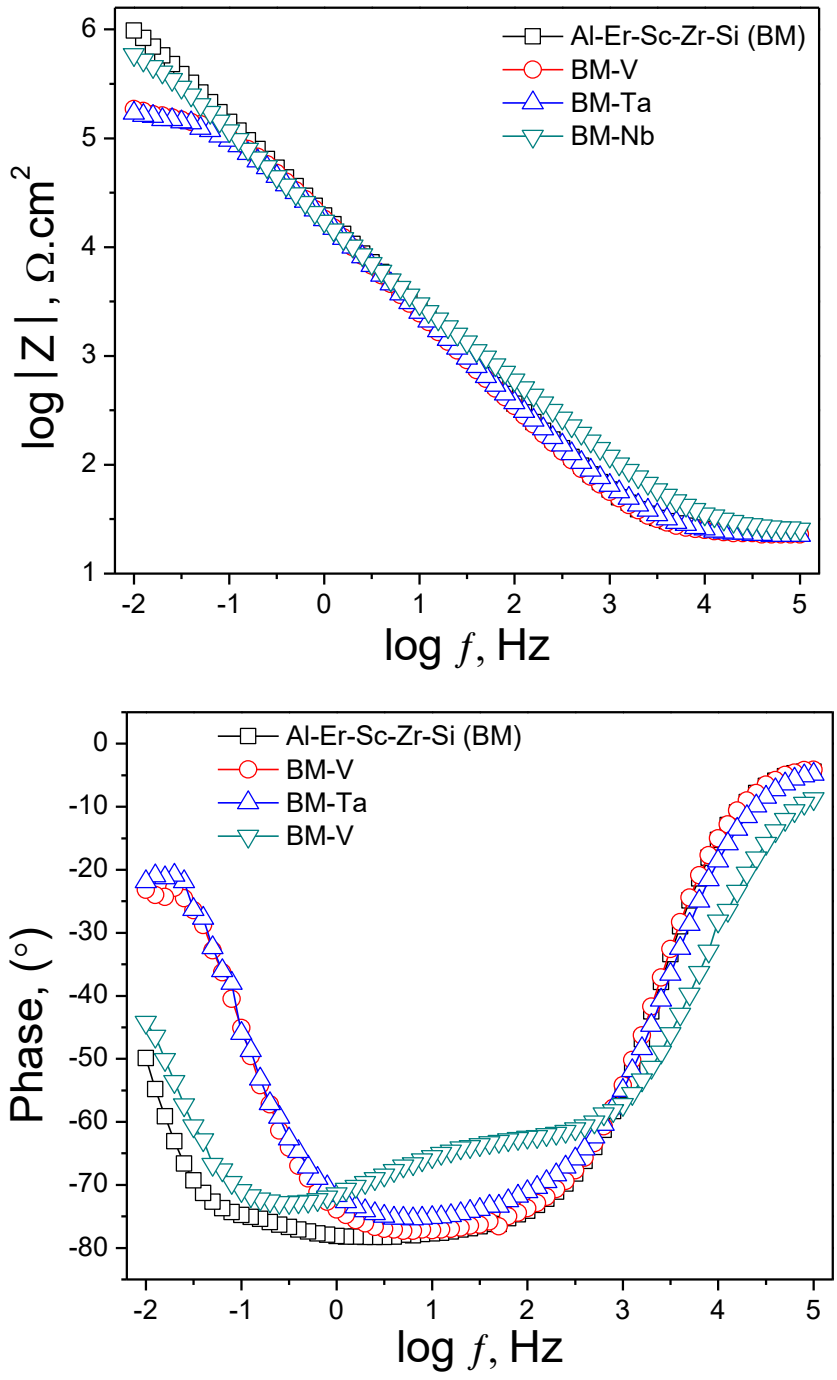

Figure 47 Bode plots after 6 hr of immersion in 1 wt. % NaCl aqueous solution of Al-Er-Sc-Zr-Si (BM) and BM alloys with V, Ta and Nb (a) impedance vs freq. and (b) phase angle vs. freq.

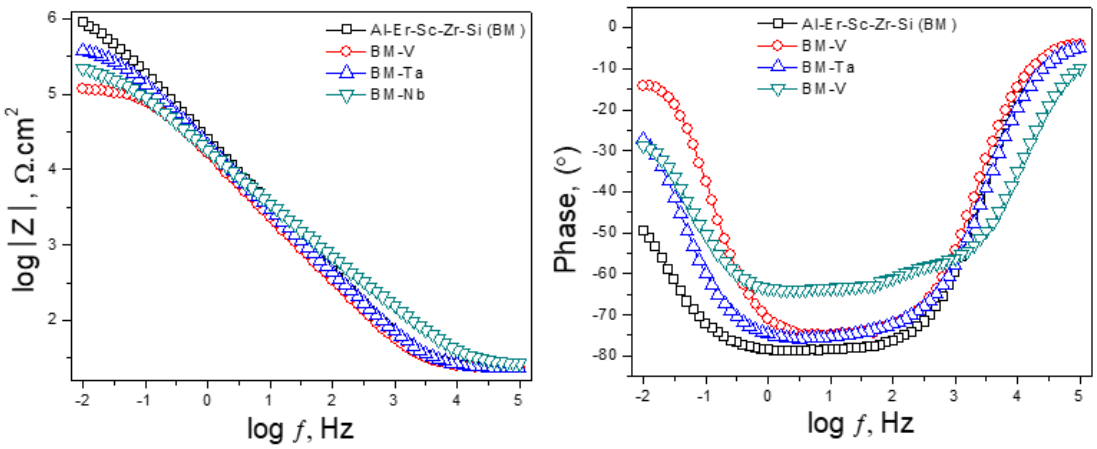

Figure 48 Bode plots after 78 hr of immersion in 1 wt. % NaCl aqueous solution of Al-Er-Sc-Zr-Si (BM) and BM alloys with V, Ta and Nb (a) impedance vs freq. and (b) phase angle vs. freq.

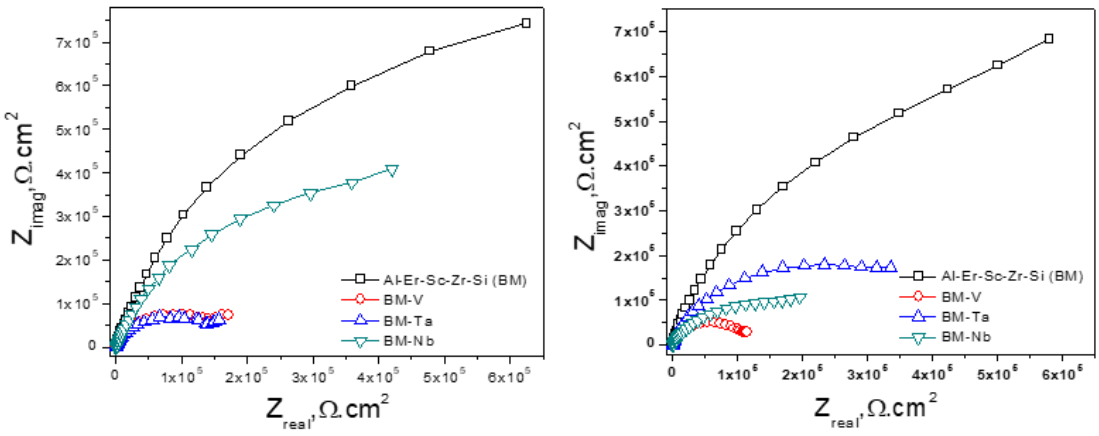

Figure 49 Nyquist plots after (a) 6 hr and (b) 78 hr of immersion in 1 wt. % NaCl aqueous solution of Al-Er-Sc-Zr-Si (BM) and BM alloys with V, Ta and Nb

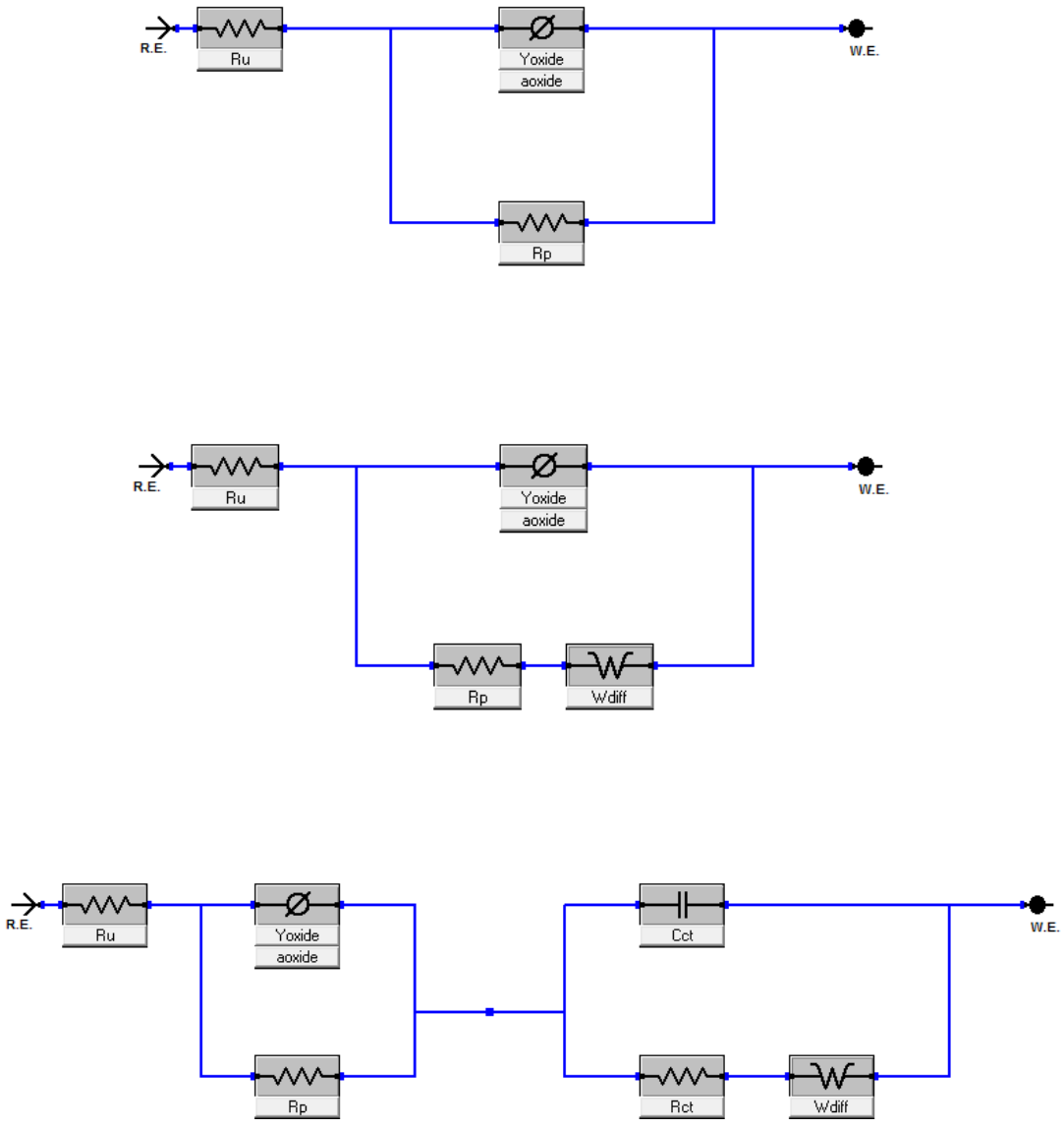

Figure 50 Proposed equivalent circuits to fit EIS plots obtained during 78 hr of immersion in 1 wt. % NaCl aqueous solution (a) BM upto 13 hr, (b) BM upto 78 hr (c) BM-V, BM-Ta, BM-Nb for all period of immersion.

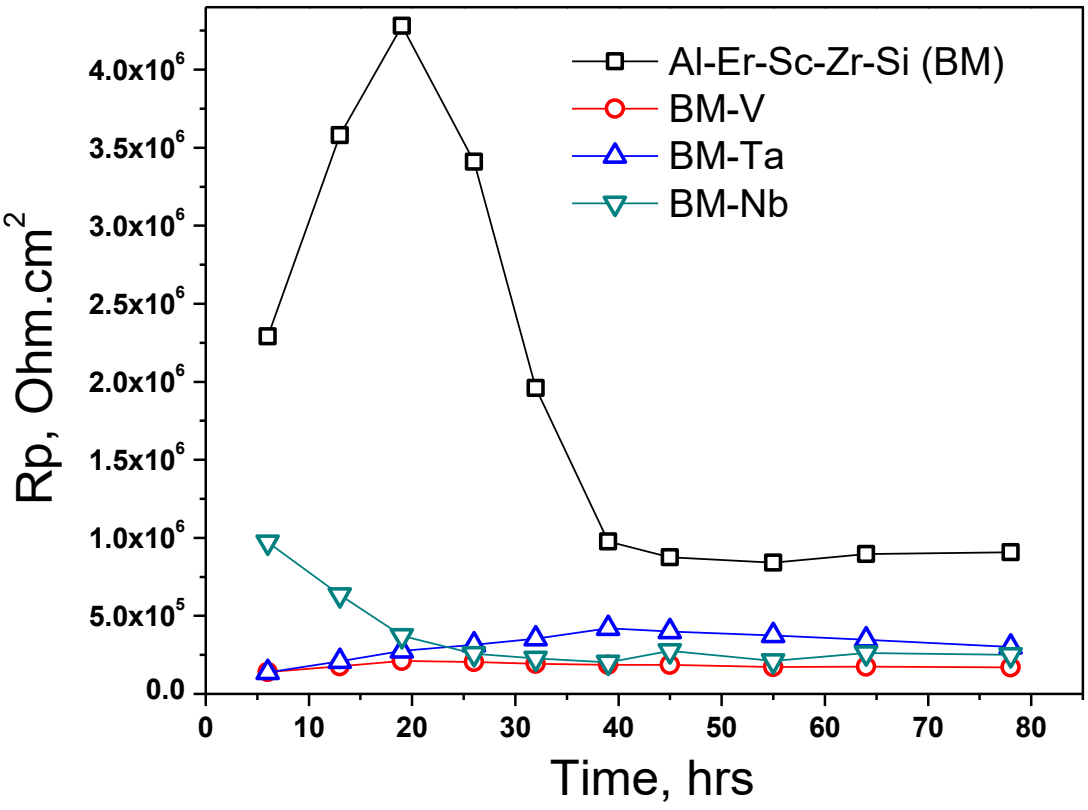

Figure 51 Variations in polarization resistance, Rp (EIS) vs. Time for Al-Er-Sc-Zr-Si (BM) and BM alloys with V, Ta and Nb during 80 hours of immersion in 1 wt. % NaCl aqueous solution.

Table 11 Electrochemical parameters obtained by fitting EIS data with equivalent circuit models

Time (hr)	$R_{p=} R_{oxide}+\|Z_{diff}\|$	$R_p=R_{oxide}+R_{ct}+\|Z_{diff}\|$			Capacitance$_{ox}$ ($C_{overall}$) F/cm^2 ×10^{-05}				Capacitance$_{ct}$ (C_{ct}) F/ cm^2 ×10^{-05}			
	Ohm.cm^2 ×10^{05}											
Sample type	BM	BM-V	BM-Ta	BM-Nb	BM	BM-V	BM-Ta	BM-Nb	BM	BM-V	BM-Ta	BM-Nb
0.5	-	-	-	-	-	-	-	-	-	-	-	-
1.5	-	-	-	-	-	-	-	-	-	-	-	-
06	22.9*	1.41	1.39	9.72	0.747	1.72	1.17	0.933	-	4.59	1.87	0.155
13	35.8*	1.76	2.08	6.35	0.644	1.77	1.24	0.843	-	0.894	1.42	0.101
19	42.8	2.11	2.76	3.73	0.61	1.20	1.18	0.794	-	1.69	1.56	0.107
26	34.1	2.04	3.15	2.57	0.593	1.17	1.17	0.807	-	1.88	1.59	0.097
32	19.6	1.92	3.53	2.27	0.593	1.17	1.15	0.725	-	2.30	1.66	0.074
39	9.77	1.87	4.21	2.02	0.598	1.17	0.866	0.793	-	2.25	1.40	0.087
45	8.76	1.86	4.00	2.75	0.605	1.18	0.682	0.717	-	2.25	7.27	0.07
55	8.42	1.72	3.74	2.11	0.61	1.22	0.699	0.814	-	1.91	5.90	0.077
64	8.96	1.75	3.47	2.61	0.607	1.21	0.707	0.010	-	2.21	4.92	0.078
78	9.08	1.70	3.01	2.50	0.604	1.27	0.752	0.796	-	1.91	3.46	0.084

The EIS spectra obtained for BM substrate were modelled using simplest model i.e. parallel combination of one time constant (CPEoverall) and resister (Rp) up to 13 hr of immersion and with an inclusion of extra impedance using Warburg element up to 78 hr. The impedance of the Warburg element (|Z_diff |) was calculated using the equation; |Z_diff |=√2 σ/ω^(1/2), Where σ is Warburg constant and can be calculated using magnitude of the admittance Y_o at ω=1 rad/sec (~0.16 Hz) using equation; σ=1/(√2×Y_o). The Y_o value can be obtained by fitting the circuit which includes Warburg impedance. The units of σ and Y_o are ohm·sec-1/2 and siemens·sec1/2 respectively. The selection of suitable equivalent electrical circuit was made on the basis of shape of Bode phase and Nyquist profiles and accuracy of fitting for different combination of circuits as judged by the minimum error distribution vs. frequency (χ2 values). It is also important to mention that the proposed circuit model should account the kinetics of the involved electrochemical processes which includes, Al dissolution, oxygen reduction (ORR) and hydrogen evolution reaction (HER), diffusion of species from bulk electrolyte to surface and vice versa. Sometimes, the proposed equivalent circuit suggests poor fitting due to consideration of only ORR contribution as the experiments are carried out at Ecorr [171]. For instance, in case of BM, initially the overall response of the system was due to the superposition of combined responses related to oxide layer, possible defects and metal-oxide interface and the elements (Rp-overall) encompass all the information related within them. Generally, each element in the model circuit associates with each of the processes occurring on the surface. In addition to it, range of frequencies is related to the different processes. Specifically, for Al, it is assumed that impedances spectrum can be divided into

three region responses associated with localized attack at higher frequency range, surface layer characteristics at slightly lower frequencies, then slowest process like transport of Al+3 ions across oxide layer at low frequency range [171]. The phase angle after 6 hr of immersion for BM (Figure 48b) indicate dominant capacitive behavior (~-60°) starts at high frequency (~0.78 kHz) exhibited a frequency independent plateau region with a minimum of (~-78°) and continue to low frequency. After a frequency of ~0.6 Hz, the phase angle rises sharply and ended (@0.01 Hz) with a slight dominant capacitive behavior (~-50°). The evolution of phase angle would agree with the fact that BM produced compact and stable protective surface layer. In addition, a dominant capacitive behavior at low frequency (characteristics of metal surface) also indicate the presence of well adherent inner crystalline layer. The presence of incomplete semicircle and highly capacitive loop in Nyquist profile (Figure 49a) also corroborate with the phase angle behavior. Further, after 13 hr immersion of BM, Warburg impedance element (semi-infinite linear diffusion) in model circuit Figure 50b indicates the hint of diffusion restricted process attributed to transport of cations and anions across oxide layer. This was also confirmed in the Nyquist plot (Figure 49b) where the arc-shaped termination of such ill-defined and unfinished segment in Nyquist plot as well appeared in phase angle profile at very low frequency i.e. @ 0.01Hz approaching proximity to 45°.

For BM alloys, the selected equivalent electrical circuit model enables the evaluation separately of the contribution of each process. In this circuit model, the loop of Rp-overall has been divided into two loops i.e. Rp-oxide and Rct resulting in the circuit model shown in Figure 50c. In particular, the former is associated with the oxide layer to

take account of pores or defects exist in this layer and the later accounts for metal-oxide interface. A double layer capacitance (Cct) (ideal capacitor) was used instead of a constant phase element (CPEct) as during circuit fitting the coefficient "n" of CPEct came up with a value of 1, recovering a perfect capacitor. Previous studies showed that using CPEct instead of Cct indicates that properties of the double-layer are heterogeneous among the studied Al alloy surface [172]. The proposed equivalent electrical circuit for BM alloys also describes the mass transfer control Warburg impedance. The phase angle behavior of BM-Nb after 6 hr immersion exhibited similar profile shape as of BM except the lesser degree of capacitive behavior. The phase angle after 6 hr of immersion for BM-Nb (Figure 48b) indicate dominant capacitive behavior (~-60°) starts at higher frequency (~0.78 kHz) and exhibited a frequency independent plateau region with a minimum of (~-65°) indicating less stable and protective layer compare to BM. The slight hump at intermediate frequency range (~0.16 kHz-~2.0 Hz) also confirms the diffusive nature of the outer layer. After a frequency of ~0.6 Hz, the phase angle profile rises gradually instead of sharp rise as observed in BM and ended (@0.01 Hz) with a dominant diffusive behavior (~-43°) indicating porous inner layer compare to BM. Also, this behavior can be observed from incomplete Nyquist plots for BM-Nb which presents an initial well-defined arc followed by a very small branch which could be assigned to an unfinished diffusion tail. The phase angle behavior of BM-Ta and BM-V exhibited very much same trend. The phase angle approaching to zero at lower frequency ranges indicates a defective and loosely adherent inner layer. The phase profile also hinted a semi-infinite linear diffusion at 0.01 Hz.

The Bode impedance plots (log |Z| vs Frequency) after 6 hr immersion shown in Figure 47a, exhibited two distinct regions for BM, whereas three regions were observed for BM-Nb, BM-V and BM-Ta. The third region for BM-Nb was ill-defined. The higher frequency region (~1-100 kHz) was due to the response of electrolyte resistance, whereas the broad low and middle region with slop of ~-0.9 displayed response of film capacitance. In addition, this region also depicts the extent of localized corrosion as even small number of pits produces large changes in this region [173]. In this region, the Bode impedance plots for BM, BM-V and BM-Ta displayed a slop between -0.82 to -0.9. For BM-Nb, the slop was around ~-0.7 may be attributed to the activity by the Nb containing micro/nano precipitates also indicated by OCP plot. The third region in the low frequency range, indicates a diffusion-controlled process within the oxide film at metal/film is responsible for the EIS spectra observed [174]. This behavior is more pronounced for BM-V and BM-Ta compare to BM-Nb also indicating diffusion of reactants and/or products to the metal/film interface [173].

Proceeding further, Figure 48 (a-b) shows the Bode plots after 78 hr of immersion. The phase angle profiles exhibited less degree of capacitive behavior (except BM-Ta) at lower frequency region compare to shorter period of immersion indicating the improved surface film near the. For BM-Ta, the capacitive behavior at ~0.3Hz shifting from ~-65° to ~-75° indicating a well-established inner surface layer. For BM-Ta, contrary to 6 hr of immersion, from Bode impedance diagram (Figure 48a), it can be observed that longer period of exposure is characterized by the presence of a rise in the value of |Z| at lowest frequencies. Also, in Table 11, it can be confirmed that in passing from 6 hr to 78 hr of

exposure, the values of oxide capacitance (Cox) for BM-Ta are decreasing from 1.77 to 0.752 F/cm2 ×10-05, this fall can be related to increase in the thickness of the layer covering the alloy surface. This evolution agrees with the polarization resistance (Rp) which is shown here as sum of all the impedance provided by oxide layer (Roxide), charge transfer resistance offered by metal surface (Rct) and impedance arise due to diffusion at metal/film interface the (|Zdiff|). The Rp vs. Time plot (Figure 51) exhibited that Rp for BM-Ta is continuously increasing i.e. from 1.39 to 4.21×1005 Ohm.cm2 up to 39 hr of exposure and after that exhibited a slight decline. On the other hand, the Cct values largely increased from 1.87 to 3.46 ×10-05 F/cm2, it can be related to the increase in local dielectric effect around the precipitates due higher and effective increase in the surface area of the matrix surrounding the precipitates. This trend of Cct was not observed in case of BM-Nb and BM-V as the Cct was decreasing with exposure time indicating reduction of the area of contact between the precipitates and the matrix [171]. The apparent decrease in the Rp values of BM and BM-Nb with increasing exposure time can be related to the increase in the activity necessary to produce the increase in the thickness of layer. This activity causes the creation of image charges of the same magnitude but of opposite sign at the oxide/metal interface, sufficient to accelerate Al^{+3} through the oxide to the film/solution interphase generating an electrical field which could be responsible for the reduction observed for Rp during this period of time [171], [175]. For BM-V, it can be observed that values of Rp remains lower than the other alloys for the all the periods of immersion. In principle it can be inferred from the electrochemical results that zones near to the nano/micro-precipitates for BM-Nb exhibited high activity in the beginning

compare to BM and BM-V comparison with BM-Ta which showed a relatively delayed activity alter at longer period of immersion.

6.3.4 Potentiodynamic polarization

The polarization curves of BM and BM alloys are presented in Figure 52 and Figure 53. The polarization curves can be characterized by a number of corrosion potentials which is an indication of an unstable passive system. Similar corrosion behaviors have been reported for chromium and chromium alloys in acidic and acidic chloride solutions [33]. The OCP values (Figure 46) for BM and BM alloys after 80 hr exposure are in a range of ~-1125 mV to ~-1150 mV. While these potentials in potentiodynamic curves correspond to the active zones indicating that corrosion potential of the system is situated way below the pitting nucleation potential. This finding indicates that no crystallographic pits will formed during entire period of immersion except at higher potentials during transient [171]. In the presence of aggressive anions such as chloride, Cl^- the protective oxide layers become unstable and deteriorates locally resulting film breakdown and pitting. Natishan et al. reviewed a number of theories and mechanisms on initiation of pitting corrosion and focused on interaction of Cl^- with the protective oxide film on pure aluminum [176]. The observations for Cl^- interactions with Al- might be applicable to micro-alloyed added aluminum. As mentioned previously, the initiation of pitting corrosion can be classified into three general groups 1) ion penetration of the oxide, 2) ion displacement leading to oxide thinning, and 3) breakdown and repair of oxides [176]–[178]. It may be inferred from prevailing mechanism of pitting that in the presence of the active surfaces resulting improved activity may lead to multiple corrosion

potentials on PD curve. Due to improved thermodynamic activity of Al as a result of active micro/nano precipices, promotes the formation and reparation of aluminum oxy-hydroxides multiple times until the potential is high enough leading to initiation of pitting. A typical PD curve for BM (Figure 53) shows only one corrosion potential i.e. E3~-1220, and there exist three small troughs before and after it i.e. E1~-1350, E2~-1250 and Epit ~-790 mV respectively. In literature, the pitting incubation potential of aluminum in neutral chloride solution is a value around ~-790 mV vs EAg/AgCl [170], [179] and values above than this were observed for BM and BM-alloys. Compared to BM and BM-Nb, BM-Ta and BM-V were characterized by a positive shift in the corrosion potential indicating reduce electrochemical activation. BM-V also exhibited high corrosion current relative to the other BM alloys. The corrosion potential of BM-Ta also seems to be more positive than BM and BM-Nb, but less positive than BM-V. These results also corroborate with the OCP trends where BM-Ta showed delayed activity compare to BM and other BM alloys. BM-Nb also exhibited highly negative corrosion potential and tendency for discrete oxidation peaks which shows that BM-Nb surface is more active than the other materials in measured potential range. The highly negative corrosion potential exhibited by the BM-Nb may also be related to the absence of cathodic segregations, which are needed to polarize the matrix to the pitting potential [165]. It is noteworthy that at higher potential, for all alloys anodic part of the polarization curves have strikingly similar profile and did not exhibit any oxidation peaks despite significant difference in the cathodic polarization curves. The pitting potentials for all alloys were also found very much similar i.e. a value around ~-750 mV. The curve for BM-Nb exhibited three well defined corrosion potentials

at E1~-1340, E2~-1170, E3~-990 and pitting potential (Epit) ~-750 mV. The transition anodic-cathodic in the current density between E1-E2 and E2 and E3 can be attributed to the cathodic reactions occurring on the passive surface at a rate greater than the rate of passive dissolution. Moreover, it was also reported that generated metal cations may affect the cathodic depolarisation consequently contributing to the observed effects on the corrosion [180]. The cathodic branch of BM-V also exhibited two small troughs i.e. at potential E1~-1450, E2~-1120 before the corrosion potential i.e. E3~-740. The anodic branch of the curve did not exhibit a discrete pitting potential as observed in other cases. Considering the pitting potential of other alloys, it seems that for BM-V the pitting has been occurred at corrosion potential E3~~-740. It can also be inferred from these results that V containing nano/micro precipitates are not enough active to promote the thermodynamic activity of matrix. Similarly, for BM-Ta, the PD curve only exhibit one distinct peak E1~-1250 mV below the corrosion potential E2~-790 mV. The Epit~-1250 mV for BM-Ta was similar to the other alloys. Usually, pits do not initiate or propagate below the protection potential and more negative Epit indicates an easier breakdown and initiation of pits. The pitting potential of the four alloys shows that varying the alloying elements do not affect the pitting potential and the alloys are equally susceptible to pitting corrosion.

The additions of trace amount of group IIIA-VA elements to Al forms the basis of sacrificial aluminum anodes for cathodic protection in chloride solutions. The cited literature confirms that presence of trace amount of Si, Ge, Ti, Zr, and Sn significantly lowered the ionic resistance of the surface film which result in a displacement of corrosion

potential in the active direction [181], [182]. However, the mechanism by which trace amount of group IIIB, IVB, VB and rare earth elements activates the aluminum surface is needed to be explored more. A detailed investigation of Al-traces alloys with varying the individual element content will be reported in the near future. However, from the previous literature, the electrochemical surface activation can be explained in terms of three main phenomenon i.e. enrichment of the surface by these added trace elements, wetting enriched trace elements particles and the aluminum metal, and de-passivation of the overlying oxide at such locations [165], [170]. Although, alloys of Al with individual element at higher concertation like Al-Ta, Al-Sc, Al-Zr etc has reported the presence of these elements in the oxide layer consequently effecting the corrosion properties. These issues will also require attention for the case of trace elements. Moreover, the role of chloride in activation in neutral solutions should be emphasize for future studies.

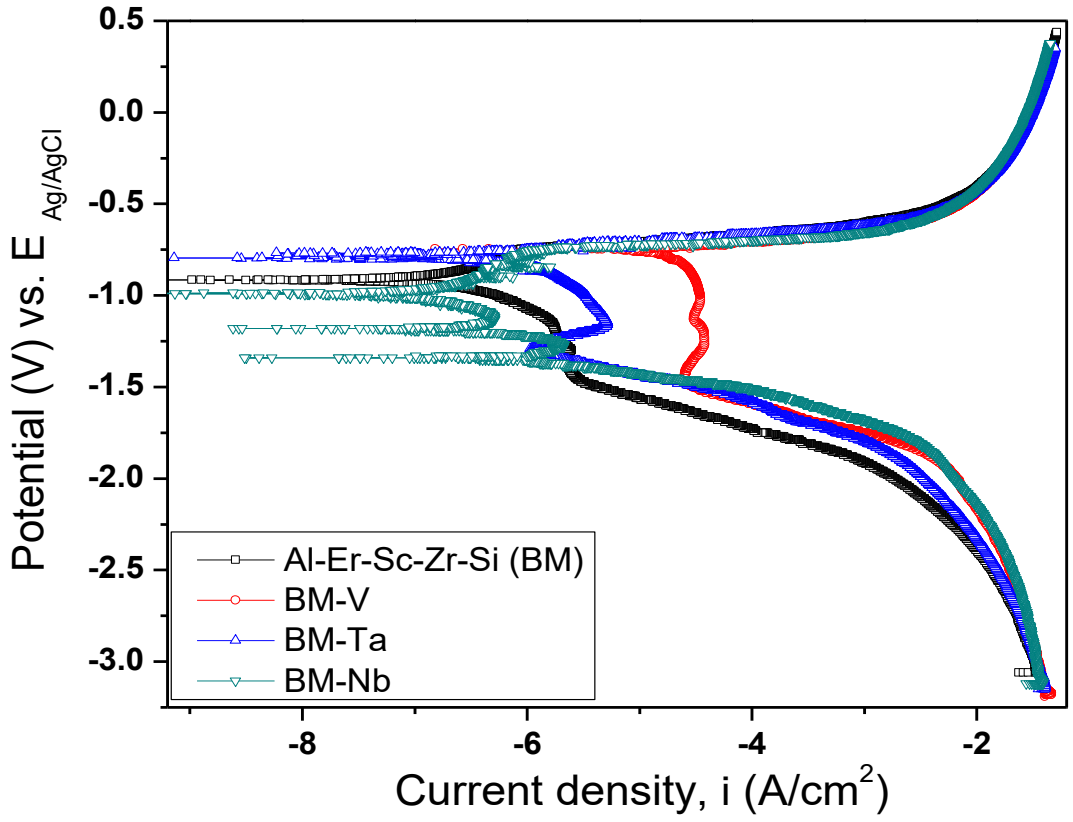

Figure 52 Potentiodynamic for Al-Er-Sc-Zr-Si (BM) and BM alloys with V, Ta and Nb after 80 hours of immersion in 1 wt. % NaCl aqueous solution.

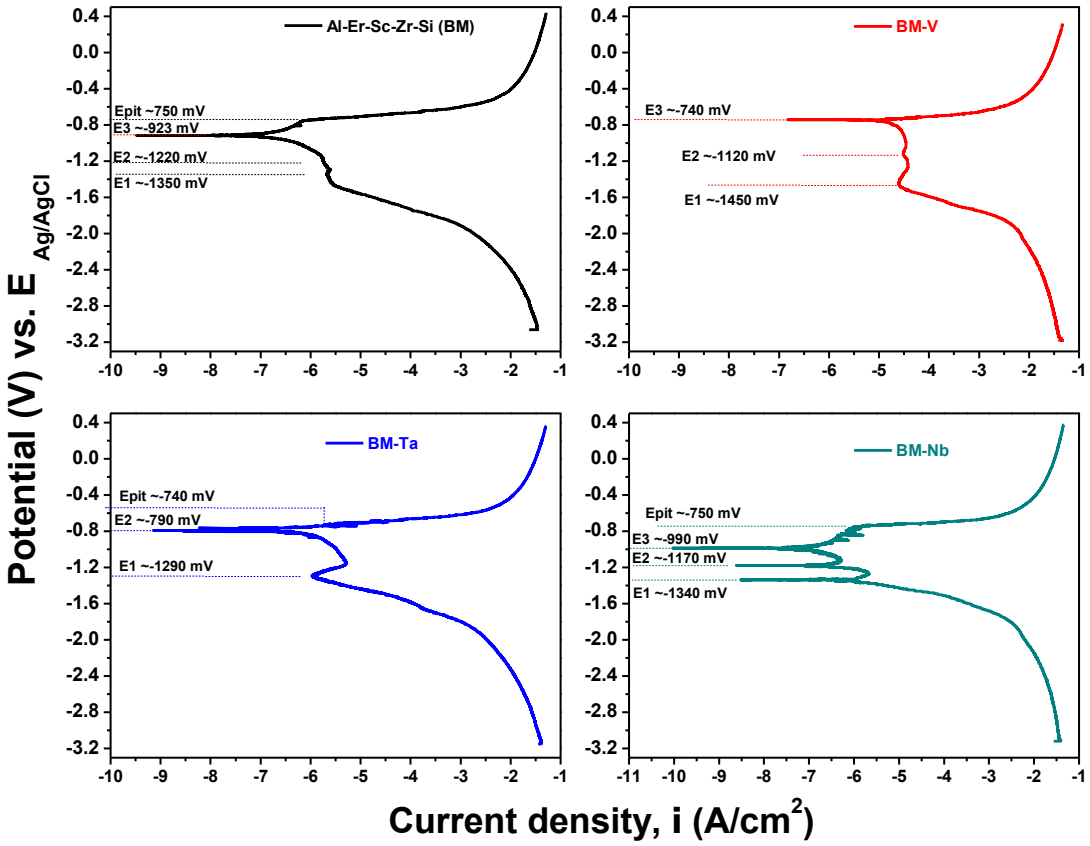

Figure 53 Potentiodynamic discrete curves for (Left)Al-Er-Sc-Zr-Si (BM), BM-Ta and (Right) BM-V, BM-Nb after 80 hours of immersion in 1 wt. % NaCl aqueous solution.

6.3.5 Surface analysis

Photomicrographs showing pitting morphology on BM and BM alloys after the PD experiments are presented in Figure 54 (a-i). In general, for all BM alloys, the surfaces with locally attacked portions exhibited irregular shaped pits as well as some small and hemispherical pits on the grain boundaries can be observed. The pitting morphology of the studied BM alloys was unaffected with changing the composition of the nanoprecipitates. As reported in earlier that Al_3(Er,Sc,Zr,V,Ta,Nb) nanoprecipitates on surface are coherent with the matrix having lesser flaws and discontinuities at the interface compare to large size precipitates. It was also reported that presence of large size of precipitate decreased the pitting potential. It can be seen that the pitting potentials of all BM alloys have similar values suggesting similar size precipitates [156], [183]. However, in general for all BM alloys the pits were found all over the surfaces as can be seen in Figure 54f. The breakdown of the oxide layer around the pits can be seen in the Figure 54g where pits are covered by white gelatinous product of the $Al(OH)_3$ (Corrosion Chimney) which solidifies upon drying. The $Al(OH)_3$ pumped buy the pits and dries eventually and cracks in form of mud-cracking. From these results, it be inferred that nanoprecipitates actively contribute to the pitting corrosion by providing active sides for intensive pitting which is a similar behavior in case of alloys containing larger number of intermetallics due to inherent discontinuities at precipitate/oxide/electrolyte interface [183], [184].

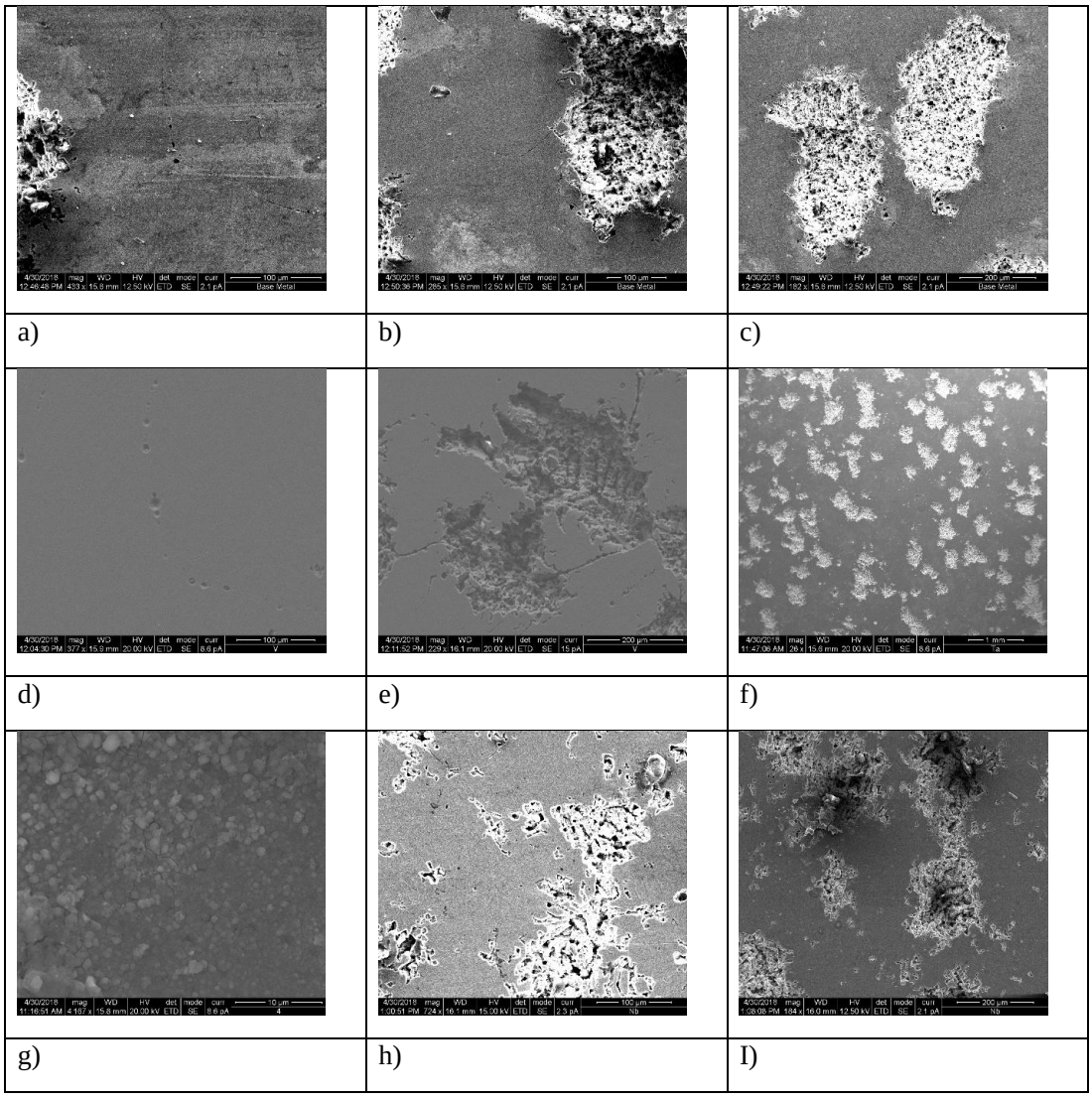

Figure 54 Scanning electron micrograph showing pitting formation after the potentiodynamic polarization experiments for 80 hr exposure in an aqueous solution containing 1% (w/v) NaCl (a-c) BM, (d-e) BM-V, (f-g) BM-Ta, and (h-i) BM-Nb.

6.4 Conclusions

In this study we investigated the mechanical and electrochemical response of high temperature Al-0.07Zr-0.02Sc-0.005Er-0.06Si (at. %) with micro-additions of Group 5 transition elements (V, Nb, or Ta) added individually. Mechanical properties were evaluated at room temperature and 200 °C using tensile tests. V-containing alloy showed 20 – 30 MPa higher room temperature yield strength than Nb- and Ta- containing alloys. However, keeping room temperature properties as reference point, there was significant drop in the yield strength at 200 °C for V-containing alloy which indicates that Ta- and Nb- containing alloys have better performance at elevated temperature. This is attributed to improved precipitate coarsening resistance.

Electrochemical characterization shows significant activation Al-Er-Sc-Zr-Si-X alloys, with reference to pure aluminum. The shift in OCP potential towards negative direction indicated the extent of activation which can be correlated with the enrichment of the aluminum surface by these elements which was resulted from precipitation hardening. The decreased resistance of the surface films formed on alloy surface contained Nb, Ta, V individually was also observed. Moreover, the film resistance of BM-Nb was higher compare to BM-Ta and BM-V at the beginning and declined with increased exposure. Contrary to Ta containing alloy, initially the resistance of surface films was lower and increased with exposure time which can be attributed to delayed activity shown by Ta enrichment. Overall and for all periods of exposure, the film resistance of BM was higher and decreasing with increased exposure time indicating a less defective passive layer. The polarization curves also exhibited multiple corrosion potential and oxidation peaks when

the alloy was cathodically scan. This can be attributed to formation of unstable surface films formed on the alloy surface at different potentials. Preliminary findings exhibited that micro-alloy addition of transition elements follow a course of surface activation due to surface enrichment that differs somewhat from that without these transition elements.

Finally, the order of electrochemical activity shown by surfaces in saline media is Al-Er-Sc-Zr-Si-Nb ≈ Al-Er-Sc-Zr-Si-Ta > Al-Er-Sc-Zr-Si > Al-Er-Sc-Zr-Si-V. While, the order of mechanical strength is Al-Er-Sc-Zr-Si-V > Al-Er-Sc-Zr-Si-Nb > Al-Er-Sc-Zr-Si-Ta > Al-Er-Sc-Zr-Si. Current study justifies the addition of Group 5 elements (Nb, Ta, or V) to improve ambient and elevated temperature mechanical properties with slight compromise on corrosion resistance over base alloy (Al-Er-Sc-Zr-Si).

CHAPTER VII

CONCLUSIONS AND FUTURE DIRECTIONS

Aluminum alloys are important structural materials due to their low density which gives them the edge over steels, Ti-, and Ni- based alloys in terms of specific strength. The major downside of these alloys is their limited application at elevated temperature due to the presence of metastable precipitates in most conventional precipitation hardenable aluminum alloys. In this dissertation I selected a recently developed scandium containing aluminum alloy, which is designed for high temperature applications. My aim was to alter the properties, processing, performance of this alloy to optimize room temperature strength, elevated strength/ductility combination, and thermal stabilities (ability to maintain microhardness after subjecting to various temperatures). Through the application of Equal channel angular pressing (ECAP), I was able to modify the structure, refine grain size down to submicron diameter, and tailor the precipitation kinetics and nucleation sites. Major conclusions from this study are as follows:

7.1 Conclusions

1. New aluminum alloy containing micro-additions of rare-earths and transition metals to be used up to 400°C. Strengths up to 16 MPa with 6 % elongation at 400 °C was achieved for aged Al-Er-Sc-Zr-V alloy.
2. Selection of ECAP route: 4Bc as most effective to produce refined grain structure with high angle of misorientation giving combined strength and ductility.

Maximum tensile strength of ~190 MPa: through precipitation hardening followed by grain refinement using ECAP route 4Bc.

3. One significant finding was the ability of supersaturated (homogenized) Al-Er-Sc-Zr-V-Si alloys to dynamically precipitate nanosized trialuminides during room temperature ECAP using route 4Bc. Deformation driven accelerated diffusion led to decomposition of this alloy during ECAP is an important discovery. It will serve as a cost-effective and time-effective processing path to mass produce this alloy with combined effect of precipitation hardening and grain refinement.
4. Thermal stability depends on the processing condition of Al-Er-Sc-Zr-Si-V alloy and shows a trade off with strength. Up to 250 °C with 62 HV (peak-aged followed by ECAP) and up to 400 °C with 52 HV (peak-aged only).
5. Grain growth mechanisms during deformation are controlled by precipitates. 43 % more grain growth in H-ECAP during deformation. In contrast only 13 % more grain growth in PA-ECAP during deformation.
6. Intergranular precipitates (along GBs) restrain grain coarsening and rotation in PA-ECAP. Intragranular precipitates (grain interior) in H-ECAP promotes high strength due to dislocation trapping in grain interior.
7. Order of electrochemical activity shown by surfaces in saline media is Al-Er-Sc-Zr-Si-Nb ≈ Al-Er-Sc-Zr-Si-Ta > Al-Er-Sc-Zr-Si-V > Al-Er-Sc-Zr-Si. However, no significant difference in corrosion properties of all four alloy systems was observed. Nevertheless, these micro-alloyed precipitation hardenable alloys are evaluated to be more active (higher corrosion rate) than pure aluminum.

7.2 Future directions

Results and analysis reported in this dissertation open a path for better processing of precipitation hardenable high temperature Al-Sc alloys through application of severe plastic deformation. Through double-aging heat treatment of Al-Er-Sc-Zr-V-Si we confirmed formation of core-shell precipitates and after ECAP of aged alloy we see that the structure is conserved. However, one of the main questions yet to be answered is whether the precipitates formed during room temperature ECAP in supersaturated alloy are also core-shell? These precipitates are formed deformation accelerated diffusion rather than thermally-activated conventional aging process. Characterization of dynamic precipitates using techniques such as atom probe tomography (APT), is an important future direction that can be explored. Other areas of future direction in this system are much broader and can be classified into processing, properties and performance areas:

1. Processing: Rare-earths and transition metals have very limited solubility in aluminum. There may be a tendency for other elements to precipitate out during ECAP at room temperature. Hence, another prospect is to explore dynamic precipitation and thermal stability of Nb- and Ta- containing Al-Er-Sc-Zr-Si alloys after SPD.
2. Processing: Additive manufacturing route for Al-Sc alloys to produce near net-shape aerospace components with better distribution of precipitates. The process can be designed such that there is dynamic precipitation during formation of a product. This will be exhaustive study to optimize processing parameters of additive manufacturing such that we can obtain an optimal

combination of strength and ductility of the component both, at room temperature as well as elevated temperature.

3. Properties: Al-Er-Sc-Zr-V-Si alloy have stable nonoperculate which alloy high thermal stability for this alloy. One future direction would be to use this model and merge it with commercial 6000 and 7000 aluminum alloy series to further enhance their high temperature properties. For instance, Al-Si alloy which is also categorized as a high temperature alloy, can be microalloyed with the established composition of Sc, Er, Zr, and V as studied in this dissertation. There is always possibility of some interaction with current phases, but it is likely to give a synergistic effect and enhance the mechanical properties.
4. Performance: Current work showed that there is slight difference between the mechanical properties of V- Nb- and Ta- containing alloys. And a recent study by Dinc et al. (2018) also evaluated similar creep behavior for these three compositions. For design consideration and to establish a selection criterion, high temperature fatigue characterization can also be employed to evaluate a better candidate for industrial applications.

REFERENCES

[1] W. E. Frazier, E. W. Lee, M. E. Donnellan, and J. J. Thompson, “Advanced lightweight alloys for aerospace applications,” *JOM*, vol. 41, no. 5, pp. 22–26, 1989.

[2] G. S. Cole and A. M. Sherman, “Light weight materials for automotive applications,” *Mater. Charact.*, vol. 35, no. 1, pp. 3–9, Jul. 1995.

[3] I. J. Polmear, “Recent Developments in Light Alloys,” *Mater. Trans. JIM*, vol. 37, no. 1, pp. 12–31, 1996.

[4] G. E. Dieter and D. Bacon, “Mechanical metallurgy,” *Journal of the Franklin Institute*, vol. 273, no. 4. p. 338, 1962.

[5] G. E. Totten and D. S. MacKenzie, *Handbook of Aluminum: Vol. 1: Physical Metallurgy and Processes*, vol. 1. CRC Press, 2003.

[6] D. N. Seidman, E. A. Marquis, and D. C. Dunand, “Precipitation strengthening at ambient and elevated temperatures of heat-treatable Al(Sc) alloys,” *Acta Mater.*, vol. 50, no. 16, pp. 4021–4035, 2002.

[7] L. S. Toropova, D. G. Eskinm, M. L. Kharakterovam, and T. V. Dobatkina, *Advanced Aluminum Alloys Containing Scandium: Structure and Properties*. Gordon and Breach Science Publishers, 1998.

[8] C. B. Fuller, D. N. Seidman, and D. C. Dunand, “Creep properties of coarse-grained Al(Sc) alloys at 300 °C,” *Scr. Mater.*, vol. 40, no. 6, pp. 691–696, 1999.

[9] C. B. Fuller, D. N. Seidman, and D. C. Dunand, “Mechanical properties of

Al(Sc,Zr) alloys at ambient and elevated temperatures," *Acta Mater.*, vol. 51, no. 16, pp. 4803–4814, 2003.

[10] R. A. Karnesky, M. E. van Dalen, D. C. Dunand, and D. N. Seidman, "Effects of substituting rare-earth elements for scandium in a precipitation-strengthened Al–0.08at. %Sc alloy," *Scr. Mater.*, vol. 55, no. 5, pp. 437–440, Sep. 2006.

[11] R. a. Karnesky, D. N. Seidman, and D. C. Dunand, "Creep of Al-Sc Microalloys with Rare-Earth Element Additions," *Mater. Sci. Forum*, vol. 519–521, pp. 1035–1040, 2006.

[12] R. A. Karnesky, M. E. van Dalen, D. C. Dunand, and D. N. Seidman, "Effects of substituting rare-earth elements for scandium in a precipitation-strengthened Al-0.08 at. %Sc alloy," *Scr. Mater.*, vol. 55, no. 5, pp. 437–440, 2006.

[13] M. E. Van Dalen, T. Gyger, D. C. Dunand, and D. N. Seidman, "Effects of Yb and Zr microalloying additions on the microstructure and mechanical properties of dilute Al-Sc alloys," *Acta Mater.*, vol. 59, no. 20, pp. 7615–7626, 2011.

[14] C. Booth-Morrison, D. N. Seidman, and D. C. Dunand, "Effect of Er additions on ambient and high-temperature strength of precipitation-strengthened Al-Zr-Sc-Si alloys," *Acta Mater.*, vol. 60, no. 8, pp. 3643–3654, 2012.

[15] A. De Luca, D. C. Dunand, and D. N. Seidman, "Mechanical properties and optimization of the aging of a dilute Al-Sc-Er-Zr-Si alloy with a high Zr/Sc ratio," *Acta Mater.*, vol. 119, pp. 35–42, 2016.

[16] D. Erdeniz *et al.*, "Effect of vanadium micro-alloying on the microstructural evolution and creep behavior of Al-Er-Sc-Zr-Si alloys," *Acta Mater.*, vol. 124, pp.

501–512, 2017.

[17] K. Venkateswarlu, V. Rajinikanth, A. K. Ray, C. Xu, and T. G. Langdon, “The characteristics of aluminum–scandium alloys processed by ECAP,” *Mater. Sci. Eng. A*, vol. 527, no. 6, pp. 1448–1452, 2010.

[18] A. K. Lohar, B. Mondal, D. Rafaja, V. Klemm, and S. C. Panigrahi, “Microstructural investigations on as-cast and annealed Al-Sc and Al-Sc-Zr alloys,” *Mater. Charact.*, vol. 60, no. 11, pp. 1387–1394, 2009.

[19] Y. V. G Davydov and A. N. Fokanov, “Alloying Aluminum alloys with Scandium and Zirconium additives,” *Met. Sci. Heat Treat.*, vol. 38, pp. 390–394, 1996.

[20] K. E. Knipling, R. A. Karnesky, C. P. Lee, D. C. Dunand, and D. N. Seidman, “Precipitation evolution in Al-0.1Sc, Al-0.1Zr and Al-0.1Sc-0.1Zr (at.%) alloys during isochronal aging,” *Acta Mater.*, vol. 58, no. 15, pp. 5184–5195, 2010.

[21] K. E. Knipling, D. N. Seidman, and D. C. Dunand, “Ambient- and high-temperature mechanical properties of isochronally aged Al-0.06Sc, Al-0.06Zr and Al-0.06Sc-0.06Zr (at.%) alloys,” *Acta Mater.*, vol. 59, no. 3, pp. 943–954, 2011.

[22] N. Q. Vo, C. H. Liebscher, M. J. S. Rawlings, M. Asta, and D. C. Dunand, “Creep properties and microstructure of a precipitation-strengthened ferritic Fe-Al-Ni-Cr alloy,” *Acta Mater.*, vol. 71, pp. 89–99, 2014.

[23] S. P. Wen, K. Y. Gao, Y. Li, H. Huang, and Z. R. Nie, “Synergetic effect of Er and Zr on the precipitation hardening of Al-Er-Zr alloy,” *Scr. Mater.*, vol. 65, no. 7, pp. 592–595, 2011.

[24] C. Booth-Morrison, D. C. Dunand, and D. N. Seidman, “Coarsening resistance at

400°C of precipitation-strengthened Al–Zr–Sc–Er alloys," *Acta Mater.*, vol. 59, no. 18, pp. 7029–7042, Oct. 2011.

[25] E. O. Hall, "The Deformation and Ageing of Mild Steel: III Discussion of Results," *Proc. Phys. Soc. Sect. B*, vol. 64, no. 9, p. 747, 1951.

[26] N. J. Petch, "The cleavage strength of polycrystals," *J. Iron Steel Inst. Lond.*, vol. 174, pp. 25–31, 1953.

[27] A. Dubyna, A. Mogucheva, and R. Kaibyshev, "Hall-Petch Relationship in an Al-Mg-Sc Alloy Subjected to ECAP," *Adv. Mater. Res.*, vol. 922, no. May, pp. 120–125, 2014.

[28] M. Furukawa, Z. Horita, M. Nemoto, R. Z. Z. Valiev, and T. G. G. Langdon, "Microhardness measurements and the hall-petch relationship in an Al-Mg alloy with submicrometer grain size," *Acta Mater.*, vol. 44, no. 11, pp. 4619–4629, 1996.

[29] Y. Iwahashi, M. Furukawa, Z. Horita, M. Nemoto, and T. G. Langdon, "Microstructural characteristics of ultrafine-grained aluminum produced using equal-channel angular pressing," *Metall. Mater. Trans. A*, vol. 29, no. 9, pp. 2245–2252, 1998.

[30] V. M. M. Segal, "Materials processing by simple shear," *Mater. Sci. Eng. A*, vol. 197, no. 2, pp. 157–164, Jul. 1995.

[31] V. M. Segal, K. T. Hartwig, and R. E. Goforth, "In situ composites processed by simple shear," *Mater. Sci. Eng. A*, vol. 224, no. 1–2, pp. 107–115, 1997.

[32] G. M. Stoica and P. K. Liaw, "Progress in equal-channel angular processing," *Jom-Journal Miner. Met. Mater. Soc.*, vol. 53, no. 3, pp. 36–40, 2001.

[33] W. J. Kim, S. I. Hong, Y. S. Kim, S. H. Min, H. T. Jeong, and J. D. Lee, “Texture development and its effect on mechanical properties of an AZ61 Mg alloy fabricated by equal channel angular pressing,” *Acta Mater.*, vol. 51, no. 11, pp. 3293–3307, 2003.

[34] A. P. Zhilyaev, K. Oh-ishi, G. I. Raab, and T. R. McNelley, “Influence of ECAP processing parameters on texture and microstructure of commercially pure aluminum,” *Mater. Sci. Eng. A*, vol. 441, no. 1–2, pp. 245–252, 2006.

[35] V. V. Stolyarov, Y. Theodore Zhu, I. V. Alexandrov, T. C. Lowe, and R. Z. Valiev, “Influence of ECAP routes on the microstructure and properties of pure Ti,” *Mater. Sci. Eng. A*, vol. 299, no. 1–2, pp. 59–67, 2001.

[36] V. M. Segal, V. I. Reznikov, A. E. Dobryshevshiy, and V. I. Kopylov, “Plastic working of metals by simple shear,” *Russ. Metall.*, no. 1, pp. 99–105, 1981.

[37] Z. Horita, T. Fujinami, M. Nemoto, and T. G. G. Langdon, “Improvement of mechanical properties for Al alloys using equal-channel angular pressing,” *J. Mater. Process. Technol.*, vol. 117, no. 3, pp. 288–292, 2001.

[38] M. Furukawa, Y. Iwahashi, Z. Horita, M. Nemoto, and T. G. Langdon, “The shearing characteristics associated with equal-channel angular pressing,” *Mater. Sci. Eng. A*, vol. 257, no. 2, pp. 328–332, 1998.

[39] S. Ota, H. Akamatsu, K. Neishi, M. Furukawa, Z. Horita, and T. G. Langdon, “Low-temperature superplasticity in aluminum alloys processed by equal-channel angular pressing,” *Mater. Trans.*, vol. 43, no. 10, pp. 2364–2369, 2002.

[40] I. Sabirov, M. Y. Y. Murashkin, and R. Z. Z. Valiev, “Nanostructured aluminium

alloys produced by severe plastic deformation: New horizons in development," *Mater. Sci. Eng. A*, vol. 560, no. 14, pp. 1–24, 2013.

[41] I. Sabirov, Y. Estrin, M. R. Barnett, I. Timokhina, and P. D. Hodgson, "Enhanced tensile ductility of an ultra-fine-grained aluminum alloy," *Scr. Mater.*, vol. 58, no. 3, pp. 163–166, 2008.

[42] M. Fujda, M. Matvija, T. Kvačkaj, O. Milkovič, P. Zubko, and K. Nagyová, "Structure and properties of AlMgSi alloys after ECAP and post-ECAP ageing," *Mater. Tehnol.*, vol. 46, no. 5, pp. 465–469, 2012.

[43] W. J. Kim and J. Y. Wang, "Microstructure of the post-ECAP aging processed 6061 Al alloys," *Mater. Sci. Eng. A*, vol. 464, no. 1–2, pp. 23–27, 2007.

[44] S. Farè, N. Lecis, and M. Vedani, "Aging Behaviour of Al-Mg-Si Alloys Subjected to Severe Plastic Deformation by ECAP and Cold Asymmetric Rolling," *J. Metall.*, vol. 2011, pp. 1–8, 2011.

[45] C. Xu, M. Furukawa, Z. Horita, and T. G. Langdon, "Influence of ECAP on precipitate distributions in a spray-cast aluminum alloy," *Acta Mater.*, vol. 53, no. 3, pp. 749–758, 2005.

[46] V. L. Sordi, C. A. Feliciano, and M. Ferrante, "The influence of deformation by equal-channel angular pressing on the ageing response and precipitate fracturing: case of the Al–Ag alloy," *J. Mater. Sci.*, vol. 50, no. 1, pp. 138–143, 2015.

[47] J. Gubicza, I. Schiller, N. Q. Chinh, J. Illy, Z. Horita, and T. G. Langdon, "The effect of severe plastic deformation on precipitation in supersaturated Al-Zn-Mg alloys," *Mater. Sci. Eng. A*, vol. 460–461, pp. 77–85, 2007.

[48] M. Murayama, Z. Horita, and K. Hono, “Microstructure of two-phase Al-1.7 at% Cu alloy deformed by equal-channel angular pressing,” *Acta Mater.*, vol. 49, no. 1, pp. 21–29, 2001.

[49] J. K. Kim, H. G. Jeong, S. I. Hong, Y. S. Kim, and W. J. Kim, “Effect of aging treatment on heavily deformed microstructure of a 6061 aluminum alloy after equal channel angular pressing,” *Scr. Mater.*, vol. 45, no. 8, pp. 901–907, 2001.

[50] J. R. Davis, J. R. D. & Associates, and A. S. M. I. H. Committee, *Aluminum and Aluminum Alloys*. ASM International, 1993.

[51] S. Park, Y. Sato, and H. Kokawa, “Microstructural evolution and its effect on Hall-Petch relationship in friction stir welding of thixomolded Mg alloy AZ91D,” *J. Mater. Sci.*, vol. 38, no. 21, pp. 4379–4383, 2003.

[52] Y. Iwahashi, Z. Horita, M. Nemoto, and T. G. Langdon, “EQUAL-CHANNEL ANGULAR PRESSING,” vol. 46, no. 9, 1998.

[53] R. Z. Valiev and T. G. Langdon, “Principles of equal-channel angular pressing as a processing tool for grain refinement,” *Prog. Mater. Sci.*, vol. 51, no. 7, pp. 881–981, Sep. 2006.

[54] Y. Estrin, M. Murashkin, and R. Valiev, “Ultrafine grained aluminium alloys: processes, structural features and properties,” *Fundam. Alum. Metall. Prod. Process. Appl. Woodhead Publ. Limited, Cambridge*, pp. 468–503, 2010.

[55] M. Saravanan, R. M. Pillai, B. C. Pai, M. Brahmakumar, and K. R. Ravi, “Equal channel angular pressing of pure aluminium - An analysis,” *Bull. Mater. Sci.*, vol. 29, no. 7, pp. 679–684, 2006.

[56] Y. Iwahashi, Z. Horita, M. Nemoto, and T. G. Langdon, “An investigation of microstructural evolution during equal-channel angular pressing,” *Acta Mater.*, vol. 45, no. 11, pp. 4733–4741, 1997.

[57] T. G. Langdon, “Twenty-five years of ultrafine-grained materials: Achieving exceptional properties through grain refinement,” *Acta Mater.*, vol. 61, no. 19, pp. 7035–7059, 2013.

[58] W. Q. Cao, A. Godfrey, and Q. Liu, “EBSP investigation of microstructure and texture evolution during equal channel angular pressing of aluminium,” *Mater. Sci. Eng. A*, vol. 361, no. 1–2, pp. 9–14, 2003.

[59] T. G. Langdon, “The principles of grain refinement in equal-channel angular pressing,” *Mater. Sci. Eng. A*, vol. 462, no. 1, pp. 3–11, 2007.

[60] R. E. Barber, T. Dudo, P. B. Yasskin, and K. T. Hartwig, “Product yield for ECAE processing,” *Scr. Mater.*, vol. 51, no. 5, pp. 373–377, 2004.

[61] V. S. Zolotorevsky, N. A. Belov, and M. V Glazoff, *Casting aluminum alloys*, vol. 12. Elsevier Amsterdam, 2007.

[62] A. Association, *Aluminum: properties and physical metallurgy*. ASM International, 1984.

[63] K. E. Knipling, D. C. Dunand, and D. N. Seidman, “Criteria for developing castable, creep-resistant aluminum-based alloys – A review,” *Zeitschrift für Met.*, vol. 97, no. 3, pp. 246–265, Mar. 2006.

[64] Y. M. Wang and E. Ma, “Strain hardening, strain rate sensitivity, and ductility of nanostructured metals,” *Mater. Sci. Eng. A*, vol. 375–377, no. 1–2 SPEC. ISS., pp.

46–52, 2004.

[65] C. Xu and T. G. Langdon, “The development of hardness homogeneity in aluminum and an aluminum alloy processed by ECAP,” *J. Mater. Sci.*, vol. 42, no. 5, pp. 1542–1550, 2007.

[66] E. A. Marquis and D. N. Seidman, “Nanoscale structural evolution of Al 3 Sc precipitates in Al(Sc) alloys,” *Acta Mater.*, vol. 49, no. 11, pp. 1909–1919, 2001.

[67] F. C. Campbell, *Lightweight materials: understanding the basics*. ASM International, 2012.

[68] Y. T. Zhu, T. C. Lowe, and T. G. Langdon, “Performance and applications of nanostructured materials produced by severe plastic deformation,” *Scr. Mater.*, vol. 51, no. 8 SPEC. ISS., pp. 825–830, 2004.

[69] C. Xu, M. Furukawa, Z. Horita, and T. G. Langdon, “Using ECAP to achieve grain refinement, precipitate fragmentation and high strain rate superplasticity in a spray-cast aluminum alloy,” *Acta Mater.*, vol. 51, no. 20, pp. 6139–6149, 2003.

[70] E. Cerri and P. Leo, “Influence of severe plastic deformation on aging of Al-Mg-Si alloys,” *Mater. Sci. Eng. A*, vol. 410–411, no. April, pp. 226–229, 2005.

[71] S. Dadbakhsh, A. Karimi Taheri, and C. W. Smith, “Strengthening study on 6082 Al alloy after combination of aging treatment and ECAP process,” *Mater. Sci. Eng. A*, vol. 527, no. 18–19, pp. 4758–4766, 2010.

[72] T. Radetić, M. Popović, E. Romhanji, and B. Verlinden, “The effect of ECAP and Cu addition on the aging response and grain substructure evolution in an Al-4.4 wt.% Mg alloy,” *Mater. Sci. Eng. A*, vol. 527, no. 3, pp. 634–644, 2010.

[73] J. Mao, S. B. Kang, and J. O. Park, “Grain refinement, thermal stability and tensile properties of 2024 aluminum alloy after equal-channel angular pressing,” *J. Mater. Process. Technol.*, vol. 159, no. 3, pp. 314–320, 2005.

[74] H. J. Roven, M. Liu, and J. C. Werenskiold, “Dynamic precipitation during severe plastic deformation of an Al-Mg-Si aluminium alloy,” *Mater. Sci. Eng. A*, vol. 483–484, no. 1–2 C, pp. 54–58, 2008.

[75] M. Liu *et al.*, “DSC analyses of static and dynamic precipitation of an Al-Mg-Si-Cu aluminum alloy,” *Prog. Nat. Sci. Mater. Int.*, vol. 25, no. 2, pp. 153–158, 2015.

[76] X. Sauvage, M. Y. Murashkin, B. B. Straumal, E. V. Bobruk, and R. Z. Valiev, “Ultrafine Grained Structures Resulting from SPD-Induced Phase Transformation in Al-Zn Alloys,” *Adv. Eng. Mater.*, vol. 17, no. 12, pp. 1821–1827, 2015.

[77] M. J. Starink, “The analysis of Al-based alloys by calorimetry: quantitative analysis of reactions and reaction kinetics,” *Int. Mater. Rev.*, vol. 49, no. 3, pp. 191–226, 2004.

[78] O. Beeri, D. C. Dunand, and D. N. Seidman, “Roles of impurities on precipitation kinetics of dilute Al-Sc alloys,” *Mater. Sci. Eng. A*, vol. 527, no. 15, pp. 3501–3509, 2010.

[79] M. H. Goodarzy, H. Arabi, M. A. Boutorabi, S. H. Seyedein, and S. H. Hasani Najafabadi, “The effects of room temperature ECAP and subsequent aging on mechanical properties of 2024 Al alloy,” *J. Alloys Compd.*, vol. 585, pp. 753–759, 2014.

[80] P. W. J. McKenzie, R. Lapovok, P. Wells, and K. Raviprasad, “Removal of porosity

in cast aluminium alloys by equal channel angular extrusion," in *Materials Science Forum*, 2003, vol. 426, pp. 297–302.

[81] M. Kolar, K. O. Pedersen, S. Gulbrandsen-Dahl, K. Teichmann, and K. Marthinsen, "Effect of Pre-Deformation on Mechanical Response of an Artificially Aged Al-Mg-Si Alloy," *Mater. Trans.*, vol. 52, no. 7, pp. 1356–1362, 2011.

[82] G. W. Smith, "Precipitation kinetics in solutionized aluminum alloy 2124: Determination by scanning and isothermal calorimetry," *Thermochim. Acta*, vol. 317, no. 1, pp. 7–23, 1998.

[83] S. Koch, M. D. Abad, S. Renhart, H. Antrekowitsch, and P. Hosemann, "A high temperature nanoindentation study of Al–Cu wrought alloy," *Mater. Sci. Eng. A*, vol. 644, pp. 218–224, 2015.

[84] N. Q. Vo, D. C. Dunand, and D. N. Seidman, "Improving aging and creep resistance in a dilute Al-Sc alloy by microalloying with Si, Zr and Er," *Acta Mater.*, vol. 63, pp. 73–85, 2014.

[85] L. S. Toporova, D. G. Eskin, M. L. Kharakterova, and T. B. Dobatkina, "Advanced aluminum alloys containing scandium," *Amsterdam: Gordon & Breach*, 1998.

[86] J. Røyset and N. Ryum, "Kinetics and mechanisms of precipitation in an Al-0.2wt.% Sc alloy," *Mater. Sci. Eng. A*, vol. 396, no. 1–2, pp. 409–422, 2005.

[87] R. Z. Valiev, M. Y. Murashkin, E. V Bobruk, and G. I. Raab, "Grain refinement and mechanical behavior of the Al Alloy, subjected to the new SPD technique," *Mater. Trans.*, vol. 50, no. 1, pp. 87–91, 2009.

[88] B. B. Straumal *et al.*, "Formation of nanograined structure and decomposition of

supersaturated solid solution during high pressure torsion of Al-Zn and Al-Mg alloys," *Acta Mater.*, vol. 52, no. 15, pp. 4469–4478, 2004.

[89] T. Sakai, A. Belyakov, R. Kaibyshev, H. Miura, and J. J. Jonas, "Dynamic and post-dynamic recrystallization under hot, cold and severe plastic deformation conditions," *Prog. Mater. Sci.*, vol. 60, no. 1, pp. 130–207, 2014.

[90] E. Ivanov, T. Grigorieva, G. Golubkova, V. Boldyrev, A. B. Fasman, and O. T. Kalinina, "Synthesis of Nickel Alumides by mechanical alloying," *Mater. Lett.*, vol. 7, no. 1, pp. 51–54, 1988.

[91] L. N. Larikov, V. M. Fal'Chenko, V. F. Mazanko, S. M. Gurevich, G. K. Kharchenko, and A. I. Ignatenko, "Anomalous acceleration of diffusion during pulsed loading of metals," *Dokl. Akad. Nauk SSSR*, vol. 221, no. 5, pp. 1073–1075, 1975.

[92] B. B. Khina, I. Solpan, and G. F. Lovshenko, "Modelling accelerated solid-state diffusion under the action of intensive plastic deformation," *J. Mater. Sci.*, vol. 39, no. 16, pp. 5135–5138, 2004.

[93] Y. Huang, J. D. Robson, and P. B. Prangnell, "The formation of nanograin structures and accelerated room-temperature theta precipitation in a severely deformed Al-4 wt.% Cu alloy," *Acta Mater.*, vol. 58, no. 5, pp. 1643–1657, 2010.

[94] Y. Buranova *et al.*, "Al3(Sc,Zr)-based precipitates in Al-Mg alloy: Effect of severe deformation," *Acta Mater.*, vol. 124, pp. 210–224, 2017.

[95] B. B. Straumal, V. Pontikis, A. R. Kilmametov, A. A. Mazilkin, and S. V Dobatkin, "Competition between precipitation and dissolution in Cu-Ag alloys under high

pressure torsion," *Acta Mater.*, vol. 122, pp. 60–71, 2017.

[96] B. B. Straumal *et al.*, "Transformations of Cu(in) supersaturated solid solutions under high-pressure torsion," *Mater. Lett.*, vol. 138, pp. 255–258, 2015.

[97] W. H. Hildebrandt, "Differential Scanning Calorimetry Evaluations of Recrystallization Behaviour in Aluminium Sheet," vol. 10A, pp. 1045–1048, 1979.

[98] H. Hallem, W. J. Rittel, B. Forbord, and K. Marthinsen, "Recrystallisation Resistance of Extruded and Cold Rolled Aluminium Alloys with Additions of Hf, Sc and Zr," *Mater. Sci. Forum*, vol. 519–521, pp. 525–530, 2006.

[99] M. E. van Dalen, R. A. Karnesky, J. R. Cabotaje, D. C. Dunand, and D. N. Seidman, "Erbium and ytterbium solubilities and diffusivities in aluminum as determined by nanoscale characterization of precipitates," *Acta Mater.*, vol. 57, no. 14, pp. 4081–4089, 2009.

[100] F. N. Rhines, K. R. Craig, and R. T. DeHoff, "Mechanism of steady-state grain growth in aluminum," *Metall. Trans.*, vol. 5, no. 2, pp. 413–425, 1974.

[101] Z. Huda, M. Saufi, and R. Shaifulazuar, "Mechanism of grain growth in an aerospace aluminum alloy," *J. Ind. Technol*, vol. 15, pp. 127–136, 2006.

[102] Z. Huda and T. Zaharinie, "Kinetics of grain growth in 2024-T3: An aerospace aluminum alloy," *J. Alloys Compd.*, vol. 478, no. 1–2, pp. 128–132, 2009.

[103] J. E. Burke and D. Turnbull, "Recrystallization and grain growth," *Prog. Met. Phys.*, vol. 3, pp. 220–292, 1952.

[104] H. Hu and B. B. Rath, "On the time exponent in isothermal grain growth," *Metall. Trans.*, vol. 1, no. 11, pp. 3181–3184, 1970.

[105] E. A. Grey and G. T. Higgins, “Solute limited grain boundary migration: A rationalisation of grain growth,” *Acta Metall.*, vol. 21, no. 4, pp. 309–321, 1973.

[106] G. Gottstein and L. S. Shvindlerman, *Grain boundary migration in metals: thermodynamics, kinetics, applications*. CRC press, 2009.

[107] M. Legros, D. S. Gianola, and K. J. Hemker, “In situ TEM observations of fast grain-boundary motion in stressed nanocrystalline aluminum films,” *Acta Mater.*, vol. 56, no. 14, pp. 3380–3393, 2008.

[108] Y. B. Wang, B. Q. Li, M. L. Sui, and S. X. Mao, “Deformation-induced grain rotation and growth in nanocrystalline Ni,” *Appl. Phys. Lett.*, vol. 92, no. 1, pp. 2006–2009, 2008.

[109] F. Mompiou, D. Caillard, and M. Legros, “Grain boundary shear-migration coupling-I. In situ TEM straining experiments in Al polycrystals,” *Acta Mater.*, vol. 57, no. 7, pp. 2198–2209, 2009.

[110] M. Tonks, P. Millett, W. Cai, and D. Wolf, “Analysis of the elastic strain energy driving force for grain boundary migration using phase field simulation,” *Scr. Mater.*, vol. 63, no. 11, pp. 1049–1052, 2010.

[111] F. Mompiou, M. Legros, and D. Caillard, “Direct observation and quantification of grain boundary shear-migration coupling in polycrystalline Al,” *J. Mater. Sci.*, vol. 46, no. 12, pp. 4308–4313, 2011.

[112] D. S. Gianola, S. Van Petegem, M. Legros, S. Brandstetter, H. Van Swygenhoven, and K. J. Hemker, “Stress-assisted discontinuous grain growth and its effect on the deformation behavior of nanocrystalline aluminum thin films,” *Acta Mater.*, vol.

54, no. 8, pp. 2253–2263, 2006.

[113] D. A. Molodov, T. Gorkaya, and G. Gottstein, “Dynamics of grain boundaries under applied mechanical stress,” *J. Mater. Sci.*, vol. 46, no. 12, pp. 4318–4326, 2011.

[114] A. J. Haslam, D. Moldovan, V. Yamakov, D. Wolf, S. R. Phillpot, and H. Gleiter, “Stress-enhanced grain growth in a nanocrystalline material by molecular-dynamics simulation,” *Acta Mater.*, vol. 51, no. 7, pp. 2097–2112, 2003.

[115] P. A. Beck and P. R. Sperry, “Strain induced grain boundary migration in high purity aluminum,” *J. Appl. Phys.*, vol. 21, no. 2, pp. 150–152, 1950.

[116] G. J. Fan, L. F. Fu, H. Choo, P. K. Liaw, and N. D. Browning, “Uniaxial tensile plastic deformation and grain growth of bulk nanocrystalline alloys,” *Acta Mater.*, vol. 54, no. 18, pp. 4781–4792, 2006.

[117] M. A. Clark and T. H. Alden, “Deformation enhanced grain growth in a superplastic Sn-1% Bi alloy,” *Acta Metall.*, vol. 21, no. 9, pp. 1195–1206, 1973.

[118] M. Jin, A. M. Minor, E. A. Stach, and J. W. Morris, “Direct observation of deformation-induced grain growth during the nanoindentation of ultrafine-grained Al at room temperature,” *Acta Mater.*, vol. 52, no. 18, pp. 5381–5387, 2004.

[119] X. Z. Liao *et al.*, “High-pressure torsion-induced grain growth in electrodeposited nanocrystalline Ni,” *Appl. Phys. Lett.*, vol. 88, no. 2, pp. 1–3, 2006.

[120] Y. B. Wang, J. C. Ho, X. Z. Liao, H. Q. Li, S. P. Ringer, and Y. T. Zhu, “Mechanism of grain growth during severe plastic deformation of a nanocrystalline Ni-Fe alloy,” *Appl. Phys. Lett.*, vol. 94, no. 1, 2009.

[121] Y. Lin, H. Wen, Y. Li, B. Wen, W. Liu, and E. J. Lavernia, “Stress-induced grain growth in an ultra-fine grained Al alloy,” *Metall. Mater. Trans. B Process Metall. Mater. Process. Sci.*, vol. 45, no. 3, pp. 795–810, 2014.

[122] A. K. Mukherjee, “An examination of the constitutive equation for elevated temperature plasticity,” *Mater. Sci. Eng. A*, vol. 322, no. 1–2, pp. 1–22, 2002.

[123] Y. Lin, B. Xu, Y. Feng, and E. J. Lavernia, “Stress-induced grain growth during high-temperature deformation of nanostructured Al containing nanoscale oxide particles,” *J. Alloys Compd.*, vol. 596, pp. 79–85, 2014.

[124] N. E. Hamilton and M. Ferry, “Grain growth in a nanocrystalline Al-Sc alloy,” *Mater. Trans.*, vol. 45, no. 7, pp. 2264–2271, 2004.

[125] V. Jindal, P. K. De, and K. Venkateswarlu, “Effect of Al3Sc precipitates on the work hardening behavior of aluminum-scandium alloys,” *Mater. Lett.*, vol. 60, pp. 3373–3375, 2006.

[126] J. Hedworth and M. J. Stowell, “The measurement of strain-rate sensitivity in superplastic alloys,” *J. Mater. Sci.*, vol. 6, no. 8, pp. 1061–1069, 1971.

[127] D. H. Bae and a K. Ghosh, “Grain size and temperature dependence of superplastic deformation in an Al-Mg alloy under isostructural condition,” *Acta Mater.*, vol. 48, no. 6, pp. 1207–1224, 2000.

[128] J. Malik *et al.*, “Equal Channel Angular Pressing of a Newly Developed Precipitation Hardenable Scandium Containing Aluminum Alloy,” *TMS Annu. Meet. Exhib.*, pp. 423–429, 2018.

[129] Z. Horita, T. Fujinami, M. Nemoto, and T. G. Langdon, “Equal-channel angular

pressing of commercial aluminum alloys: Grain refinement, thermal stability and tensile properties," *Metall. Mater. Trans. A Phys. Metall. Mater. Sci.*, vol. 31A, no. 3, pp. 691–701, 2000.

[130] A. Bommareddy, M. Z. Quadir, and M. Ferry, "Time and temperature regime of continuous grain coarsening in an ECAP-processed Al(0.1 wt.% Sc) alloy," *J. Alloys Compd.*, vol. 527, pp. 145–151, 2012.

[131] C. M. Cepeda-Jiménez, M. Castillo-Rodríguez, J. M. Molina-Aldareguia, Y. Huang, T. G. Langdon, and M. T. Pérez-Prado, "Controlling the high temperature mechanical behavior of Al alloys by precipitation and severe straining," *Mater. Sci. Eng. A*, vol. 679, pp. 36–47, 2017.

[132] R. C. Picu, G. Vincze, F. Ozturk, J. J. Gracio, F. Barlat, and A. M. Maniatty, "Strain rate sensitivity of the commercial aluminum alloy AA5182-O," *Mater. Sci. Eng. A*, vol. 390, no. 1–2, pp. 334–343, 2005.

[133] J. Xu, J. Li, L. Shi, D. Shan, and B. Guo, "Effects of temperature, strain rate and specimen size on the deformation behaviors at micro/meso-scale in ultrafine-grained pure Al," *Mater. Charact.*, vol. 109, pp. 181–188, 2015.

[134] D. Erdeniz, A. De Luca, D. N. Seidman, and D. C. Dunand, "Effects of Nb and Ta additions on the strength and coarsening resistance of precipitation-strengthened Al-Zr-Sc-Er-Si alloys," *Mater. Charact.*, vol. 141, no. April, pp. 260–266, 2018.

[135] W. Nasim *et al.*, "Structure and growth of core–shell nanoprecipitates in Al–Er–Sc–Zr–V–Si high-temperature alloys," *J. Mater. Sci.*, vol. 54, no. 2, pp. 1857–1871, 2019.

[136] C. Booth-Morrison, D. N. Seidman, and D. C. Dunand, “Effect of Er additions on ambient and high-temperature strength of precipitation-strengthened Al–Zr–Sc–Si alloys,” *Acta Mater.*, vol. 60, no. 8, pp. 3643–3654, 2012.

[137] M. Liu *et al.*, “Aging behavior and mechanical properties of 6013 aluminum alloy processed by severe plastic deformation,” *Trans. Nonferrous Met. Soc. China*, vol. 24, no. 12, pp. 3858–3865, 2014.

[138] A. Deschamps, F. De Geuser, Z. Horita, S. Lee, and G. Renou, “Precipitation kinetics in a severely plastically deformed 7075 aluminium alloy,” *Acta Mater.*, vol. 66, pp. 105–117, 2014.

[139] J. G. Morris, “Dynamic strain aging in aluminum alloys,” *Mater. Sci. Eng.*, vol. 13, no. 2, pp. 101–108, 1974.

[140] C. B. Fuller, A. R. Krause, D. C. Dunand, and D. N. Seidman, “Microstructure and mechanical properties of a 5754 aluminum alloy modified by Sc and Zr additions,” *Mater. Sci. Eng. A*, vol. 338, no. 1–2, pp. 8–16, 2002.

[141] W. J. Kim, C. S. Chung, D. S. Ma, S. I. Hong, and H. K. Kim, “Optimization of strength and ductility of 2024 Al by equal channel angular pressing (ECAP) and post-ECAP aging,” *Scr. Mater.*, vol. 49, no. 4, pp. 333–338, 2003.

[142] L. Jiang *et al.*, “Microalloying ultrafine grained al alloys with enhanced ductility,” *Sci. Rep.*, vol. 4, pp. 1–6, 2014.

[143] C. Y. Yu, P. L. Sun, P. W. Kao, and C. P. Chang, “Evolution of microstructure during annealing of a severely deformed aluminum,” *Mater. Sci. Eng. A*, vol. 366, no. 2, pp. 310–317, 2004.

[144] J. Røyset and N. Ryum, “Scandium in aluminium alloys,” *Int. Mater. Rev.*, vol. 50, no. 1, pp. 19–44, 2005.

[145] G. J. Fan *et al.*, “Deformation behavior of an ultrafine-grained Al-Mg alloy at different strain rates,” *Scr. Mater.*, vol. 52, no. 9, pp. 929–933, 2005.

[146] Y. Wang, M. Chen, F. Zhou, and E. Ma, “High tensile ductility in a nanostructured metal,” *Nature*, vol. 419, no. 6910, pp. 912–915, 2002.

[147] B. Q. Han, F. A. Mohamed, and E. J. Lavernia, “Deformation mechanisms and ductility of nanostructured Al alloys,” vol. 821, no. May, pp. 263–268, 2004.

[148] M. Ferry, N. E. Hamilton, and F. J. Humphreys, “Continuous and discontinuous grain coarsening in a fine-grained particle-containing Al-Sc alloy,” *Acta Mater.*, vol. 53, no. 4, pp. 1097–1109, 2005.

[149] Z. R. Nie *et al.*, “Research on Rare Earth in Aluminum,” *Mater. Sci. Forum*, vol. 396–402, pp. 1730–1731, 2002.

[150] J. Malik *et al.*, “Equal Channel Angular Pressing of a Newly Developed Precipitation Hardenable Scandium Containing Aluminum Alloy,” *TMS Annu. Meet. Exhib.*, pp. 423–429, 2018.

[151] Y. Deng, Z. Yin, K. Zhao, J. Duan, J. Hu, and Z. He, “Effects of Sc and Zr microalloying additions and aging time at 120°C on the corrosion behaviour of an Al–Zn–Mg alloy,” *Corros. Sci.*, vol. 65, pp. 288–298, 2012.

[152] A. De Luca, D. C. Dunand, D. N. Seidman, and O. Martin, “Scandium-Enriched Nanoprecipitates in Aluminum Providing Enhanced Coarsening and Creep Resistance,” 2018, pp. 1589–1594.

[153] J. Esquivel, H. A. Murdoch, K. A. Darling, and R. K. Gupta, “Excellent corrosion resistance and hardness in Al alloys by extended solid solubility and nanocrystalline structure,” *Mater. Res. Lett.*, vol. 6, no. 1, pp. 79–83, 2018.

[154] M. E. M. EL-Bedawy, “Effect of aging on the corrosion of aluminum alloy 6061,” 2010.

[155] V. Neubert, B. Smola, I. Stulíková, A. Bakkar, and J. Reuter, “Microstructure, mechanical properties and corrosion behaviour of dilute Al–Sc–Zr alloy prepared by powder metallurgy,” *Mater. Sci. Eng. A*, vol. 464, no. 1, pp. 358–364, 2007.

[156] H. Yoshioka, H. Habazaki, A. Kawashima, K. Asami, and K. Hashimoto, “The corrosion behavior of sputter-deposited Al.Zr alloys in 1 M HCl solution,” *Corros. Sci.*, vol. 33, no. 3, pp. 425–436, 1992.

[157] R. C. Bhardwaj, A. Gonzalezmartin, and J. O. Bockris, “Insitu corrosion studies of aluminum and aluminum tantalum alloy in 0.01M NaCl using STM,” *J. Electrochem. Soc.*, vol. 139, no. 4, pp. 1050–1058, 1992.

[158] M. Metikoš-Huković, A. Kwokal, and J. Piljac, “The influence of niobium and vanadium on passivity of titanium-based implants in physiological solution,” *Biomaterials*, vol. 24, no. 21, pp. 3765–3775, 2003.

[159] A. K. Shukla, R. Balasubramaniam, and S. Bhargava, “Properties of passive film formed on CP titanium, Ti–6Al–4V and Ti–13.4Al–29Nb alloys in simulated human body conditions,” *Intermetallics*, vol. 13, no. 6, pp. 631–637, 2005.

[160] F. Rosalbino, E. Angelini, S. De Negri, A. Saccone, and S. Delfino, “Influence of the rare earth content on the electrochemical behaviour of Al–Mg–Er alloys,”

Intermetallics, vol. 11, no. 5, pp. 435–441, 2003.

[161] W. Nasim *et al.*, "Structure and growth of core–shell nanoprecipitates in Al–Er–Sc–Zr–V–Si high-temperature alloys," *J. Mater. Sci.*, 2018.

[162] N. Q. Vo, D. C. Dunand, and D. N. Seidman, "Improving aging and creep resistance in a dilute Al–Sc alloy by microalloying with Si, Zr and Er," *Acta Mater.*, vol. 63, pp. 73–85, 2014.

[163] A. U. Chaudhry, B. Mansoor, T. Mungole, G. Ayoub, and D. P. Field, "Corrosion mechanism in PVD deposited nano-scale titanium nitride thin film with intercalated titanium for protecting the surface of silicon," *Electrochim. Acta*, vol. 264, pp. 69–82, 2018.

[164] A. De Luca, D. C. Dunand, and D. N. Seidman, "Microstructure and mechanical properties of a precipitation- strengthened Al-Zr-Sc-Er-Si alloy with a very small Sc content," *Acta Mater.*, vol. 144, pp. 80–91, 2018.

[165] Y. W. Keuong, J. H. Nordlien, S. Ono, and K. Nisancioglu, "Electrochemical Activation of Aluminum by Trace Element Lead," *J. Electrochem. Soc.*, vol. 150, no. 11, pp. B547–B551, 2003.

[166] H. Habazaki, K. Shimizu, P. Skeldon, G. E. Thompson, G. C. Wood, and X. Zhou, "Effects of Alloying Elements in Anodizing of Aluminium," *Trans. IMF*, vol. 75, no. 1, pp. 18–23, 1997.

[167] S. Zečević, L. Gajić, A. R. Despić, and D. M. Drazić, "Effect of pulsating current on anode polarisation in an aluminium anode battery with a neutral aqueous electrolyte," *Electrochim. Acta*, vol. 26, no. 11, pp. 1625–1631, 1981.

[168] A. R. Despić, D. M. Dražić, M. M. Purenović, and N. Ciković, “Electrochemical properties of aluminium alloys containing indium, gallium and thallium,” *J. Appl. Electrochem.*, vol. 6, no. 6, pp. 527–542, 1976.

[169] R. H. Burns, F. S. Shuker, and P. E. Manning, “Industrial Applications of Corrosion-Resistant Tantalum, Niobium, and Their Alloys,” in *Refractory Metals and Their Industrial Applications*, ASTM International, 1984.

[170] A. Afseth, J. H. Nordlien, G. M. Scamans, and K. Nisancioglu, “Effect of heat treatment on electrochemical behaviour of aluminium alloy AA3005,” *Corros. Sci.*, vol. 44, no. 1, pp. 145–162, 2002.

[171] A. A., B. M., B. F. J., O. R., and M. M., “Using EIS to study the electrochemical response of alloy AA5083 in solutions of NaCl,” *Mater. Corros.*, vol. 52, no. 3, pp. 185–192, 2001.

[172] M. C. Quevedo, G. Galicia, R. Mayen-Mondragon, and J. G. Llongueras, “Role of turbulent flow seawater in the corrosion enhancement of an Al–Zn–Mg alloy: an electrochemical impedance spectroscopy (EIS) analysis of oxygen reduction reaction (ORR),” *J. Mater. Res. Technol.*, vol. 7, no. 2, pp. 149–157, 2018.

[173] F. Mansfeld, “Analysis and interpretation of EIS data for metals and alloys,” *Tech. Rep. 26*, 1993.

[174] J. B. Bessone, D. R. Salinas, C. E. Mayer, M. Ebert, and W. J. Lorenz, “An EIS study of aluminium barrier-type oxide films formed in different media,” *Electrochim. Acta*, vol. 37, no. 12, pp. 2283–2290, 1992.

[175] J. M. A. El Kader and A. M. S. El Din, “Film Thickening on Nickel in Aqueous

Solution in Relation to Anion Type and Concentration," *Br. Corros. J.*, vol. 14, no. 1, pp. 40–45, 1979.

[176] P. M. Natishan and W. E. O'Grady, "Chloride Ion Interactions with Oxide-Covered Aluminum Leading to Pitting Corrosion: A Review," *J. Electrochem. Soc.*, vol. 161, no. 9, pp. C421–C432, 2014.

[177] G. S. Frankel, "Pitting Corrosion of Metals: A Review of the Critical Factors," *J. Electrochem. Soc.*, vol. 145, no. 6, pp. 2186–2198, 1998.

[178] J. Kruger, "Passivity of metals – a materials science perspective," *Int. Mater. Rev.*, vol. 33, no. 1, pp. 113–130, 1988.

[179] E. Sato, M. Sato, and I. Uchiyama, "Pitting Corrosion of Aluminum in Sodium Chloride Solution and Analyses of Surface Films," 防食技術, vol. 24, no. 5, pp. 223–229, 1975.

[180] C. Escrivà-Cerdán, E. Blasco-Tamarit, D. M. García-García, J. García-Antón, and A. Guenbour, "Passivation behaviour of Alloy 31 (UNS N08031) in polluted phosphoric acid at different temperatures," *Corros. Sci.*, vol. 56, pp. 114–122, 2012.

[181] D. S. Keir, M. J. Pryor, and P. R. Sperry, "The Influence of Ternary Alloying Additions on the Galvanic Behavior of Aluminum-Tin Alloys," *J. Electrochem. Soc.*, vol. 116, no. 3, pp. 319–322, 1969.

[182] D. S. Keir, M. J. Pryor, and P. R. Sperry, "Galvanic Corrosion Characteristics of Aluminum Alloyed with Group IV Metals," *J. Electrochem. Soc.*, vol. 114, no. 8, pp. 777–782, 1967.

[183] Z. Ahmad, A. Ul-Hamid, and A.-A. B.J, "The corrosion behavior of scandium

alloyed Al 5052 in neutral sodium chloride solution," *Corros. Sci.*, vol. 43, no. 7, pp. 1227–1243, 2001.

[184] H. C. Laura P, McCabe, Gordon A. Sargebt, "Effect of microstructure on the erosion of steels by solid particles," *Wear*, vol. 105, pp. 257–277, 1985.